The Impact of Irradiation Particle Type and Energy on Radiation-induced Trap Properties in CCDs

Thesis submitted for the degree of

Doctor of Philosophy

at The Open University

by

Anton Lindley-DeCaire

Centre for Electronic Imaging

School of Physical Science

Faculty of Science Technology Engineering and Mathematics

The Open University

September 2020

Abstract

This thesis describes a study on the impact of irradiation particle type and particle energy on silicon-based detectors. Radiation damage is a major limiting factor to achieving high-accuracy scientific observations in space and can reduce a mission's operational lifetime. Highly energetic particles can penetrate through satellites, reflect off the mirrors in the focal plane (e.g., Chandra) or interact with the body of the satellite to produce secondary particles that are energetic enough to fluoresce or damage the devices. The energetic particle can displace a silicon atom from its regular lattice position and the resulting vacancy (the lattice position absent of a silicon atom) can migrate through the device until it finds an energetically stable pairing. This degrades the performance of the detector and therefore quality of the science delivered. There is currently no ideal solution to fully mitigate radiation damage, instead any remaining damage must be corrected post-irradiation. This correction requires a complete understanding of the damage mechanisms and a real time measurement of the damage sites in the imaging area.

Upcoming missions such as Euclid require a high level of post-imaging corrections to meet the ambitious scientific goals and will be utilising the "trap pumping" technique in-orbit to perform live characterisations on the active defects. The trap pumping technique is used extensively in this study to identify radiation induced defects in the silicon lattice by characterising defects introduced by energetic interactions at various energies and doses, including irradiation by protons, photons, neutrons and electrons. Different particle types and energies can cause ionisation damage, single atom displacement damage or clusters of atomic displacements.

In this study several new and important results have been identified relating to n-channel defects. These defects are specific to particle type and energy. In particular the presence of a "fast tail" of emission time constants of the divacancy are found for proton and neutron irradiations and absent in gamma irradiations. Furthermore, a spread of emission times is found for all particle irradiations which indicates traps may occupy a distribution of energies/cross sections around an energy level rather

than a single fixed emission time constant for each trap species. This work also shows that potential pockets can be falsely identified as traps through the trap pumping technique when insufficient datapoints are used. These results improve our fundamental understanding of trap dynamics in n-channel silicon and can help shape the strategy for damage mitigation and testing strategy for trap pumping in CCD based satellite missions.

Declaration

I hereby declare that no part of this thesis has been previously submitted to this or any other university as part of the requirement for a higher degree. The work described herein was conducted solely by the undersigned except for those colleagues and other workers acknowledged in the text.

Dedication

This thesis is dedicated to my parents and to Sarah.

Acknowledgements

The work of this thesis could not have been completed without the help and support of many people. I would particularly like to thank my supervisory team David Hall, Nathan Bush and Ben Dryer for all their encouragement and assistance throughout the PhD.

Thank you to all the staff at the CEI including Konstantin Stefanov, Andrew Holland, Matthew Soman, Jesper Skottfelt, Chiaki Crews, Oliver Hetherington, Julian Heymes, Martin Prest, George Randall, Zoe Lee-Payne, Martine Harvey, James Endicott and Steven Parsons.

Thank you to David Burt, Doug Jordan and Mark Robbins from Teledyne-e2v for sharing their technical knowledge and assistance whenever possible.

I would like to thank my PhD colleagues past and present including Matt Lewis, Alice Dunford, James Ivory, Daniel-Dee Lofthouse- Smith, Chris Davis, Thomas Buggey, Harry Fox, Edgar Allenwood, Saad Ahmed and Lawrence Jones and more.

A final thank you to all the friends and family that have been a part of the PhD experience.

List of acronyms

ACE	Advanced Composition Explorer
ACIS	Advanced CCD Imaging Spectrometer
ADU	Analogue to Digital Units
AIMO	Advanced Inverted Mode Operation
AR	Anti-Reflection
ASTM	American Society for Testing and Materials
CCD	Charge Coupled Device
CME	Coronal Mass Ejection
CTE	Charge Transfer Efficiency
CTI	Charge Transfer Inefficiency
DDD	Displacement Damage Dose
DLTS	Deep Level Transient Spectroscopy
DN	Data Numbers
DSNU	Dark Signal Non-Uniformity
ECSS	European Cooperation for Space Standardization
EMCCD	Electron Multiplying Charge Coupled Device
EPER	Extended Pixel Edge Response
EPR	Electron Paramagnetic Resonance
ESA	European Space Agency
ESTEC	European Space Research and Technology Centre
FPR	First Pixel Response
GCR	Galactic Cosmic Rays
HEO	Highly Elliptical Orbit
HST	Hubble Space Telescope
IMO	Inverted Mode Operation
IR	Infrared
JDEM	Joint Dark Energy Mission
JUICE	JUpiter ICy Moons Explorer
LED	Light Emitting Diode
LET	Linear Energy Transfer
LPCVD	Low Pressure Chemical Vapor Deposition
LST	Large Space Telescope
NASA	The National Aeronautics and Space Administration
NIEL	Non-Ionising Energy Loss
NIMO	Non-Inverted Mode Operation
NIR	Near-Infrared
NIST	National Institute of Standards and Technology
NPL	National Physics Laboratory
OAO-2	Orbiting Astronomical Observatory
ONERA	Office National d'Etudes et de Recherches Aerospatiales
PKA	Primary Knock-on Atom
PLATO	PLAnetary Transits and Oscillations of stars
PSI	Paul Scherrer Institut
QE	Quantum Efficiency
RPS	Random Pumping Signal
RTS	Random Telegraph Signal
SAA	South Atlantic Anomaly
SDO	Solar Dynamic Observatory

SMILE	The Solar wind Magnetosphere Ionosphere Link Explorer
SOHO	Solar and Heliospheric Observatory
SPENVIS	SPace ENVironment Information System
SRH	Shockley-Read-Hall
TEC	ThermoElectric Cooler
TID	Total Ionising Dose
TRIM	TRansport of Ions in Matter
UV	Ultra-Violet
VIS	VISible imager

Publications

The results from the thesis are presented in:

Lindley-DeCaire, A., Hall, D., Bush, N., Dryer, B. and Holland, A., 2019, September. The silicon lattice defects in proton and gamma irradiated n-channel CCDs. In *UV/Optical/IR Space Telescopes and Instruments: Innovative Technologies and Concepts IX* (Vol. 11115, p. 111150C). International Society for Optics and Photonics.

Lindley-DeCaire, A, Soman, M., 2019, February. ESA NPI Program: CCD347-20 Gamma Irradiation Characterisation Report (Technical Report).

Further publications are in preparation based on the research in Chapters 5-7.

Contents

Chapter 1: Introduction 1
1.1 Context 1
1.2 Aims and Objectives 3
1.3 Thesis Structure 3
1.4 References 4
Chapter 2: The Charge Coupled Device 6
2.1 The Principals of Operation of a CCD 6
2.1.1 Principal of the pn-Junction 7
2.1.2 Charge Collection 8
2.1.3 Charge Transfer 10
2.1.4 The Output Circuit 11
2.2 Noise Sources 13
2.3 Quantum Efficiency 14
2.4 Dark current 16
2.5 Charge Transfer Efficiency 17
2.6 References 18
Chapter 3: Radiation Damage Effects on CCDs 19
3.1 The Space Radiation Environment 19
3.1.1 Solar Activity 20
3.1.2 Galactic Cosmic Rays 21
3.1.3 Planetary Considerations 23
3.2 Stopping Power 25
3.3 Ionisation Damage 28
3.3.1 Gate Dielectric Damage 28
3.3.2 De-passivation and Surface Traps 29
3.4 Displacement Damage 30
3.4.1 Point Defects 31
3.4.2 Cluster Defects 34
3.4.3 The Operational Impact of Defects on CCDs 35
3.4.4 The NIEL Scaling Hypothesis 39
3.5 Radiation Damage in CCDs in Flight 39
3.5.1 Shielding 41
3.6 Annealing 42

3.7 References 44
Chapter 4: The Trap Pumping Technique 49
4.1 Introduction 49
4.1.1 A History of Pocket Pumping to Trap Pumping 49
4.1.2 The DLTS Technique 55
4.1.3 Euclid VIS Instrument 56
4.1.4 Understanding the Spread in Emission Time Constants 57
4.2 Detailed Theory of Trap Pumping 58
4.3 References 64
Chapter 5: Proton Radiation Damage 67
5.1 Introduction 67
5.1.1 CCD47-20 Devices 69
5.1.2 Irradiation Facility 70
5.2 Trap Pumping Experimental Setup 71
5.2.1 Experimental Method 73
5.2.2 Clocking Sequence 74
5.2.3 Trap Measurements 76
5.2.4 Probing Region 78
5.3 Proton Trap Pumping Results 80
5.3.1 Trap Detection 80
5.3.2 Traps Present From Manufacturing 84
5.3.3 Traps Produced by Proton Irradiations 85
5.3.4 Energy Level 88
5.4 Summary 92
5.5 References 92
Chapter 6: Gamma Radiation Damage 94
6.1 Introduction 94
6.1.1 The CCD347-20 96
6.1.2 Irradiation Facility 96
6.2 Trap Pumping Measurements 98
6.3 Gamma Trap Pumping Results 100
6.3.1 Trap Detection 100
6.3.2 Potential Pockets 102
6.3.3 Irradiated Trap Landscape 106
6.3.4 Energy Levels 108
6.4 Summary 109

6.5 References 110
Chapter 7: Comparison of Multiple Damage Types 112
7.1 Introduction 112
7.2 Proton and Gamma Irradiation Comparison 114
7.2.1 Emission Time Constants 114
7.2.2 Energy Level and Cross Section Measurements First Method 117
7.2.3 Energy Land Cross Section Measurements Second Method 119
7.3 Neutron irradiation comparison 122
7.3.1 Traps produced by neutron irradiations 122
7.3.2 Electron irradiation experimental setup 126
7.3.3 Comparison of the neutron and electron trap landscapes 126
7.3.4 Comparison of neutron and proton irradiations 129
7.3.5 Energy level of the X2 peak 130
7.4 NIEL Scaling Discussion 131
7.5 “RPS Defects” 132
7.6 Summary 137
7.7 References 139
Chapter 8: Conclusions and future work 141

Chapter 1: Introduction

1.1 Context

Charge Coupled Devices (CCDs) are light-sensitive integrated circuits invented in the 1970s (1-3). This semiconductor device has proven highly successful in astronomical observations and revolutionised our understanding of the universe. Since the CCD's initial use in space-based astronomy, manufacturers and scientists have improved the radiation hardness of the CCD by making many advancements the architecture, operating principles and post-imaging damage correction algorithms as the space radiation environment and the damage mechanisms become better understood.

Space-based observatories are still an essential scientific tool for astronomy as the Earth's atmosphere blocks photon wavelength bands to varying degrees including gamma rays, X-rays, ultraviolet light and most of the infrared spectrum. Ground-based telescopes must also correct for distortions in the visible light spectrum which can be distorted by turbulence in the air. However, satellites become exposed to the high energy photons and particles that are otherwise absorbed in the atmosphere. The resulting radiation damage can degrade the performance of the CCD in several ways, one of which is displacement damage, disrupting the uniform silicon crystal lattice and forming unwanted, stable defects with energy levels in the bandgap. A small number of the unwanted defects with energy levels close to the conduction band are capable of trapping and releasing signal charge which degrades the Charge Transfer Efficiency (CTE), a critical metric of observations. Historically, radiation damage has been difficult to fully mitigate in CCDs, with missions such as the Hubble Space Telescope (HST) heating up the detectors to allow radiation-induced defects to change the lattice configuration to another, less impactful defect species. Correction algorithms were developed to rectify radiation damage and software was specially designed to correct the effects of Charge Transfer Inefficiency (CTI), in the case of HST reducing the effects of CTI by 97% (4). Euclid is a European Space Agency (ESA) mission for which its Visible (VIS) instrument will require data correction algorithms to reduce the effects of CTI

by approximately 99% (5,6) by the end of its useful scientific lifetime, requiring significant steps forward for this to be achieved beyond the correction currently possible on HST.

The space radiation environment can be highly variable with a multitude of particle types bombarding the detector at vastly different energies and doses. Many factors affect the dose received by the detector such as the chosen orbit, solar activity and shielding. For example, orbits that pass through the high energy high flux South Atlantic Anomaly (SAA) region require either a significant radiation shield or to turn the device off entirely to preserve the effective lifetime of the devices. Standard solar output increases and decreases on a measured 11 year cycle, with periods of low and high intensity radiation emission, but random highly energetic flares from the surface emit large numbers of damaging particles in a short period of time, rapidly degrading instrument sensors.

The radiation environments around different planets in our solar system are known to have different particle compositions. For example, the radiation belts of Jupiter are dominated by high energy electrons while near-Earth belts are dominated by high energy protons.

Many radiation damage studies involving Electron Paramagnetic Resonance (EPR) (7), infrared (IR) spectroscopy (8), photoconductivity (9) and Deep-Level Transient Spectroscopy (DLTS) (10) techniques have looked into the trap properties of silicon-based devices following irradiations to better understand the effect of different particle interactions with silicon for different particle types and energies. For ten years, a powerful measurement technique known as "trap pumping" has been used for the study of defects in CCDs by locating and characterising individual active traps. Trap pumping is important because it can be used to probe the release times of traps and improve both our understanding of the defect complexes that form and how to best operate the device. The development of the modern trap pumping technique has allowed for an in-depth understanding of the various trap types in a given CCD technology. Our improved understanding of the underlying physics is an essential step towards the accurate modelling of the damage required for the correction of in-flight images from radiation damaged CCDs.

1.2 Aims and Objectives

Until now, the knowledge gained from trap pumping using the method developed by Hall (11), has been studied on devices irradiated with 6.5 MeV protons. The work in this thesis expands on the particle types studied and the effect of particle energy using the trap pumping technique, improving our understanding of how the space radiation environment can impact detector performance. This thesis therefore aims to answer the following research questions:

1) Does the particle type used to irradiate a device have any effect on the emission time constants found for a single trap species?
2) Does the particle energy used to irradiate a device have a significant effect on the emission time constants found for a single trap species?
3) Are the observed results facility dependent (i.e. is there an influence from secondaries that may be present from scatter in the beamline structure)?

1.3 Thesis Structure

The thesis is organised into eight chapters. Chapter 2 introduces the standard design and operating principals of the CCD. Chapter 3 summarises the sources of radiation in space, the effects of radiation damage for CCDs and the operational impact and mitigation strategies to combat this. Chapter 4 describes the trap pumping technique, starting from its development then providing an overview of most recent trap pumping studies to demonstrate the capabilities of the technique. Chapter 5 presents the findings from two CCDs irradiated with protons at different energies. The trap pumping technique is used to find changes in the defect landscapes and determine whether the spread in parameters for each trap's species is specific to the irradiation energy of the protons used and/or facility used (e.g. from secondaries produced in the beamline structure or beam degradation).

Chapter 6 presents results from multiple devices irradiated with a ^{60}Co gamma source at different doses to compare the interaction type with the spread of parameters found. It shows results indicating

that the trap pumping technique has additional applications in measuring the properties of potential pockets. Chapter 7 compares the different energetic particle interactions of protons, neutrons, electrons and high energy photons. Chapter 8 summarises the outcomes of the thesis and outlines the future work that would be required to further continue this area of research.

1.4 References

1. Amelio GF, Tompsett MF, Smith GE. Experimental verification of the charge coupled device concept. Bell System Technical Journal. 1970 Apr;49(4):593-600.
2. Boyle WS, Smith GE. Charge coupled semiconductor devices (Bell System Technical Journal 1970). Selected Papers on Instrumentation in Astronomy. 1993:475.
3. Boyle W, Smith G, inventors. Buried channel charge coupled devices. United States patent US 3,792,322. 1974 Feb 12.
4. Massey R, Stoughton C, Leauthaud A, Rhodes J, Koekemoer A, Ellis R, Shaghoulian E. Pixel-based correction for charge transfer inefficiency in the Hubble Space Telescope Advanced Camera for Surveys. Monthly Notices of the Royal Astronomical Society. 2010 Jan 1;401(1):371-84.
5. Cropper M, Hoekstra H, Kitching T, Massey R, Amiaux J, Miller L, Mellier Y, Rhodes J, Rowe B, Pires S, Saxton C. Defining a weak lensing experiment in space. Monthly Notices of the Royal Astronomical Society. 2013 Jun 1;431(4):3103-26.
6. Massey R, Hoekstra H, Kitching T, Rhodes J, Cropper M, Amiaux J, Harvey D, Mellier Y, Meneghetti M, Miller L, Paulin-Henriksson S. Origins of weak lensing systematics, and requirements on future instrumentation (or knowledge of instrumentation). Monthly Notices of the Royal Astronomical Society. 2013 Feb 11;429(1):661-78.
7. Corbett J, Watkins G. Silicon Divacancy and its Direct Production by Electron Irradiation. Physical Review Letters. 1961;7(8):314-316.
8. Chen C, Corelli J. Infrared Spectroscopy of Divacancy-Associated Radiation-Induced Absorption Bands in Silicon. Physical Review B. 1972;5(4):1505-1517.

9. Kalma A, Corelli J. Photoconductivity Studies of Defects in Silicon: Divacancy-Associated Energy Levels. Physical Review. 1968;173(3):734-745.

10. Evwaraye A, Sun E. Electron-irradiation-induced divacancy in lightly doped silicon. Journal of Applied Physics. 1976;47(9):3776-3780.

11. Hall D, Murray N, Holland A, Gow J, Clarke A, Burt D. Determination of In Situ Trap Properties in CCDs Using a "Single-Trap Pumping" Technique. IEEE Transactions on Nuclear Science. 2014;61(4):1826-1833.

Chapter 2: The Charge Coupled Device

Charge Coupled Devices (CCDs) are popular semiconductor detectors, ideal for imaging and spectroscopy applications. They were invented in 1969 by Boyle and Smith (1) of Bell labs and their work earned them the Nobel prize in physics forty years later. The technology was initially designed to be a semiconductor-based memory storage device similar to magnetic 'bubble' memory. Not long after its invention it became clear that CCDs were ideal for digital imaging and would go on to replace the vidicon tube system as the imager of choice. This chapter focuses on the operation of the CCD, explaining the structure and the fundamentals of operation including the charge generation, storage, transfer and readout with associated noise sources and relevant measurement techniques.

2.1 The Principals of Operation of a CCD

Figure 2.1 illustrates the internal structure of the CCD labelled with charge transfer directions towards the output electronics. Each step in the process is explained in more detail in the following sub-sections. Images are obtained when incident photons are converted into electron-hole pairs, after-which the electrons are separated and stored under the active gate electrode. A collection of gate electrodes and channel stops define size of the pixel. When all the charge has been collected in the pixel, entire rows of signal are transferred in the "parallel" direction towards the readout register. When instructed, the "serial" readout register moves each row's signal one-by-one towards the output where one charge packet is converted and amplified into a digital signal. The process of transferring rows of charge in the parallel direction into the serial register then reading out each pixel is repeated until the entire image area has been measured.

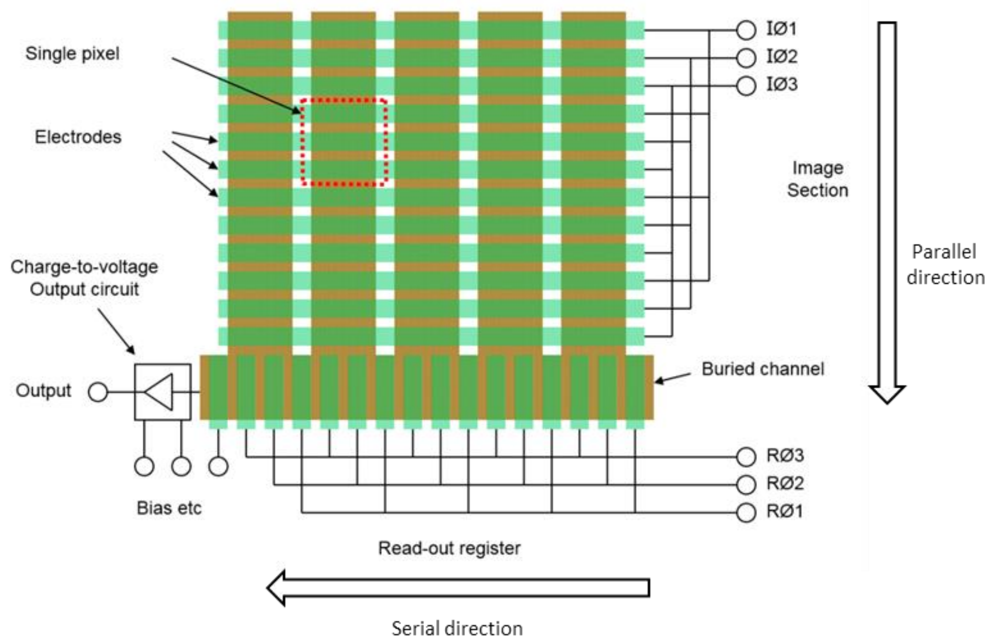

Figure 2.1: Plan view of the CCD illustrating the image area, readout registers and output. Parallel and serial transfers are controlled by voltages applied to the electrodes using image clocks IΦ1-3 and output register clocks RΦ1-3. Buried channels designate the paths the charge packets can travel while clocked under an electrode. A single pixel is three electrodes in this example but there can be more. Electrodes actually overlap in CCDs but are separate here for clarity.

2.1.1 Principal of the pn-Junction

The pn-junction is one of the fundamental building blocks in solid state devices, and describes a region formed at the boundary between n- and p-type regions in a semiconductor. N-type and p-type semiconductors are fabricated by intentionally introducing impurities (doping) to the intrinsic semiconductor. The impurities form ionic bonds with the silicon crystal and modulate its electrical, optical, and structural properties. For n-type silicon, phosphorus is the most common group V "donor" dopant, with five outer shell electrons (one more than silicon), and for p-type silicon, boron is the most common group III "acceptor" dopant, with three outer shell electrons (one less that silicon). When the two material types are brought into contact, electrons diffuse from the n-type material and recombine with holes diffusing from the p-type material. Once equilibrium is reached, an electric field is formed from the charged ions and this resists any further diffusion. This region is known as the depletion region and serves to insulate from the external regions, shown in Figure 2.2. Any electron-hole pairs generated in the depletion region are separated by the electric field and swept in opposing

directions. The depletion region size can be manipulated by changing the quantity of doping in each region and by applying external electric fields.

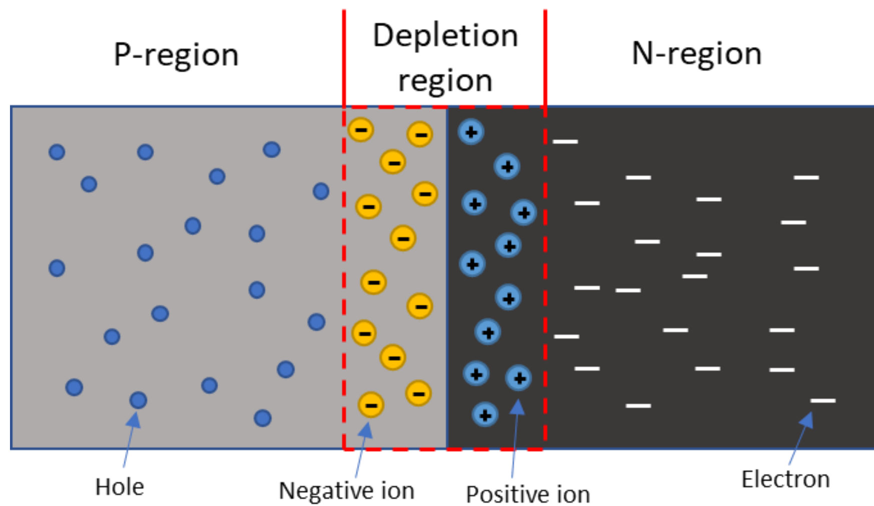

Figure 2.2: The pn junction with n-, p- and depletion regions and no applied voltages.

2.1.2 Charge Collection

After the generation of electrons-hole pairs from incident photons the electrons need to be captured and stored. Modern CCDs are based off the n-MOS capacitor design which is used to store charge. A MOS capacitor is made by layering an insulator and gate electrodes on-top of a p-type semiconductor substrate. By doping the p-type semiconductor region with phosphorus before the electrode is added a pn-junction is formed. This pn-junction buries the depletion region below the surface, which forms a buried channel. This is preferable to MOS capacitors where charge is collected at the surface because the Si-SiO_2 interface has a high density (>10^{10} cm^{-2} eV^{-1}) of interface states which act as trapping sites for signal electrons. The depletion region can be extended through the device with an external electric field supplied from the gate electrodes which can modulate the depth of the charge collection region. A MOS capacitor and its potential profile across the doping layers is shown in Figure 2.3. Photo-generated electron-hole pairs generated in the buried channel are separated by the potentials supplied from the gate electrodes and electrons are stored at the peak in potential.

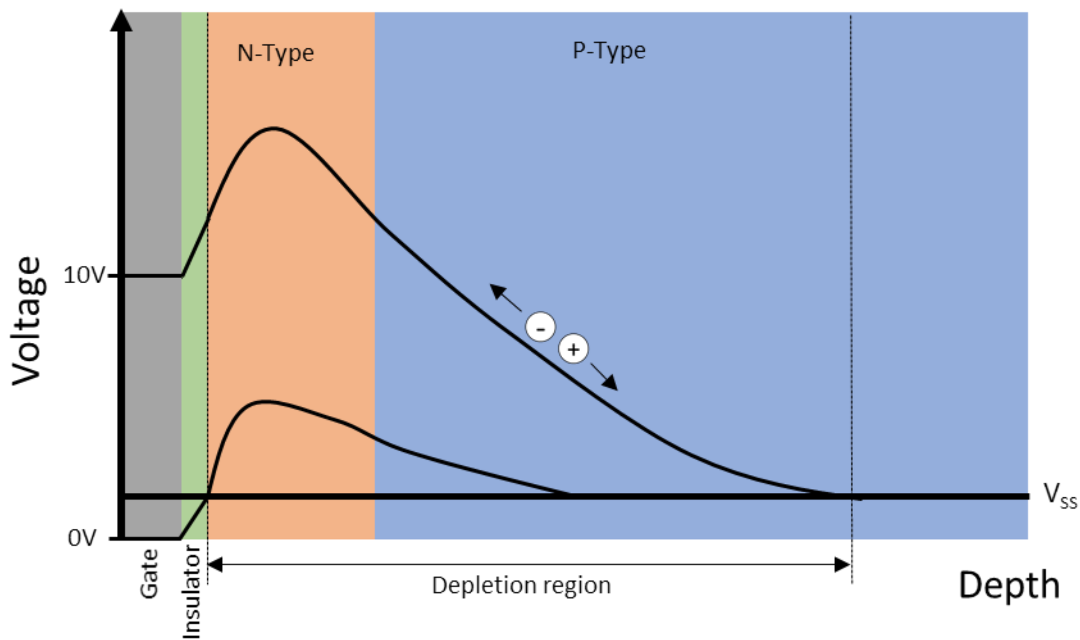

Figure 2.3: Cross section of structure and potential through a buried channel MOS capacitor.

The charge packet storage region is shaped by the potential barrier from the pixel. The charge cloud held under two gate electrodes for a CCD97 pixel is modelled in Figure 2.4 using the program SILVACO. The charge density is greatest in the core of the charge cloud with an exponential drop off in electron concentration towards the edges. The edge density fluctuates from local scattering events, while a restoring force from the electric field keeps the packet relatively well confined (2).

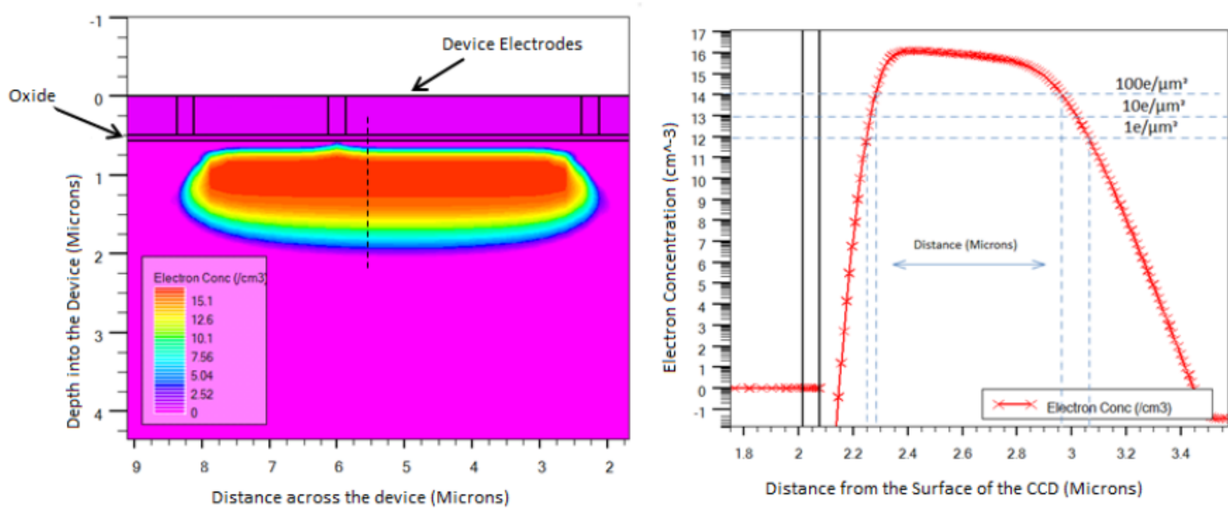

Figure 2.4: Silvaco simulation of the charge packet cross-section in Euclid pixel (left) and the 1-D electron concentration profile against depth (right). Image credit: (3).

2.1.3 Charge Transfer

The charge collected under the gate electrode in a pixel requires transfer through the device towards the output readout circuitry. By sequentially raising and lowering the voltage of gate electrodes at precise timings, the potential wells holding the signal charge change shape and allow for charge transfer, as illustrated in Figure 2.5. The standard transfer process begins by storing the accumulated charge in the potential well of the starting phase, which is insulated by potential barriers to neighbouring pixels. Following storage, raising the neighbouring gate voltage transfers charge to the maximum potential felt between the two electrodes. Adjacent electrode gate structures overlap above the channel, allowing for seamless transfer through the CCD, and transfer requires time of overlapping potentials (t_{oi}) to allow for an efficient charge transfer. The potential well structure and the charge transfer process between two gate electrodes is illustrated in Figure 2.6. Finally, the starting phase voltage is lowered and the signal charge is moved to the neighbouring phase.

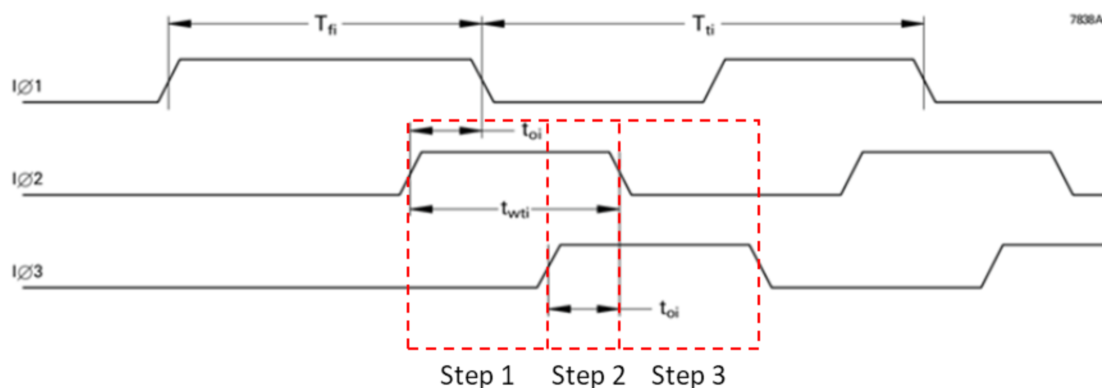

Figure 2.5: Schematic of recommended clocking schemes for a CCD47-20. Image modified to show steps 1,2,3 used in Figure 2.6. Image credit: (4).

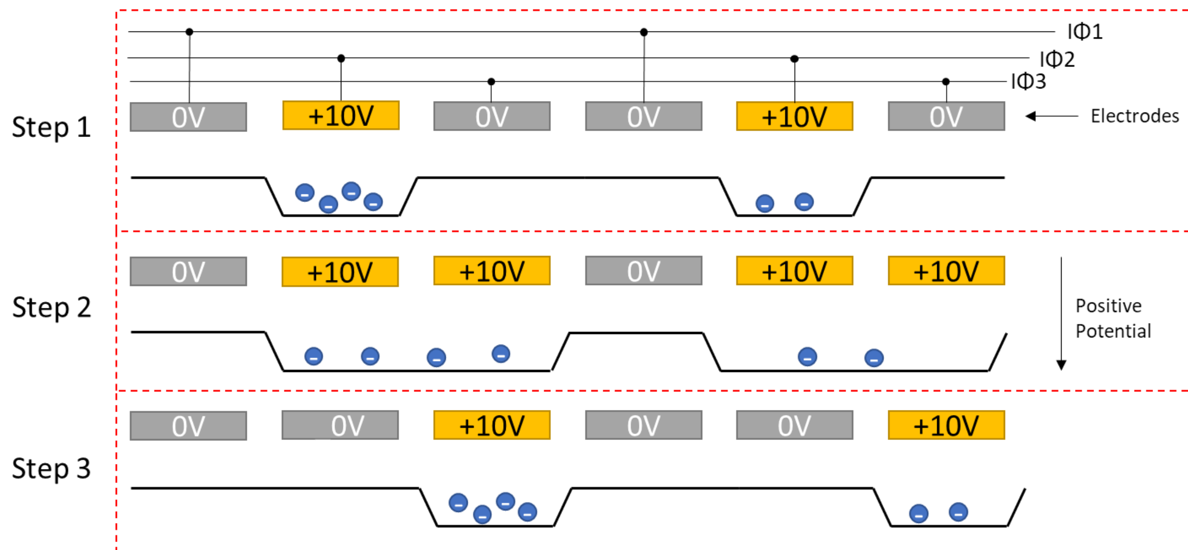

Figure 2.6: Charge transfer following the shape of the potential wells under the gate electrodes for transfer between two neighbouring phases.

2.1.4 The Output Circuit

The output circuit is found at the end of the readout register. A schematic of the output circuitry is shown in Figure 2.7. When the electrons in the charge packets have been transferred to the readout register, charge packets are transferred from the last electrode RΦ3 onto the detection node. The detection node is heavily N doped with a capacitance C_N which connects to both the reset voltage MOSFET and the amplifier. Charge on the detection node results in a voltage which can be sent to the amplifier MOSFET. The voltage is defined as:

$$V = \frac{qN_e}{C_N} \qquad \text{Equation 2.1}$$

Where q is the charge of the electron, N_e is the number of electrons on the detection node, C_N is the capacitance of the detection node. The reset transistor is switched between high and low voltage.

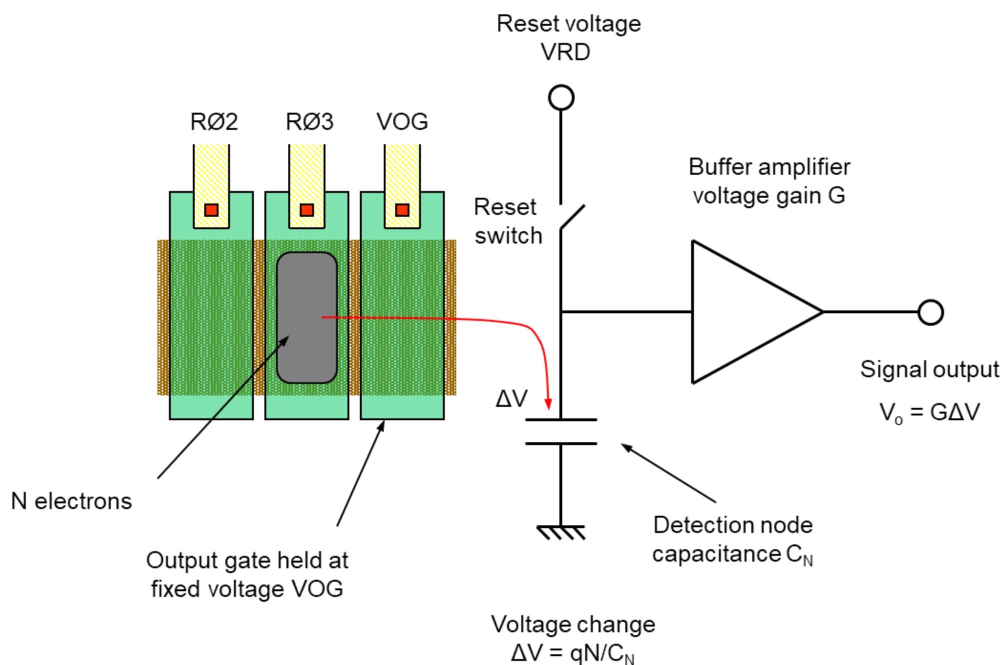

Figure 2.7: Schematic of the end of the serial register and the output circuitry.

After charge is transferred to the detection node and measured by the output circuitry the voltage is reset. This resetting of the detection node voltage introduces Johnson noise from the channel resistance of the reset transistor. The noise found in the reset transistor following a reset is given by Equation 2.2, where Q_n is the Johnson noise voltage on the output node measured in Coulombs rms, k is Boltzmann's constant, T is temperature in kelvin and C_n is the detection node capacitance.

$$Q_n = \sqrt{kTC_n} \quad \text{Equation 2.2}$$

Noise sources including reset noise, Johnson noise and flicker noise from the output circuitry can be heavily mitigated by method known as correlated double sampling (CDS). A basic CDS circuit is shown in Figure 2.8. The signal from the CCD is lightly and linearly amplified in the pre-amp before reference and data signal levels are captured. The output signal is sampled twice, at the reference signal and again at the data signal. The process is used to extract the correct image data of the pixel and removes any low-frequency noise on the output signal.

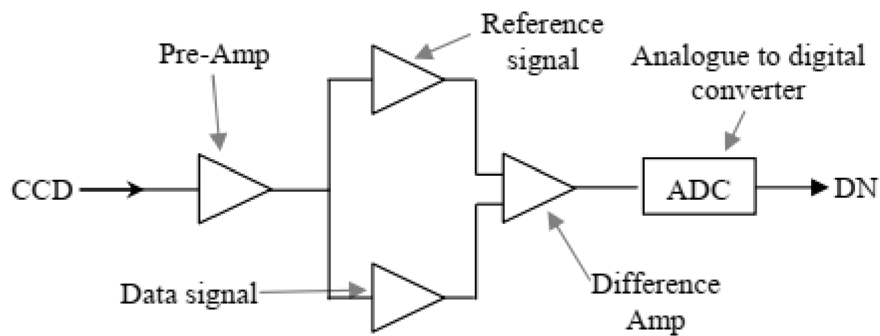

Figure 2.8: Basic CDS circuit schematic. Image credit: (5).

2.2 Noise Sources

Several noise sources arise in the signal chain for a CCD. The three sections of the signal chain are the drive electronics supplying the clocks and bias voltages (system noise), the CCD (read noise) and the signal processing electronics. Any noise generated along that chain that has not been removed is amplified and then sampled by the analogue to digital converter (ADC) to a digital signal. Several of the major noise sources of a CCD can be characterised using a photon transfer curve (PTC) (Figure 2.9) which will be used here to explain the impact of different noise sources.

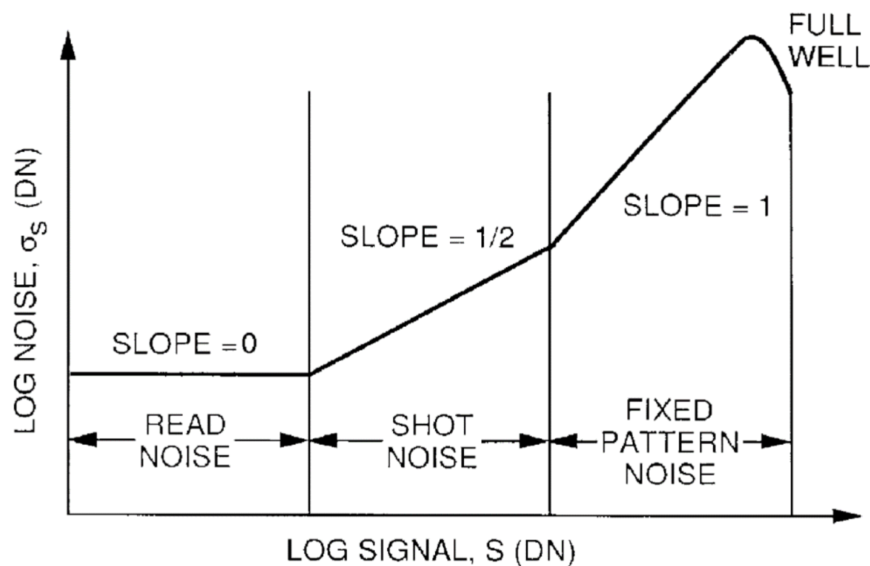

Figure 2.9: Photon transfer curve illustrating noise regimes at varying illumination levels. Image credit: (6).

The first region of the PTC is measured at very low illumination levels where the read noise dominates any signal. Read noise is the remaining analogue noise from the CCD's output stage after reset noise has been removed by CDS. There are effectively two contributions: the CCD output stage's readout noise, and the readout electronics readout noise. This causes uncertainty in charge measurement and is prevalent in images with short exposure times or faint background levels.

As the illumination is increased, the second region of the PTC shows shot noise dominating the noise sources. The generation of photons from a light source is inherently a statistical process. When multiple frames are taken of the same source, the fluctuation of the intensity in each frame follows a Poisson distribution. As this distribution follows Poisson statistics, the noise is proportional to the square root of the signal, and this is why the slope of the PTC is ½.

At higher signals, in the final region of the PTC, fixed pattern noise (FPN) becomes the dominant noise source. FPN arises from the differences in sensitivity between pixels and is directly proportional to the input signal size. This means that each pixel will have a slightly different signal from a uniform illumination. In CCDs FPN appears to be randomly distributed throughout the image area but remains consistent for each specific detector. The PTC now has a gradient of 1 as the fixed pattern noise is proportional to the signal.

2.3 Quantum Efficiency

Quantum efficiency (QE) is a measure of the sensitivity of the CCD to incident photons. It is defined as the proportion of the incident photons which generate signal charge and is typically reported as a percentage. Space telescopes focus on subsets of the full EM spectrum so the CCD can be designed for the best QE at the chosen wavelengths. As shown in Figure 2.10, detectors, such as the CCD47-20 (a typical CCD from Teledyne e2v), can achieve very high QE at visible wavelength; the typical spectral response between 300 and 1100 nm is shown to be as high as 95%. Photons with a wavelength shorter than 300nm typically transfer their energy into the first few microns of the detector before reaching

the depletion region. Photons with longer wavelengths are essentially transparent to CCDs with a low probability of interaction because there is not enough energy to create electron-hole pairs.

A limitation of front-illuminated (FI) devices is that the gate electrode structures can block incident photons. By thinning the back-surface of a FI device and illuminating from the backside, the problem is circumvented as photons will interact with the depletion region first. This is known as a back-illuminated (BI) CCD. A boron implant is added to the new surface to promote charge movement away from the trap-dense back surface. The back surface is polished and highly reflective, so an antireflection (AR) coating is added to improve the QE of the desired wavelengths to be studied. The typical thickness of these devices approaches the depletion depth (typically 13-40µm) and allows for significant improvements for many wavelengths of the QE.

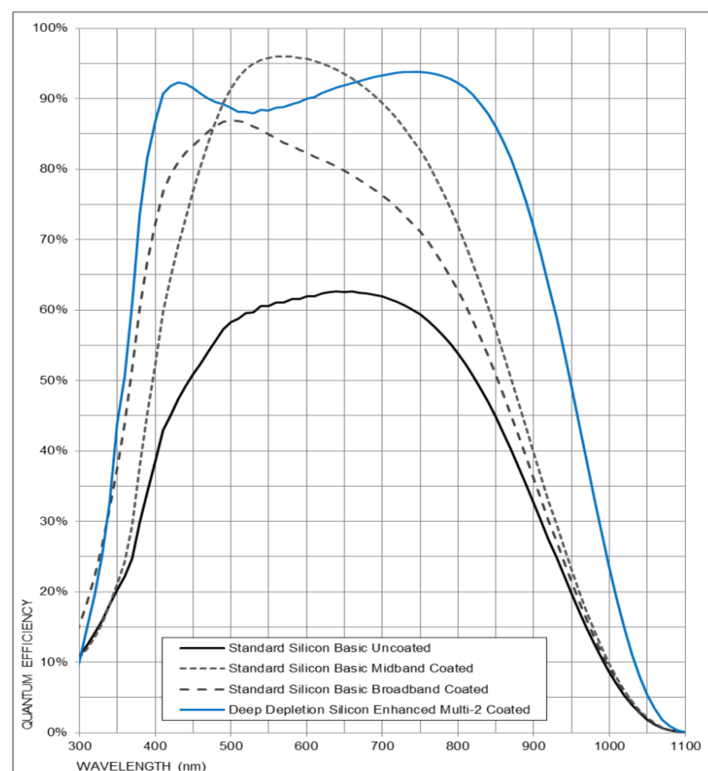

Figure 2.10: Typical Spectral Response of CCD47-20 NIMO device at 243 K. Image Credit: (4).

2.4 Dark current

CCDs can generate signal charge in the absence of light through thermal excitations referred to as dark current. The unwanted signal accumulates during charge capture and is indistinguishable from photo-generated signal. The source of dark current is from electrons having sufficient thermal energy to break free from the lattice, so the majority of imaging satellites operate cryogenically to heavily suppress dark current.

Defects in the silicon are found throughout the CCD, with the highest concentration found at the Si-SiO_2 interface. The interface states have a large distribution of energies, with a mean energy close to the mid-band of silicon at ≈0.5 eV and supplies an "stepping point" for electrons to promote from the valance band to the conduction band. Non-interface dark current sites can be in the depleted material within the potential well or diffusion sources in the bulk material, as illustrated in Figure 2.11.

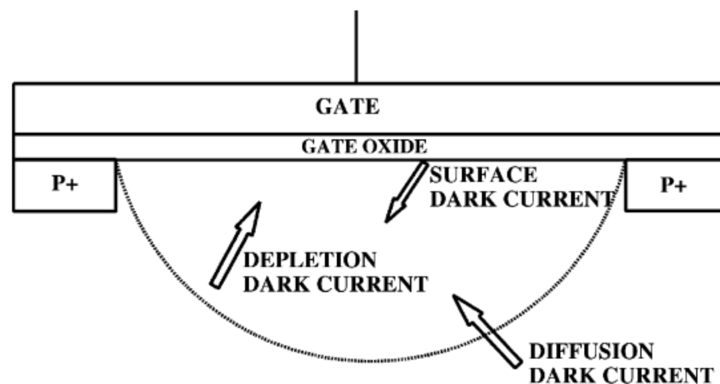

Figure 2.11: Dark current sources within the CCD. Adapted from (6).

Bulk silicon defects present at a much smaller concentration than surface states. These defects can become the dominant source of dark current over the lifetime of a satellite mission. A build-up of radiation induced traps on space-based CCDs such as the instruments on Hubble require annealing to change the configuration of the trapping sites and improve dark current. This is discussed further in the annealing section 3.6. Dark current can be suppressed by running the device in Inverted Mode Operation (IMO). This operating mode inverts one or more gate electrodes during image integration and floods the interface surface with holes, reducing the probability of thermal generation but at the cost of a smaller depletion depth.

2.5 Charge Transfer Efficiency

When charge is transferred between electrodes, there is a chance that some of the signal charge is left behind in low energy traps. Charge Transfer Efficiency (CTE) is a measurement of the fraction of the generated signal that is successfully transferred from each pixel. Charge Transfer Inefficiency (CTI) is the inverse measurement; the fraction that did not successfully transfer, CTI = 1-CTE. Modern scientific detector design and fabrication has advanced to reduce CTI to less than 10^{-5} (7).

The Extended Pixel Edge Response (EPER) and the First Pixel Response (FPR) are two analysis techniques used to measure the charge transfer inefficiency (CTI) of a CCD. Both methods require a flat-field signal, which can be provided by charge injection or an external light source, to supply near-uniform illumination across the image area. The EPER technique overclocks in the serial and parallel directions (reading out overscan pixels) to measure the deferred charge found in the extended pixel regions. EPER is considered to under-measure CTI because traps with long emission times can fail to reemit in the overscan region.

First Pixel Response (FPR) measures the missing charge in the leading edge of the flat field image. The storage region is flushed of charge and then the image region is read out normally, with the leading row losing charge to any traps present through the emptied store region. The measurement is best used with larger charge packets where the trapped signal is a relatively small percentage of the signal, however larger charge packets are known to interact with more traps so there is a trade-off.

Equation 2.3 is used for both FPR and EPER where S_D is the total charge deferred/lost in either FPR first pixels or EPER tail, S_x is the average charge level from the flat field and N_P is the number of pixel transfers from the CCD register (6).

$$CTI = \frac{S_D}{S_x(e^-)N_P} \qquad \text{Equation 2.3}$$

2.6 References

1. Boyle WS, Smith GE. Charge coupled semiconductor devices (Bell System Technical Journal 1970). Selected Papers on Instrumentation in Astronomy. 1993:475.
2. Bush N. The impact of radiation damage on electron multiplying CCD technology for the WFIRST coronagraph. Open University (United Kingdom); 2018.
3. Clarke A, Hall D, Holland A, Burt D. Modelling charge storage in Euclid CCD structures. Journal of Instrumentation. 2012;7(01):C01058-C01058.
4. CCD47-20 Back Illuminated NIMO Frame-Transfer High Performance CCD Sensor. [Internet]. E2v.com. 2017 [cited 15 July 2020]. Available from: https://www.e2v.com/resources/account/download-datasheet/1436
5. Gow JP. Radiation damage analysis of the swept charge device for the C1XS instrument (Doctoral dissertation, Brunel University School of Engineering and Design PhD Theses).
6. Janesick J, Elliott T, Collins S, Blouke M, Freeman J. Scientific Charge-Coupled Devices. Optical Engineering. 1987;26(8).
7. Mostek NJ, Bebek CJ, Karcher A, Kolbe WF, Roe NA, Thacker J. Charge trap identification for proton-irradiated p+ channel CCDs. InHigh Energy, Optical, and Infrared Detectors for Astronomy IV 2010 Jul 16 (Vol. 7742, p. 774216). International Society for Optics and Photonics.

Chapter 3: Radiation Damage Effects on CCDs

In 1968 the first successful space telescope was launched, the Orbiting Astronomical Observatory (OAO-2), which demonstrated that space-based observations were the future of astronomy (1). During the 1970s and early 1980s, NASA sent satellites equipped with vidicon tubes for observations, a type of camera based on cathode ray tube technology. Missions including Surveyor, Ranger, Mariner, Viking, and Voyager used vidicon tube technology as the primary imaging method until solid-state image systems superseded their performance. The technology was useful for missions that observed planets and their moons but lacked the sensitivity, stability and long-term reliability necessary for the scope of future missions (2). The first L-class mission to incorporate a CCD in space was the Large Space Telescope (LST), later renamed to the Hubble telescope, which launched in 1990. By this point, the CCD had surpassed the cathode ray technology and began to make a considerable impact on astronomical observations. The introduction of the CCD into space-based observations provided new challenges from the radiation environment. The previous generation's vidicon tubes had a near-perfect radiation hardness due to a lack of local electronics, whereas CCDs are highly susceptible to radiation damage.

3.1 The Space Radiation Environment

The radiation environment of space is highly complex and dynamic, with three primary factors affecting missions including solar activity, galactic cosmic rays, and the trapped particle magnetosphere interaction, Figure 3.1. In our efforts to predict radiation damage in CCDs, we need to understand the impact of particle type, flux, energy and the variation of space environments.

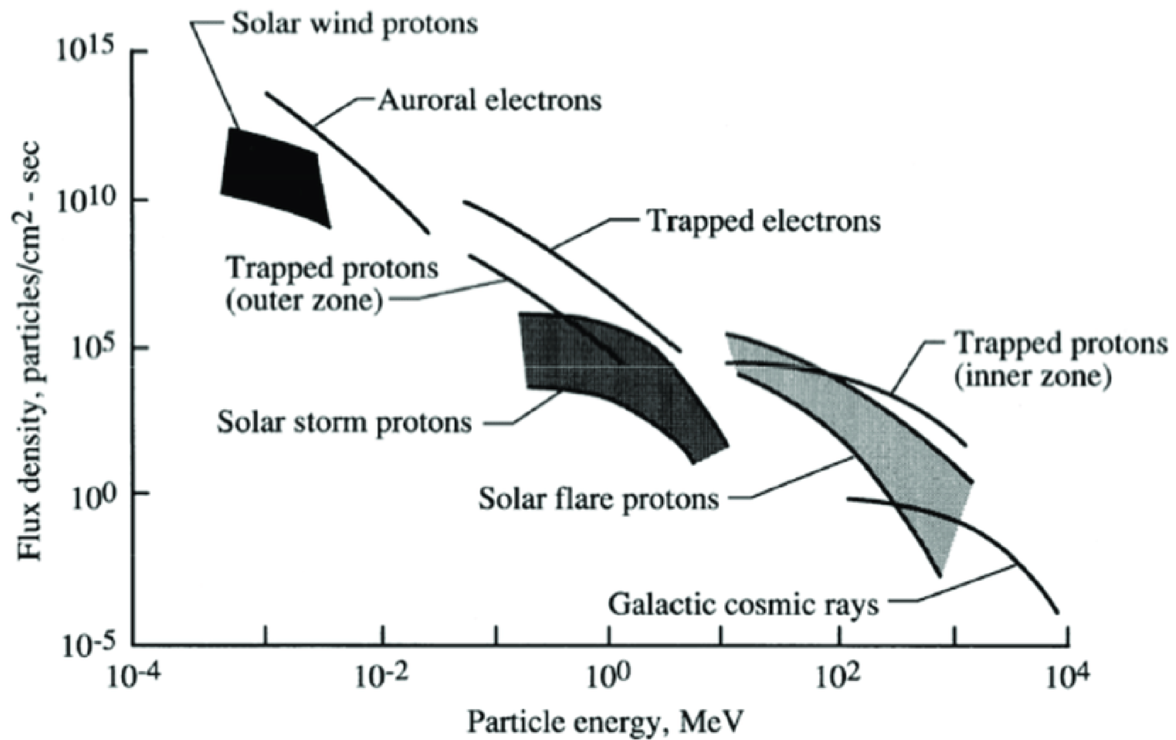

Figure 3.1: Estimated free space radiation environment. Image credit: (3).

3.1.1 Solar Activity

The Sun contributes the majority of radiation that space-based missions encounter but the radiation environment varies with specific orbit. Solar activity encompasses three phenomena: solar wind, solar flares and Coronal Mass Ejection (CME), each contributing to the radiation environment. The solar wind is the most abundant radiation type in the solar system, an energetic plasma of protons, electrons, alpha particles and a small proportion of heavier elements.

A solar flare describes a sudden bright flash from the Sun which is typically accompanied by a CME. The accelerated particles emitted are, on average, more energetic than the standard solar wind. CMEs are significant ejections of magnetised plasma and EM radiation which accompany the solar wind consisting primarily of protons and electrons. These highly energetic ions move as an Alfvén wave, a type of magnetohydrodynamic wave of oscillating ions in the presence of a strong magnetic field. The speed of CME ejected particles is slow relative to EM radiation, so a large number of satellites and observatories are specifically designed to monitor the sunspot activity daily and provide an early

warning system of major solar events approaching Earth. Such missions include the Solar and Heliospheric Observatory (SOHO) spacecraft, the Solar Dynamic Observatory (SDO) which studies the solar atmosphere and the Advanced Composition Explorer (ACE). The fastest possible CME event emits particles at near 3000 km/s and is estimated to take 15+ hours to reach Earth (4). The cycle predicts as many as three solar flares/CME eruptions a day can be observed during the activity maxima of the Sun and as few as once a week during its minima, Figure 3.2. The solar cycle is predicted to reach another minimum, like the Dalton minimum, following the modern maximum period; however solar activity is still poorly understood.

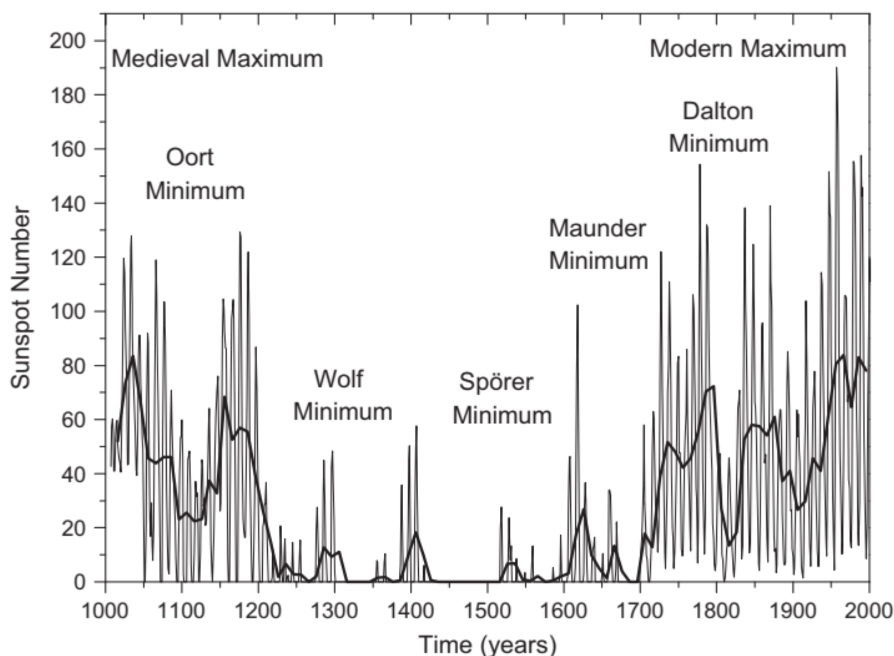

Figure 3.2: Yearly average number of sunspots from 1007-2006. Image credit: (5).

3.1.2 Galactic Cosmic Rays

Galactic Cosmic Rays (GCR) are high-energy charged particles that originate from extra-heliospheric sources at a flux that modulates in anti-correlation with the solar wind (6) with an eleven-year cycle. The composition of the cosmic ray spectrum is approximately 89% protons, 10% alpha particles, 2% electrons with the remainder consisting of heavier nuclei and positrons. The GCR spectrum represents

the majority of high energy particle interactions a mission encounters, ranging from tens of MeV to energies exceeding 10^{20} eV.

On Earth, the majority of GCRs collide with the stratosphere to produce secondary events of muons, protons and electrons which are detectable by ground-based CCDs. In space, the absence of an atmosphere means the satellite is subject to the full spectrum of GCR particles. The high energy particles, though low in flux, can penetrate shielding and produce secondary events that can damage the detector. The GCR background energy spectra flux is modulated with solar activity and is shown at 1 AU in Figure 3.3 which indicates that damage can fluctuate through the 11 year solar cycle.

Attempts have been made to model the GCR spectrum. The Cosmic Ray Effects on Micro-Electronics, also known as CREME96, is one of the most popular modelling programs and was developed by The Naval Research Laboratory. The program uses numerical models of the ionizing radiation environments in near-Earth orbits and estimates the Linear Energy Transfer (LET) radiation environment for missions.

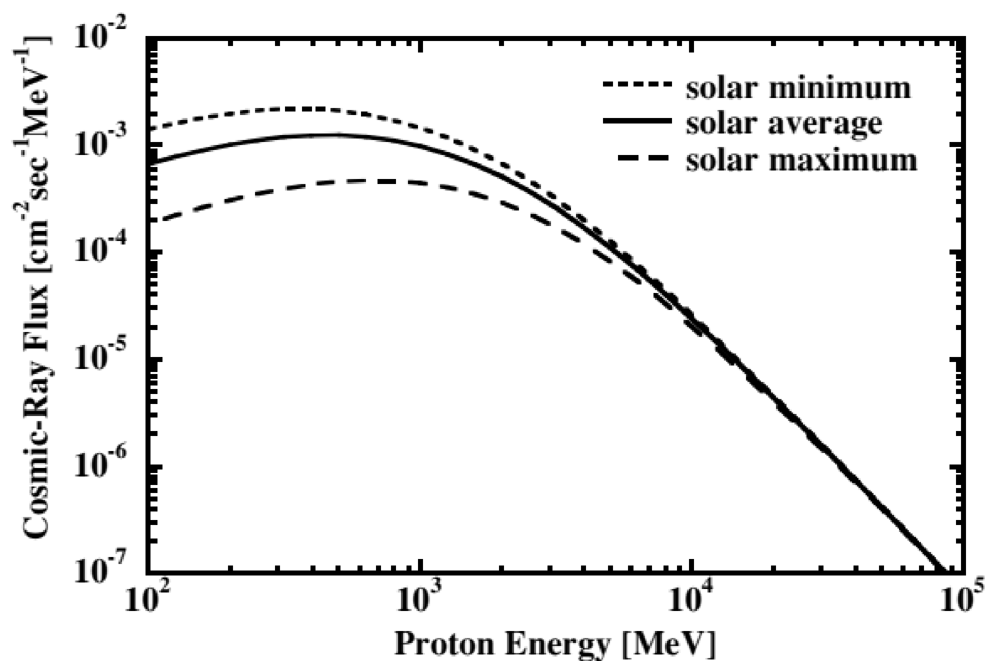

Figure 3.3: Energy spectra of GCR protons at 1 AU. Image credit: (7).

3.1.3 Planetary Considerations

An essential consideration for a space mission is the choice of an appropriate orbit, or fly-by route of a planet, to achieve the scientific criteria of the mission while ensuring the longevity of its equipment. Planets with a strong magnetic field are capable of trapping and concentrating charged particles in radiation belts, known as Van Allen Belts and include Earth, Jupiter, Saturn, Uranus and Neptune. Satellites orbiting these planets receive a concentrated radiation dose from charged energetic particles when travelling through the Van Allen Belts. The final magnetosphere shape is a combination of the planet's magnetic field interacting with the solar wind where the majority of trapped particles originate.

The Earth has a complex magnetosphere and its interaction with the solar wind can directly affect the radiation belts. The solar wind compresses the shape of the magnetosphere on the dayside to tens of Earth radii and stretches on the night side to hundreds of Earth radii (8). The inner Van Allen belt stretches from 400 to 6000 miles and the outer belt stretches from 8400 to 36000 miles above the surface (9). The flux of trapped protons, shown in Figure 3.4, changes with distance from the Earth's surface at each energy level.

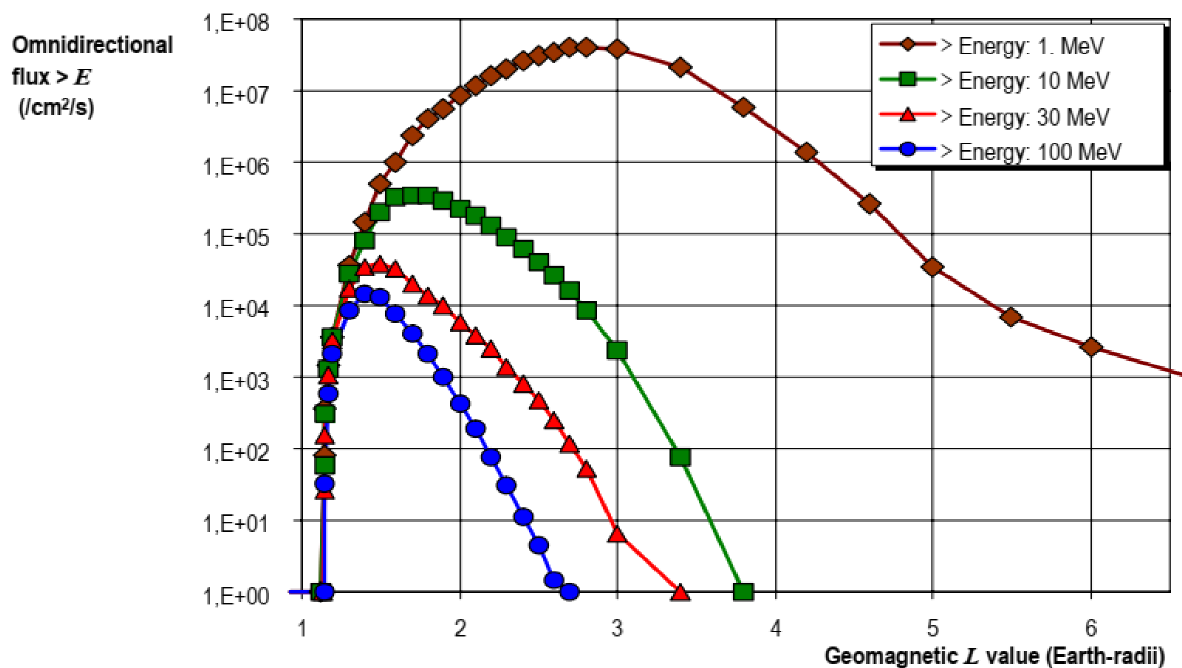

Figure 3.4: Proton flux variation with distance on the geomagnetic equator orbiting Earth for various energy thresholds. Image credit: (10).

The radiation environment from trapped particles in the Earth's magnetosphere is at its most extreme at the South Atlantic Anomaly (SAA). The Earth's magnetic dipole is slightly offset from the Earth's centre by roughly 400 miles. The region, which extends from the East Pacific to South Africa, represents the entrance of the highest energy particles trapped in the belt. The region has a radiation environment orders of magnitude higher than any other location across the magnetosphere. Missions that pass through the region, such as the Hubble Space Telescope (Low Earth Orbit), are usually forced to suspend data acquisition due to the severity of the radiation.

Missions attempting to orbit Jupiter, such as the ESA JUICE mission, will encounter the largest and most powerful planetary magnetosphere in the solar system. The first missions to directly study the magnetosphere were Pioneers 10 and 11 (1973-1974) which received ten times the predicted dose (11). The radiation environment was so extreme that images of Io, one of the moons of Jupiter, were corrupted. Voyager 1 and 2 (1979-1980) were designed to be more radiation hard to cope with the radiation environment. Despite the preparation, the passing through the plasma torus massively degraded the sensors and degraded images of Io and Ganymede. The Galileo spacecraft orbited

Jupiter from 1995-2003 at a distance of one-hundred Jupiter radii so the instruments on-board could survive the radiation environments. The challenge of orbiting Jupiter is the abundance of high energy electrons that are highly effective at creating secondary electrons in interactions with the spacecraft, Figure 3.5.

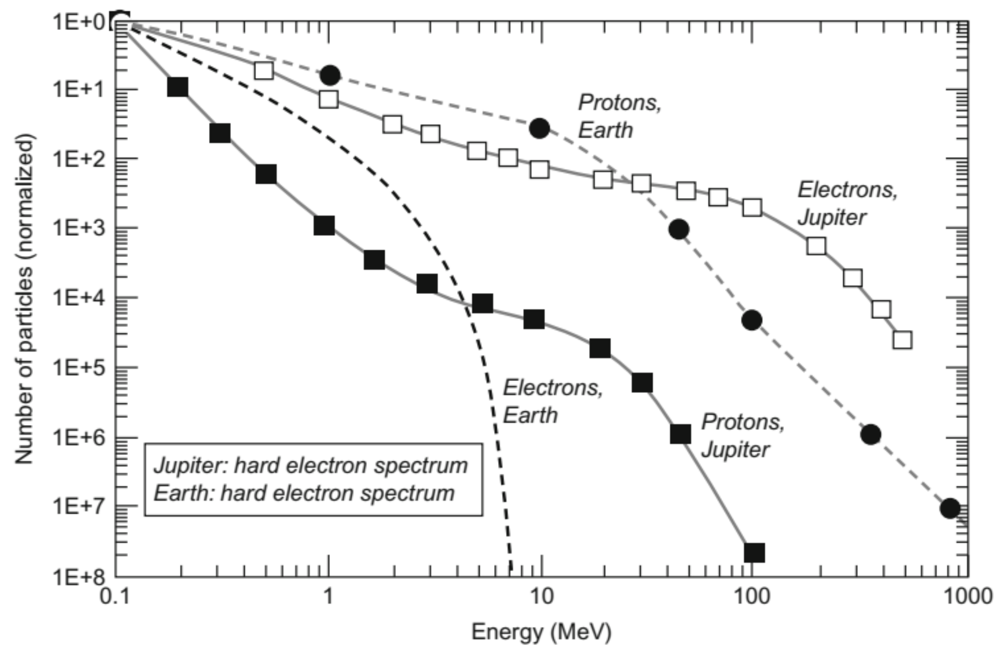

Figure 3.5: Radiation environment differences between Earth and Jupiter for electron and proton energies and fluxes Image credit: (12).

3.2 Stopping Power

To simulate the space environment and test the expected performance in orbit, we irradiate CCDs with individual particle types such as protons, neutrons and high energy photons, at various energies and fluences. Different particle types lose their energy in a variety of interactions, either through ionisation damage, displacement damage or a combination of the two.

The stopping power is a measure of a material's ability to slow down energetic particles. Several factors impact the absorbed dose, including radiation type, energy level, mass, charge and target flux density. Absorption of energy comes from two phenomena: electronic stopping and nuclear stopping. Electronic stopping power describes the inelastic collisions between bound electrons and nuclear

stopping power describes the elastic collisions between an ion and target atom, changing direction and results in energy loss of the ion. Different particle types, protons, neutrons, electrons and EM radiation all interact differently depending on the charge state, mass and energy. As the energy level of each type of radiation changes different absorption methods dominate.

The stopping power for low and high energy protons in silicon is shown in Figure 3.6, demonstrating the non-linear nature of the electronic and nuclear components to the total stopping power and a dominance of the electronic stopping power throughout the energy range. The penetration depth of a 1 MeV ion is typically in the micrometre range, close to the depletion layer and observable by a CCD assuming electron-hole pair production through electronic stopping. The electronic stopping power dominates energy loss through silicon, and as protons become more energetic, they are less likely to interact through nuclear interactions.

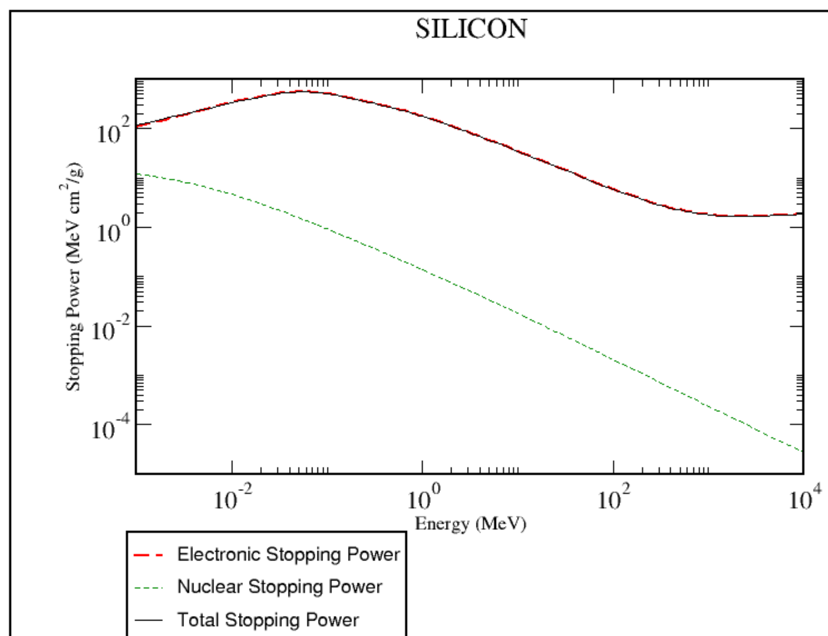

Figure 3.6: Stopping power for protons in silicon (13).

As a proton increases in energy, the total stopping range increases requiring more substantial shielding to absorb higher energy events consistently, Figure 3.7. Weight restrictions on satellites and

a lack of physical space around the detectors means careful consideration is taken in choosing the type of materials, the density and the thickness of these shields.

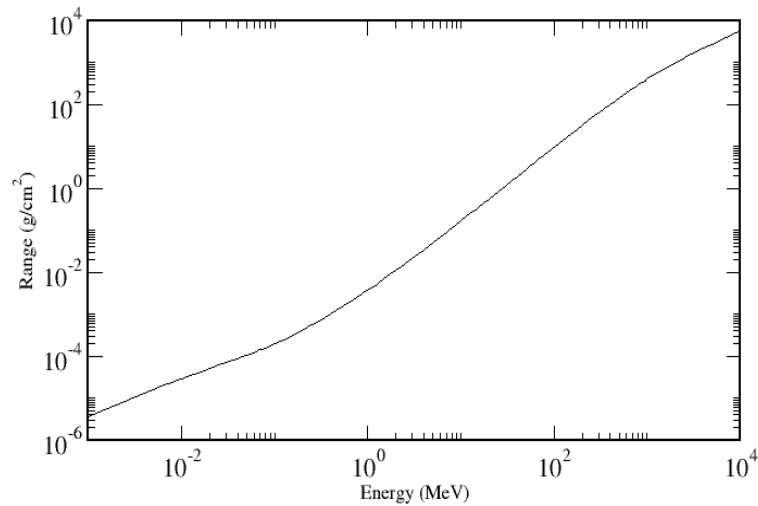

Figure 3.7: Stopping range for protons at different energies (13).

At high energies of EM radiation (e.g. X-rays and gamma rays) Compton scattering dominates, where high energy photons transfer part of its energy to the electron and eject the electron from the atomic orbit. The secondary electron emitted from the Compton event is capable of both electronic and nuclear interactions. Nuclear interactions are possible as the electron has a mass component. For high energy gamma rays, pair-production dominates by forming electron-positron pairs. The process occurs locally to the atomic nucleus to absorb recoil momentum. Pair production requires a minimum energy transfer of 1.022 MeV, sufficient for two-electron masses. The type of interaction can determine the damage mechanism that the silicon is likely to receive, Figure 3.8.

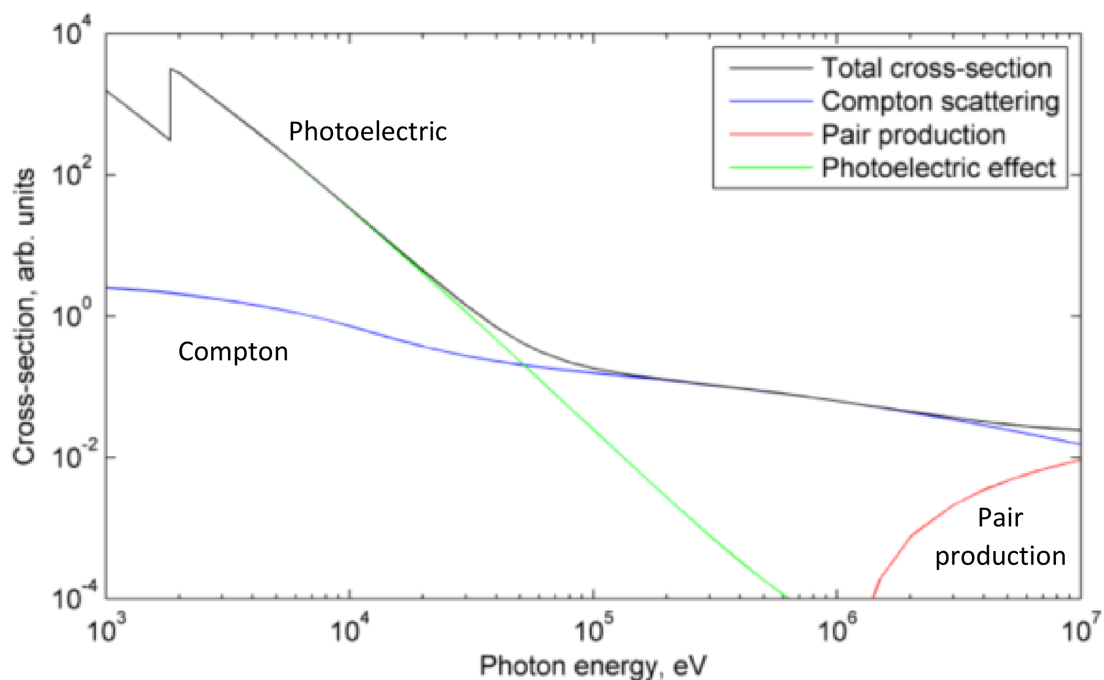

Figure 3.8: Cross-section interactions with silicon for photons (13).

3.3 Ionisation Damage

The electronic stopping effect from energetic interactions manifests as ionising radiation damage through the CCD. Ionisation damage has different performance impacts based on the region of the CCD that absorbs the energy which includes: the surface, gate structures, buried channel or bulk silicon. The particle type and incident velocity determine the energy and depth at which absorption is expected to occur. A proton, for example, loses the majority of its energy through Coulombic interactions with the lattice (≈99%), generating electron-hole pairs along its path by exciting shell electrons from the lattice to the conduction band.

3.3.1 Gate Dielectric Damage

Ionisation damage causes a flat-band voltage shift in the surface regions, changing the effective voltage applied to a CCD. In the surface regions of n-channel front-illuminated devices, generated e-h pairs separate and electrons are attracted to the positive bias of the gate structure. Electrons are highly mobile and escape the gate electrode, while holes are less mobile and slowly move away from

the gate to the Si-SiO interface, becoming trapped. Holes that failed to recombine can be trapped for long periods. The sheet of holes are positively charged and work against the positive voltage of the gate, requiring the clock and output amplifiers to run at higher voltages.

To reduce the impact of oxide charge accumulation, devices requiring negatively biased gates typically contain a thin nitride layer in-between the gate and the Si-SiO_2 interface. Holes are most likely to either recombine through reducing the mobility of the electrons or to settle at the SiO_2-Si_3N_4 interface (14).

A typical flat-band shift for flight devices from the 1980s was approximately -0.1 V per krad in silicon (2). Over the last 30 years however, there has been an improvement in the understanding and mitigation of ionising damage. Radiation-hard devices have demonstrated an improvement in flat-band voltage shift where standard devices typically range from 100-200mV/krad. In contrast, radiation-hard devices are capable of ≈6 mV/krad and a reduction in the surface dark signal (14). Methods of improving radiation hardness include thinning the gate dielectric, thus reducing the size of the trapping region but reducing the maximum voltage and may fail to insulate the surface states fully.

3.3.2 De-passivation and Surface Traps

Passivation is a step in the CCD manufacturing process that introduces hydrogen to fill dangling bonds at the SiO_2 gate insulator interface rendering them inactive, Figure 3.9. Radiation damage is believed to de-passivate the region, freeing hydrogen molecules and returning the surface state into "dangling bonds". Current theories suggest that holes can liberate hydrogen surface bonds that diffuse into the interface and release additional hydrogen, creating H_2 gas which escapes from the CCD. The process is irreversible for a flight-based mission. Potential mitigation techniques include using a pinned or inverted mode CCD or running very cold to reduce dark signal. The long-term de-passivation process is known as reverse annealing because it increases dark current and shifts the flatband voltage. The

Cassini Star Tracker CCD experienced reverse annealing following irradiation and forced engineers to a change of operating temperature from -90°C to -40°C to better manage the CTE degradation (2).

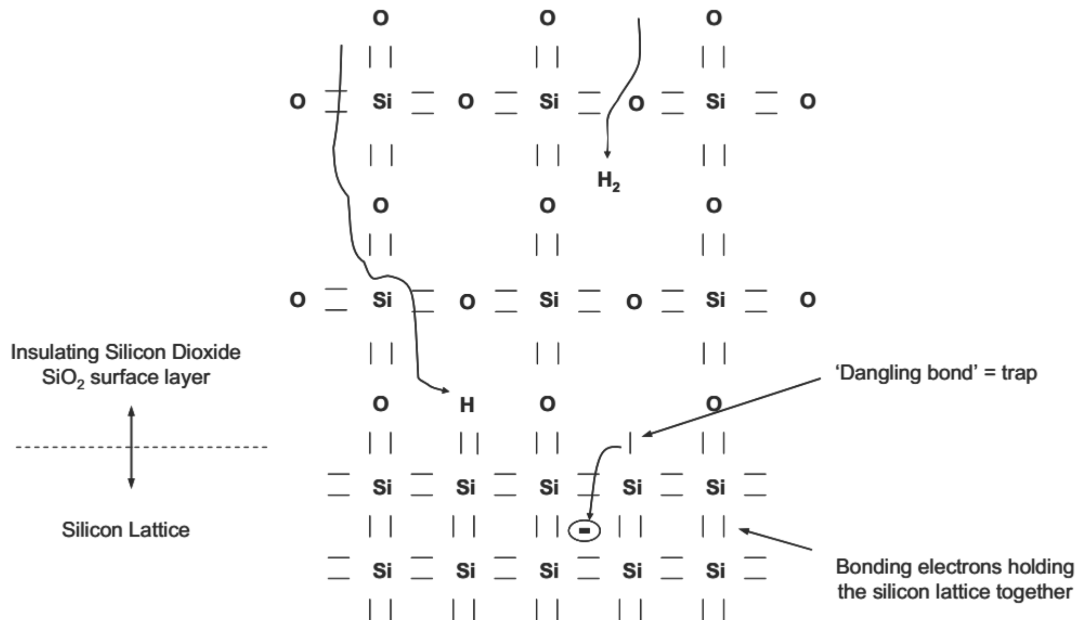

Figure 3.9: Passivation of the silicon surface oxide layer. Image Credit: (14).

3.4 Displacement Damage

Detectors used in the space environment are subject to displacement damage, caused by particles that collide and displace silicon atoms from the crystal lattice and create vacancy-interstitial pairs. A lone vacancy is mobile in the lattice and while most vacancies will recombine, some can form stable defects. These defects have energy levels within the silicon band gap and are capable of trapping majority and minority carriers, which can increase Charge Transfer Inefficiency (CTI) and increase dark signal. The impact of displacement damage is one of the most significant challenges facing high accuracy scientific imaging as the landscape of defects (or traps) evolves throughout the operational lifecycle of the CCD.

Displacement damage is caused by the collision of an incident charged particle or neutron, displacing a silicon atom from its lattice site. The displaced silicon atom, known as a Primary Knock-on Atom (PKA), moves with sufficient energy to either come to rest in an interstitial position in space between

the crystal lattice or cause a chain reaction until the energy of the knock-on atom is too low for further displacements. The displaced atom and the vacancy together are known as a Frenkel pair. Displacement damage introduces two types of defects into the CCD, point defects and clusters of defects.

3.4.1 Point Defects

Point defects are localised disruptions to the otherwise perfect crystal lattice structure. Electrons and photons at the 1 MeV range are expected to produce point defects, relatively isolated from one another, while a 1 MeV neutron gives rise to many defects in near proximity. There are three main types of point defects: vacancies, interstitial defects or substitutional defects.

A vacancy site is the absence of an atom from its normal lattice position. A single vacancy can migrate through the lattice if it has sufficient energy. The energy necessary for a vacancy to migrate through the lattice and overcome potential barriers comes from a combination of thermal, illumination excitation and electric field interaction. The vacancy migrates through the lattice until it finds an energetically stable configuration, typically pairing to oxygen, phosphorous or another vacancy.

A stable defect species commonly found in irradiated CCDs is the double-vacancy pair configuration known as a divacancy. The divacancy has been extensively studied over the last 50 years and is considered one of the major trap species due to its relative abundance in CCDs, its impact to the operation of both n- and p-channel CCDs, and its stability at room temperature. Techniques used to study the defect include Electron Paramagnetic Resonance (EPR) (15), infrared (IR) spectroscopy (16), photoconductivity (17) and Deep-Level Transient Spectroscopy (DLTS) (18). An isolated vacancy or pair of vacancies can occupy five different charge states in the silicon band gap (V^{--}, V^{-}, V^{0}, V^{+}, V^{++}), (19) with three different levels introduced into the forbidden gap. The change in electronic configuration from electron capture causes local shifts in the lattice structure around the vacancy because of the Coulombic repulsion force, which increases for each captured electron. A vacancy that neighbours a

dopant or impurity is a defect-impurity complex. The typical vacancy defects found in CCDs are presented in Table 3.1.

Table 3.1: Typical vacancy related defects species present in CCDs and their respective energy levels and temperature stability. Energy levels in the table are listed as E_V + for hole traps with energy levels above the valance band and E_C – for electron traps below the conduction band.

Defect	Description	Energy level (eV)	Annealing Temperature	Source
V	Vacancy	N/A	< 150 °K	
V-V	Divacancy	$E_V + 0.21$ $E_c - 0.41$ $E_c - 0.23$	600 °K	(15)
V-O	A-center	$E_c - 0.16$	600 °K	(20)
P-V	E-center	$E_c - 0.45$ $E_v + 0.27$	350-450 °K	(21) (22)
B-V	Boron Vacancy	$E_V + 0.31$ $E_V + 0.37$ $E_V + 0.13$	260 °K	(23)

There are numerous interstitial defect states possible in silicon. A self-interstitial atom for a CCD is a silicon atom outside its normal lattice position. Common impurity related defects include the implanted dopant ions from group-III (boron) and group-V (phosphorous). Other non-silicon/dopant atoms can enter either through the manufacturing process or implanted from radiation damage as interstitial or substitutional atoms. A substitution impurity atom is an atom of a different type to the bulk material that occupies one of the lattice sites of a bulk atom. Interstitial configurations that might be expected in a CCD are presented in Table 3.2. Impurity concentration correlates to the quantity of interstitial defects, which increase in population with additional displacement damage events. Figure 3.10 visualises different types of defect in the $\langle 100 \rangle$ plane of a silicon lattice.

Table 3.2: Typical interstitial defects species present in CCDs and their respective energy levels, charge state and temperature stability. Defects with multiple energy levels have metastable structural transformations. (E) and (H) are the electron and hole emission activation energy and (ME) and (MH) are metastable alternative configurations. Subscripts i and s represent interstitial and substitutional atoms (24).

Defect	Energy level (eV)	Annealing Temperature
$(Si)_iO_i$	-	230 K
B_i	$E_V + 0.13$ $E_c - 0.45$	240 K
B_iB_s	0.30 (H)	>400 °C
B_iO_i	0.26 (E)	150-200 °C
B_iC_s	0.29 (H)	400 °C
C_i	$E_c - 0.12$ $E_V + 0.27$	50 °C
C_iC_s	$E_c - 0.17$ (ME) $E_c - 0.10$ (ME) $E_V + 0.09$ (MH) $E_V + 0.05$ (MH)	225 °C
C_iP_s	$E_c - 0.30$ (ME) $E_c - 0.29$ (ME) $E_c - 0.23$ (ME) $E_c - 0.21$ (ME)	125 K
C_iO_i	$E_V + 0.36$	400 °C

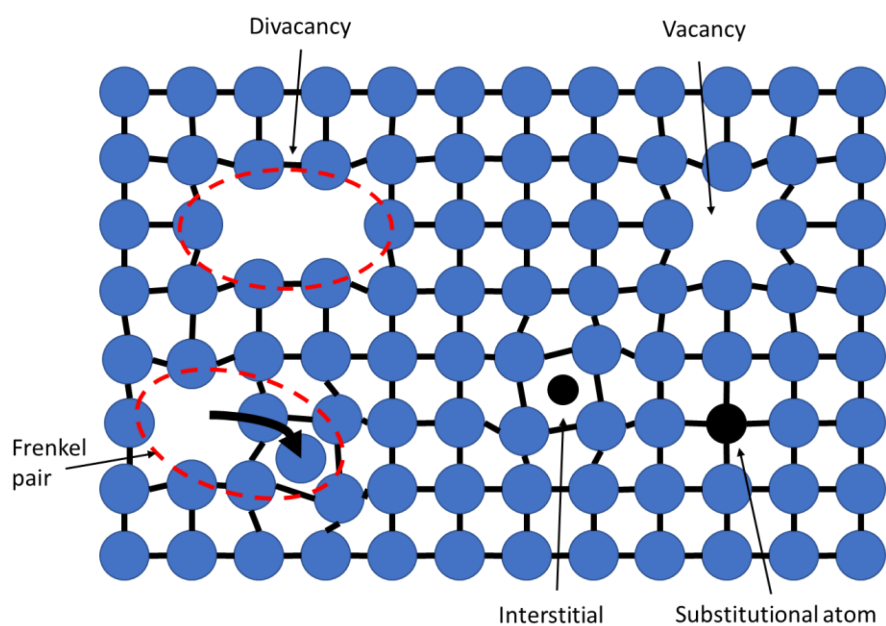

Figure 3.10: Visualisation of various defect species in a $\langle 100 \rangle$ plane of a crystal silicon lattice.

For displacement damage to create Frenkel pairs, damage sources need to exceed the threshold energy of silicon in a crystal lattice, and there is much contention in the literature for this threshold. The threshold displacement (Td) energy is the minimum recoil energy necessary to displace a silicon atom from a regular lattice position. In silicon, the average Td is typically quoted as ≈21 eV, varying with temperature and Fermi level. Both were found experimentally (25,26) and in simulations (27) for $\langle 100 \rangle$ silicon.

The direction of irradiation on the silicon can change the Td necessary for displacement events. Holmström states that Td is poorly known in Silicon and that experimental methods show a widely varying scale of results for Td in the range of 10 – 30 eV has been shown in independent studies from Loferski (28), Corbett (25) and Hemment (29). More recent studies narrowed the variation of threshold displacement energy to be plane dependant. In Holmström (27) the $\langle 100 \rangle$ plane has a threshold energy of 20±2 eV in contrast to the $\langle 111 \rangle$ plane with a Td of 12.5±1.5 eV. The change in threshold displacement energy would affect trap production for low energy irradiations. The reason for threshold variation is still unclear. Damaged local regions could be assumed to have lower threshold displacement energy requirements as there are fewer stable bonds necessary to break to displace a silicon atom.

3.4.2 Cluster Defects

Cluster defects may be roughly classified as three or more displacement events from a single particle interaction (two displacement events can still form a divacancy which is classified as a point defect). However, it is more commonly used to describe many localised defects, mainly vacancies and interstitials in a spherical volume with a radius of ≈150-200 Å containing ≈10^5-10^6 atoms (30). Cluster defects are known to have an enhanced recombination effectiveness compared to isolated defects and is predicted to be independent of impurity levels and oxygen concentrations, with recombination dominated by non-impurity related defects such as divacancies (31).

For the solid-state community, the knowledge of clustering relative to point defects is very limited because of the difficulty to simulate such large damage sites computationally. For protons in the 6-20 MeV range, it is predicted that nuclear elastic interactions dominate displacement events, introducing single cascade events and at energies higher than 20 MeV, proton interactions are dominated by nuclear reactions as detailed in investigations by Wood (32) and expanded on by Srour (31), Figure 3.11. Energetic neutrons only interact through nuclear reactions resulting in very few events and a high energy silicon knock-on atom which can produce dense cascades of silicon interstitials and vacancies. Neutrons can cause cluster defects at considerably lower energies, potentially a few MeV.

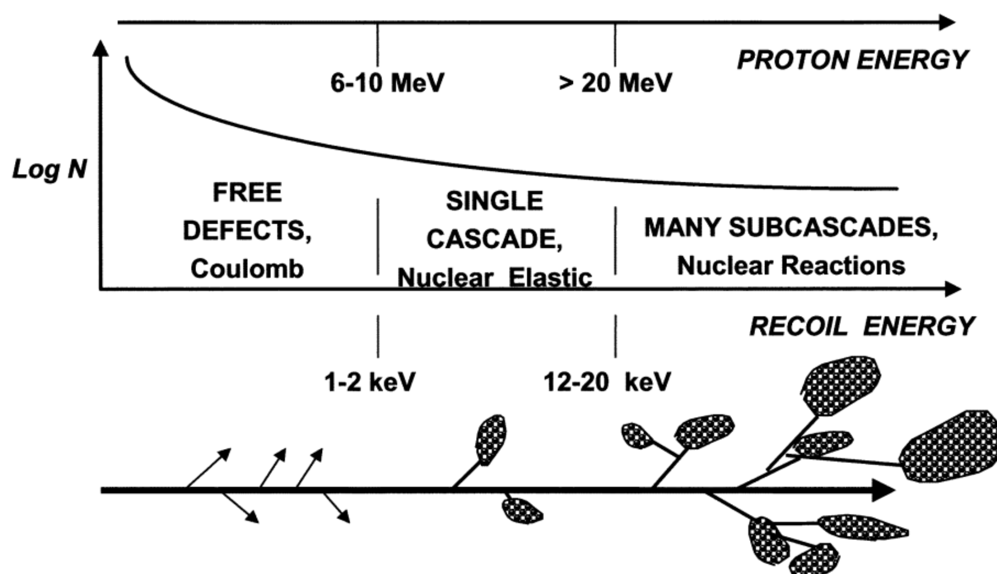

Figure 3.11: Displacement damage threshold for energetic proton interactions and the type of damage they produce. Image credit: (32) and adapted in (31).

3.4.3 The Operational Impact of Defects on CCDs

While the radiation environment of space leads to the formation of defect complexes through displacement damage, the CCD wafer inherently consists of many defects through the production cycle. The wafer fabrication of silicon fails to grow as a perfect crystal, with necessary steps such as ion implantation and back-thinning introducing impurities into the device. Lattice vacancies and impurities degrade the performance of the CCD through increases in CTI and dark signal.

Of course, in a CCD where doping is necessary for operation and the pn-junction location for the depletion layer has an abundance of p-type and n-type material, dopant impurity based traps are frequent. A common defect in n-channel irradiated CCDs is the E-centre, a phosphorous-vacancy pair. The defects, following their initial displacements, reorder to the most energetically stable configurations. This re-ordering of defects is known as annealing and is dependent on temperature. Figure 3.12 shows a range of defect types in silicon, how defects warp the regular atomic structures and their respective electrical levels in between the conduction/valance bands.

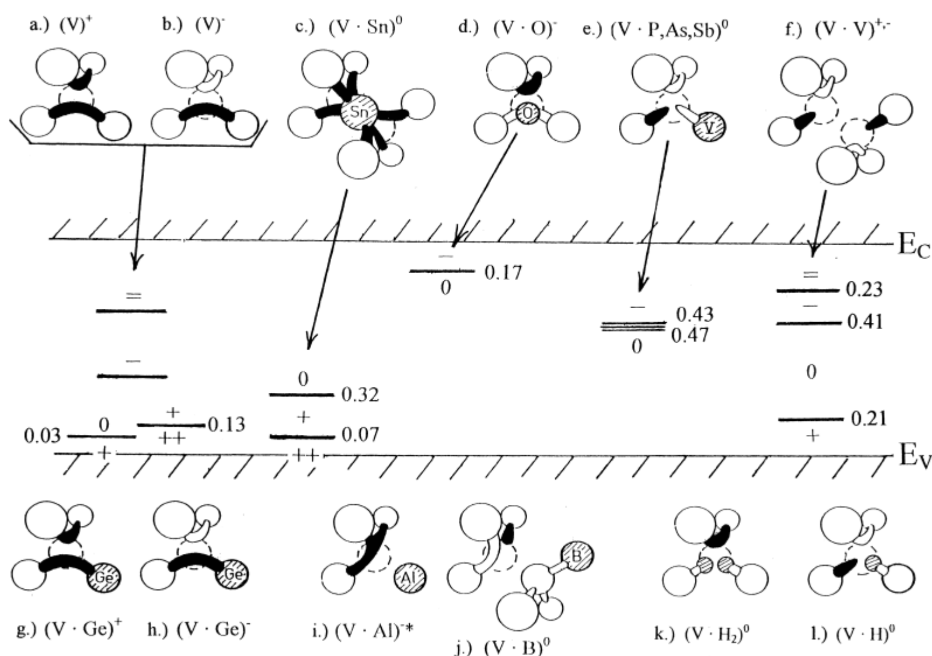

Figure 3.12: Diagram of several defect types and their mid-band gap energy levels in silicon (33).

Shallow traps for n-channel devices have energy levels close to the conduction band (and in p-channel devices close to the valance band), located inside the forbidden band gap region of silicon. A shallow trap requires only a small amount of thermal energy to introduce a majority carrier into the charge packet. Shallow defects can trap a majority carrier from the charge packet. Still, as the energy level is so close to the band edge, defects are predicted to release the charge almost instantaneously.

As discussed previously, there are five dominant n-channel trap species in CCDs. The A-centre is a defect where the silicon-vacancy neighbours an oxygen atom to form a stable trap. The E-centre, a

phosphorous dopant atom neighbouring a vacancy, is typically dominant for CCDs at room temperature and can be permanently filled when the temperature is maintained below approximately 273 K which will also mitigate any CTI effects (34). There is mixed evidence for the “unknown” trap, named as such because its source is not known. Figure 3.13 demonstrates these displacement damage effects on the lattice.

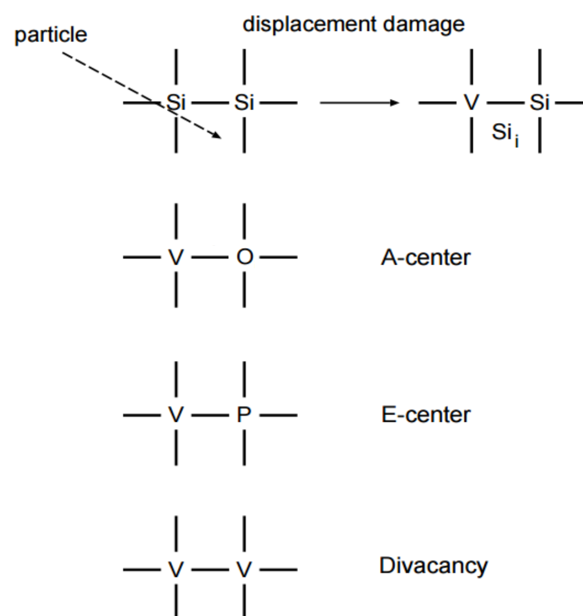

Figure 3.13: N-type silicon irradiation-induced defects (35).

There are three dominant charge trapping defect species in a p-channel device that dominate the increase in CTI under typical operation times and temperatures for astronomy applications: the silicon divacancy (V_2), carbon interstitial (C_i) and carbon-oxygen hole traps (36). Carbon is an unintended but inevitable component of CCD construction, being present in the stock silicon material and varying from batch to batch. Table 3.3 shows an estimation of the impurity levels in a standard CCD.

Table 3.3: Estimated impurities through the manufacturing process (37).

Impurity	Background Concentration (count per cm^3)	Notes
Boron	$\approx 10^{16}$	p-doped Silicon
Phosphorous	$\approx 10^{16}$	n-doped Silicon
Oxygen	$\approx 10^{18}$	Due to the crystal growth process
Carbon	$\approx 10^{15}$	Can vary from batch to batch and type of silicon used
Gold/Silver	Negligible	A single atom can cause hot pixel, needs to be avoided

The impurities introduced by the manufacturing process are either unavoidable due to the nature of the growth of silicon or are necessary for device operation (dopants). The capturing of a majority carrier is dependent on the type of defect and its associated emission time constant (release time) which changes with temperature, Figure 3.14. It is worth noting that all commercial CCDs are n-channel, but p-channel CCDs are still investigated because the technology may be inherently more radiation hard. This is theorised because the traps affecting CTI are different for the two device types.

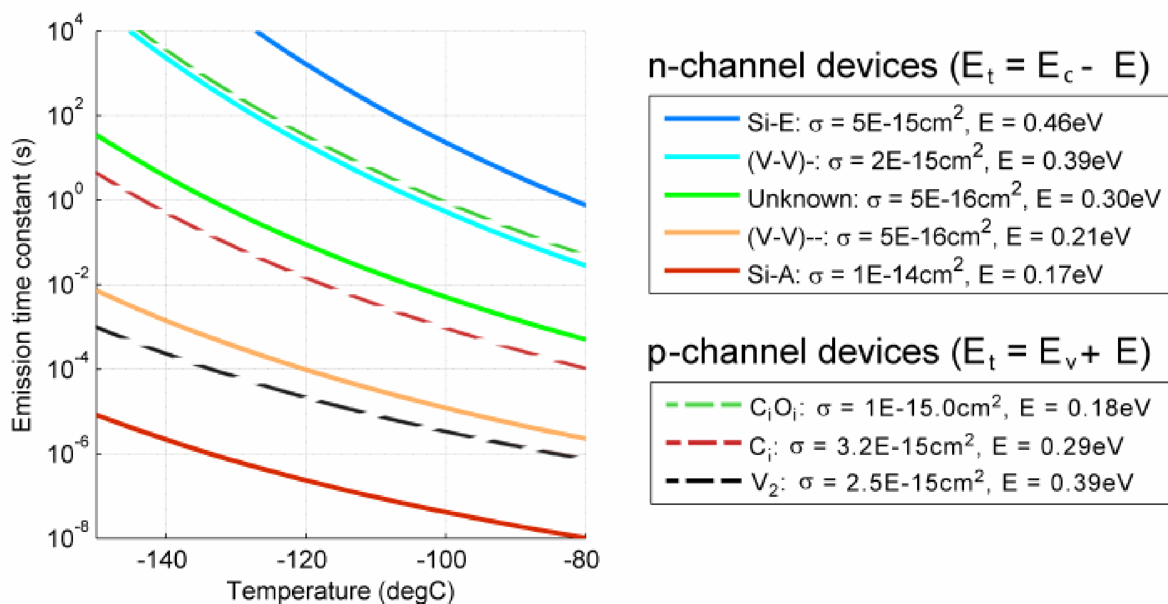

Figure 3.14: n-channel and p-channel comparison of dominant trap species following proton-irradiation. Extension of (38) to include p-channel dominant trap species.

3.4.4 The NIEL Scaling Hypothesis

Non-ionising energy loss (NIEL) is defined as the energy deposition in a material per unit mass by radiation through displacement of atoms, rather than excitation/ionisation. NIEL scaling is the act of comparing irradiations with a monoenergetic sources to find the equivalent damage from other monoenergetic sources. This is important as the broad and high energy spectrum of radiation in space cannot be fully simulated on Earth. This applies to both particle energy and species and a 1 MeV neutron damage equivalent normalisation for different irradiations is shown in Figure 3.15. The scientific standard for space based irradiations are normalised to either 10 MeV protons, 1 MeV neutrons or 1 MeV electrons.

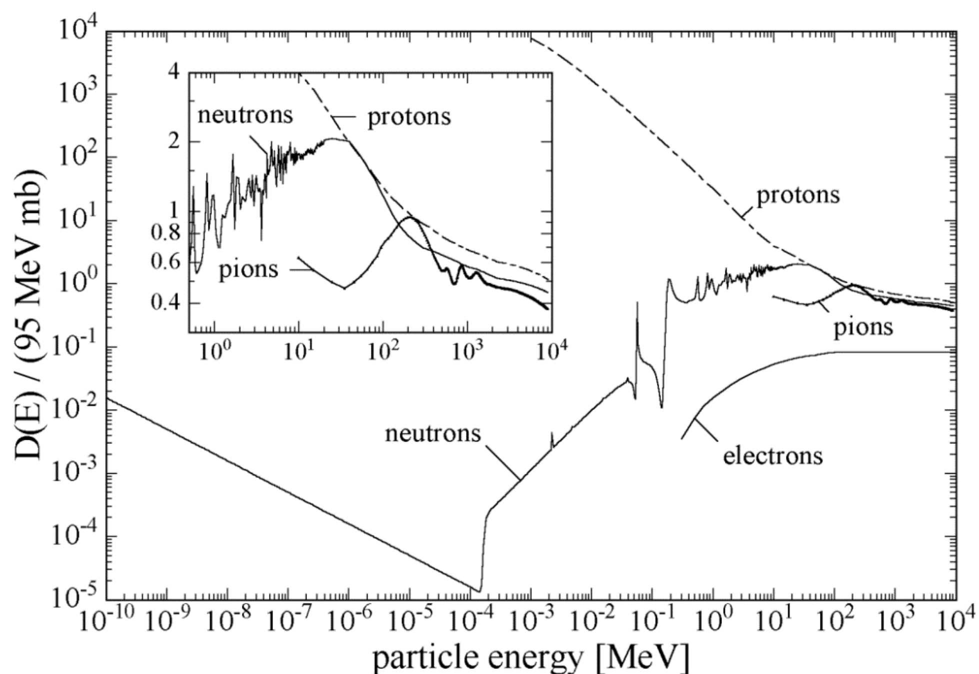

Figure 3.15: Displacement damage functions, where 95 MeV mb is the damage equivalent to 1 MeV neutrons. Image credit: (39) (Moll).

3.5 Radiation Damage in CCDs in Flight

To predict the radiation damage on Charge-Coupled Devices (CCDs), it is crucial that scientists understand how space missions interact with their radiation environment. Each mission studying the space radiation environment contributes to prediction models, such as SPENVIS which estimate the

flux density of different energetic particles for a chosen mission's orbit/flight path (41). Recreating the irradiation conditions of satellite orbits on Earth for pre-launch testing would require multiple radiation sources and beamlines at various energies and is next to impossible to achieve practically. Instead, devices are irradiated to a predicted end of life dose using a monoenergetic beamline or source. The only practical solution for experiments on Earth is for the beamline or source to be one particle type (i.e. proton, neutron, gamma, electron, heavy ion) which is scaled to the appropriate ionisation damage/NIEL scaling predicted in the spectrum from the space environment.

For example, Bassler (42) demonstrates the radiation dose predicted for the RØMER mission which orbits in high Earth orbit using SPENVIS, as shown in Table 3.4. The predicted electron spectrum would not apply to the high energy, electron-dense radiation environment of Jupiter but lower energy particles are blocked with a 20 mm aluminium shield. Electrons stopped in the shielding contribute to Bremsstrahlung, while protons dominate the ionisation damage.

Table 3.4: SPENVIS simulated radiation doses and 10 MeV fluence for a mission 2 year in HEO orbit, with a 20 mm aluminium shield as part of the RØMER mission (42).

Radiation type	Dose
Electrons	0.00 Gy
Bremsstrahlung	1.06 Gy
Trapped protons	13.01 Gy
Solar protons	1.52 Gy
Total ionising dose	15.59 Gy
Total non-ionizing fluence (10 MeV-equivalent)	4.97×10^9 protons/cm^2

Each space mission requires a new satellite design to accommodate different payloads to fit the criteria of the mission. The designing of a spacecraft is highly complex, and unforeseen problems can occur. For example, within the first month of operation of the Chandra X-ray Observatory it was discovered that the energy resolution of the front-illuminated CCD was rapidly degrading because of

weakly penetrating proton radiation. With each of Chandra's passes around the Earth (in a Highly Elliptical Orbit), the detector received a larger than expected device performance degradation. It was found that as Chandra passed through the SAA, 100-300 keV protons perfectly reflected off the telescope's X-ray mirrors into the focal plane of the CCD. When discovered, the Chandra and ACIS team were able to mitigate any further damage by operating the CCD in a different position for all further radiation belt passes.

In the presence of a solar flare or CME, the recommendation is to switch off the CCD to avoid imaging proton-produced false images and because biasing is known to speed up degradation for all forms of particle (43). Examples of these interactions are in data from the Stardust spacecraft, which in November 2000 interacted with a solar flare, saturating the images as high energy protons flooded in, forcing the spacecraft to operate in safe mode. A geomagnetic storm, also known as a solar storm, is a shockwave from the solar wind that interacts with the Earth's magnetic field and can impact the operation of the satellite.

3.5.1 Shielding

The CCD typically requires shielding on the satellite due to its sensitivity to radiation (which is described in more detail later in this chapter). High energy protons can be highly abundant in the space environment and contribute a large proportion of damage experienced by flight-missions to silicon-based detectors. Shielding aims to reduce the background radiation by slowing down or completely absorbing the incident particle. Low energy protons are considered "soft" protons up to several hundred keV (44), although the maximum energy is very loosely defined in the literature. The majority are produced through the solar wind and can easily be shielded against and fully absorbed in only a few centimetres of aluminium. While the majority of the solar wind and low energy particles are blocked by standard shielding and mirrors, degradation of the image sensor is still expected through a mission's lifetime. The density of damaging low energy particles that can penetrate shielding in space is very low.

A variety of shielding methods have been attempted during space missions that reduce, but fail to stop, all radiation sources from damaging the operating CCDs. Low energy protons can scatter from mirrors in the optical pathway and damage the detectors while high energy protons can penetrate even the most dense shielding practical on a satellite and cause damage to the CCD, with >100MeV protons from a CME event observed to the focal plane and charge trails indicating omnidirectional arrival (45). As complete mitigation from radiation damage is near impossible, so understanding the impact of radiation to spaceflight instrumentation becomes a priority. Different damage mitigation methods are being proposed with intense studies into high-Z material shielding and including adding a mechanical shield that physically retracts from the optical path of the sensor for observations which emphasises how critical radiation damage is to device operation.

3.6 Annealing

Annealing is the process of heat treatment to accelerate defect migration and dissociation. The process in CCDs can restore the device performance following irradiation, typically improving CTI and reducing the number of hot pixels. Various methods of annealing can be used, including thermal, current injection (electrical) and laser (optical) annealing (46). Of the annealing methods, thermal annealing is most common for defect analysis.

The properties fixed from annealing are produced from displacement damaging radiation, which introduces defects, interstitials and vacancies into the buried channel of the CCD. These defects found in the buried channel migrate over months or years while at room temperature and even longer at mission operating temperatures. The rate of change can be accelerated and even change the defect complex following heat treatment, demonstrated in Figure 3.16. Defects, interstitials and vacancies have a low potential energy necessary for lattice migration through the crystal (47). The migrating atom settles at the most energetically stable defect configuration. The rate of migration is dependent on both the thermal energy and the proximity to nearby defect constituents. The reader should refer

to (48) for a more in-depth analysis of the annealing properties and the DLTS method on trap identification.

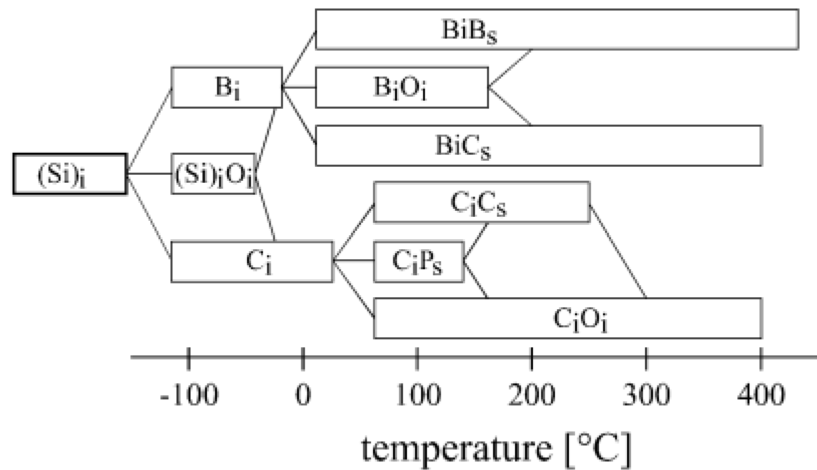

Figure 3.16: Reaction hierarchy of interstitial defect formation pathways for self-interstitial silicon. Image credit: (39).

CCDs in orbit usually run at very low temperatures which heavily suppresses dark signal. Each satellite mission CCD is scheduled to operate at a specific temperature. Temperature variations are chosen pre-flight to accommodate the science goals and suppress the dark signal, power requirements of the satellite, the amount of space dedicated to radiators and harsher tolerances on a colder focal plane. Large scale missions have a history of operating cold as seen in Gaia (163 K), Hubble (190 K) and Chandra (153 K), and future missions continue to cool the CCD arrays including Euclid's VIS instrument (153 K), SMILE (173 K) and PLATO (203 K).

The Wide Field Camera 3 (WFC3) CCD onboard the Hubble telescope performs monthly thermal anneals which take away 10% of the possible observing time to reduce the number of hot pixels (48). Hot pixels are the classification of pixels with an unusually high dark current and are believed form because of lattice defects or foreign atoms such as Fe, Ni, Au (49). The physics behind their magnitude increase in dark signal is still unknown, with some evidence that the electric field strength can influence the signal level and other evidence that the behaviour is similar to Random Telegraph Signal (RTS) pixels, presenting a signal of multiple discrete values randomly (50). While the performance has been improved for Hubble, other missions such as Chandra saw an unexpected increase in CTI. The

performance degradation was attributed to point defect interactions and demonstrates that the study of defects in space needs to be investigated thoroughly.

3.7 References

1. December 1968 - Orbiting Astronomical Observatory 2 (OAO-2) Launched [Internet]. NASA. 2016 [cited 16 August 2020]. Available from: https://www.nasa.gov/directorates/heo/scan/images/history/December1968_2.html
2. Janesick J, Elliott T, Collins S, Blouke M, Freeman J. Scientific Charge-Coupled Devices. Optical Engineering. 1987;26(8).
3. Rais-Rohani M. On structural design of a mobile lunar habitat with multi-layered environmental shielding. Rep. No. NASA CR-2005-213845, Marshall Space Flight Center, Ala. 2005 Apr.
4. Coronal Mass Ejections [Internet]. Swpc.noaa.gov. 2014 [cited 15 July 2020]. Available from: https://www.swpc.noaa.gov/phenomena/coronal-mass-ejections
5. Rigozo N, Nordemann D, Echer E, Echer M, Silva H. Prediction of solar minimum and maximum epochs on the basis of spectral characteristics for the next millennium. Planetary and Space Science. 2010;58(14-15):1971-1976.
6. Space Engineering Space Environment. [Internet]. ESA Spacewx.com. 2008 [cited 16 July 2020]. Available from: https://www.spacewx.com/Docs/ECSS-E-ST-10-04C_15Nov2008.pdf
7. Yamashita N, Hasebe N, Miyachi T, Kobayashi M, Okudaira O, Kobayashi S et al. Complexities of gamma-ray line intensities from the lunar surface. Earth, Planets and Space. 2008;60(4):313-319.
8. Piddington J. The closed model of the Earth's magnetosphere. Journal of Geophysical Research: Space Physics. 1979;84(A1):93-100.
9. Van Allen Probes Spot an Impenetrable Barrier in Space [Internet]. NASA. 2014 [cited 17 July 2020]. Available from: https://www.nasa.gov/content/goddard/van-allen-probes-spot-impenetrable-barrier-in-space

10. Space Engineering Space Environment. [Internet]. ESA Spacewx.com. 2008 [cited 16 July 2020]. Available from: https://www.spacewx.com/Docs/ECSS-E-ST-10-04C_15Nov2008.pdf
11. Fimmel RO, Van Allen JA, Burgess E. Pioneer: first to Jupiter, Saturn, and beyond. Scientific and Technical Information Office, National Aeronautics and Space Administration; 1980.
12. Bailey S, Landis G. The next-generation of space cells for diverse environments. InSpace Power 2002 May (Vol. 502, p. 9).
13. Stopping-Power & Range Tables for Electrons, Protons, and Helium Ions [Internet]. NIST. 2016 [cited 6 August 2020]. Available from: https://www.nist.gov/pml/stopping-power-range-tables-electrons-protons-and-helium-ions
14. Burt D, Endicott J, Jerram P, Pool P, Morris D, Hussain A, Ezra P. Improving radiation tolerance in e2v CCD sensors. InAstronomical and Space Optical Systems International Society for Optics and Photonics. 2009 Aug 26 (Vol. 7439, p. 743902).
15. Corbett J, Watkins G. Silicon Divacancy and its Direct Production by Electron Irradiation. Physical Review Letters. 1961;7(8):314-316.
16. Chen C, Corelli J. Infrared Spectroscopy of Divacancy-Associated Radiation-Induced Absorption Bands in Silicon. Physical Review B. 1972;5(4):1505-1517.
17. Kalma A, Corelli J. Photoconductivity Studies of Defects in Silicon: Divacancy-Associated Energy Levels. Physical Review. 1968;173(3):734-745.
18. Evwaraye A, Sun E. Electron-irradiation-induced divacancy in lightly doped silicon. Journal of Applied Physics. 1976;47(9):3776-3780.
19. Watkins G. Native Defects and their Interactions with Impurities in Silicon. MRS Proceedings. 1997;469.
20. Corbett J, Watkins G. Silicon Divacancy and its Direct Production by Electron Irradiation. Physical Review Letters. 1961;7(8):314-316.
21. Watkins G, Corbett J. Defects in Irradiated Silicon. I. Electron Spin Resonance of the Si-ACenter. Physical Review. 1961;121(4):1001-1014.

22. Watkins G, Corbett J. Defects in Irradiated Silicon. I. Electron Spin Resonance of the Si-ACenter. Physical Review. 1961;121(4):1001-1014.
23. Larsen A, Mesli A, Bonde Nielsen K, Nielsen H, Dobaczewski L, Adey J et al. ECenter in Silicon Has a Donor Level in the Band Gap. Physical Review Letters. 2006;97(10).
24. Bains S, Banbury P. A bistable defect in electron-irradiated boron-doped silicon. Journal of Physics C: Solid State Physics. 1985;18(5):L109-L116.
25. Kimerling LC, Asom MT, Benton JL, Drevinsky PJ, Caefer CE. Interstitial defect reactions in silicon. InMaterials Science Forum 1989 (Vol. 38, pp. 141-150). Trans Tech Publications Ltd.
26. Corbett J, Watkins G. Production of Divacancies and Vacancies by Electron Irradiation of Silicon. Physical Review. 1965;138(2A):A555-A560.
27. Bourgoin J, Ludeau P, Massarani B. Threshold energy determination in thick semiconductor samples. Revue de Physique Appliquée. 1976;11(2):279-284.
28. Holmström E, Kuronen A, Nordlund K. Threshold defect production in silicon determined by density functional theory molecular dynamics simulations. Physical Review B. 2008;78(4).
29. Loferski JJ, Rappaport P. Radiation damage in Ge and Si detected by carrier lifetime changes: damage thresholds. Physical Review. 1958 Jul 15;111(2):432.
30. Hemment PL, Stevens PR. Study of the Anisotropy of Radiation Damage Rates in n-Type Silicon. Journal of Applied Physics. 1969 Nov;40(12):4893-901.
31. Gossick B. Disordered Regions in Semiconductors Bombarded by Fast Neutrons. Journal of Applied Physics. 1959;30(8):1214-1218.
32. Srour J, Marshall C, Marshall P. Review of displacement damage effects in silicon devices. IEEE Transactions on Nuclear Science. 2003;50(3):653-670.
33. Wood S, Doyle N, Spitznagel J, Choyke W, More R, McGruer J et al. Simulation of Radiation Damage in Solids. IEEE Transactions on Nuclear Science. 1981;28(6):4107-4112.
34. Watkins G. Intrinsic defects in silicon. Materials Science in Semiconductor Processing. 2000;3(4):227-235.

35. Hopkinson G. Proton-induced CCD charge transfer degradation at low-operating temperatures. IEEE Transactions on Nuclear Science. 2001;48(6):1790-1795.
36. Stefanov K. Radiation damage effects in CCD sensors for tracking applications in high energy physics (Doctoral dissertation, PhD thesis, Saga University, Japan).
37. Mostek NJ, Bebek CJ, Karcher A, Kolbe WF, Roe NA, Thacker J. Charge trap identification for proton-irradiated p+ channel CCDs. InHigh Energy, Optical, and Infrared Detectors for Astronomy IV 2010 Jul 16 (Vol. 7742, p. 774216). International Society for Optics and Photonics.
38. Bush N. The impact of radiation damage on electron multiplying CCD technology for the WFIRST coronagraph. Open University (United Kingdom); 2018.
39. Hall D, Murray N, Holland A, Gow J, Clarke A, Burt D. Determination of In Situ Trap Properties in CCDs Using a “Single-Trap Pumping” Technique. IEEE Transactions on Nuclear Science. 2014;61(4):1826-1833.
40. Inguimbert C, Messenger S. Equivalent Displacement Damage Dose for On-Orbit Space Applications. IEEE Transactions on Nuclear Science. 2012;59(6):3117-3125.
41. SPENVIS - Space Environment, Effects, and Education System [Internet]. Spenvis.oma.be. 1996 [cited 19 July 2020]. Available from: https://www.spenvis.oma.be
42. Bassler N. Radiation damage in charge-coupled devices. Radiation and Environmental Biophysics. 2010;49(3):373-378.
43. Wang Z, Chen W, He B, Yao Z, Xiao Z, Sheng J et al. Dose rate effects on array CCDs exposed by Co-60 γ rays induce saturation output degradation and annealing tests. AIP Advances. 2015;5(10):107134.
44. Fioretti V, Bulgarelli A, Lotti S, Macculi C, Mineo T, Piro L, Bruno D, Cappi M, Dadina M. The Geant4 mass model of the ATHENA Silicon Pore Optics and its effect on soft proton scattering. InSpace Telescopes and Instrumentation 2018: Ultraviolet to Gamma Ray 2018 Jul 6 (Vol. 10699, p. 106993J). International Society for Optics and Photonics.

45. Hopkinson G, Mohammadzadeh A. Comparison of CCD damage due to 10- and 60-MeV protons. IEEE Transactions on Nuclear Science. 2003;50(6):1960-1967.
46. Larsen A, Mesli A, Bonde Nielsen K, Nielsen H, Dobaczewski L, Adey J et al. ECenter in Silicon Has a Donor Level in the Band Gap. Physical Review Letters. 2006;97(10).
47. Bourgoin J, Corbett J, Frisch H. Ionization enhanced diffusion. The Journal of Chemical Physics. 1973;59(8):4042-4046.
48. Marshall C, Marshall P. CCD radiation effects and test issues for satellite designers. NASA-GSFC Multi-Engineering Disciplinary Support Contract Task 1058m. 2003 Oct.
49. Widenhorn R, Dunlap J, Bodegom E. Exposure Time Dependence of Dark Current in CCD Imagers. IEEE Transactions on Electron Devices. 2010;57(3):581-587.
50. Hopkins I, Hopkinson G. Random telegraph signals from proton-irradiated CCDs. IEEE Transactions on Nuclear Science. 1993;40(6):1567-1574.

Chapter 4: The Trap Pumping Technique

4.1 Introduction

As discussed in Chapter 3 the space radiation environment is damaging to CCDs, with missions such as Euclid's VIS instrument requiring the development of damage correction models to achieve the science goals. CTI behaviour is directly linked to the defects in the buried channel which trap signal charge and reemit it into trailing pixels during readout. These defects can be characterised, and their properties measured using the "trap pumping" technique. In this chapter the history and methodology of the technique are described, summarising notable studies to demonstrate the evolution of the technique into a powerful research tool that can be run on flight hardware to assess the live radiation damage effects and place the work of this thesis into context.

4.1.1 A History of Pocket Pumping to Trap Pumping

"Pocket pumping" is a technique used for discovering and characterising electron (or hole) trapping sites in a CCD. These may include crystalline defects in the silicon and potential pockets which are imperfect potential well structures formed in the manufacturing process (1). In early uses of the technique the CCD was illuminated to a low level, recommended between 100-1000 electrons (2), and using a custom clocking scheme the charge packet is transferred across multiple rows or columns before returning to the original position to then be readout normally. The method caused charge build-up in regions that contain a potential pocket and this build-up increases in intensity with clocking repetitions. The initial scope of the technique was to find the size of the pocket and its position. An example of a frame using pocket pumping is shown in Figure 4.1.

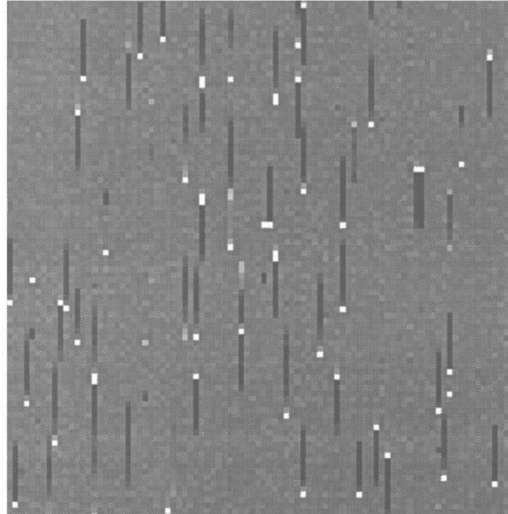

Figure 4.1: Pocket pumping frame across multiple pixels showing forward and reverse traps (2)

From 2010, pocket pumping emerges in the literature as one of the most effective tools to help to improve radiation tolerance and understand the defect landscape. Here is a summary of the previous work that laid the foundations towards "trap pumping" as a tool in the study of single pixel traps.

The first major paper using pocket pumping to look at radiation induced defects is from Mostek (3) who applied the technique to p-channel CCDs to understand the types of traps that affect CTI. The pocket pumping technique was expanded upon in this paper by clocking through a single pixel rather than multiple pixels, allowing for a more detailed analysis of the properties of individual traps. The CCD irradiation attempted to simulate the radiation environment for the proposed JDEM satellite in L2 orbit which was achieved by irradiating CCDs to multiple fluences with protons at an energy of 12.5 MeV. The front-illuminated CCDs were 250 µm thick with a 10.5 µm pixel pitch and a four-corner readout for the 3512 x 3512 pixel array. Pocket pumping was performed on the CCDs using a three-phase clock transfer process across a pixel boundary and back again with a clock timing of 100 kHz and repeated every 5 K between 128 K and 210 K. The density of traps was measured by pumping 10000 parallel transfers with a mean flat field level of approximately 8000 electrons rather than the 100 to 1000 previously suggested by Janesick which allowed for the measurement of defects with trap efficiencies below 1 e^-/transfer. Figure 4.2 shows a pumped image with traps creating "dipole" signals relative to the uniform image background.

The study showed that pocket pumping measurements could be used to identify traps in individual pixels, deduce the energy levels and cross sections of multiple trap species and with this information found the silicon divacancy was the dominant trap species for parallel transfer CTI at these clock speeds.

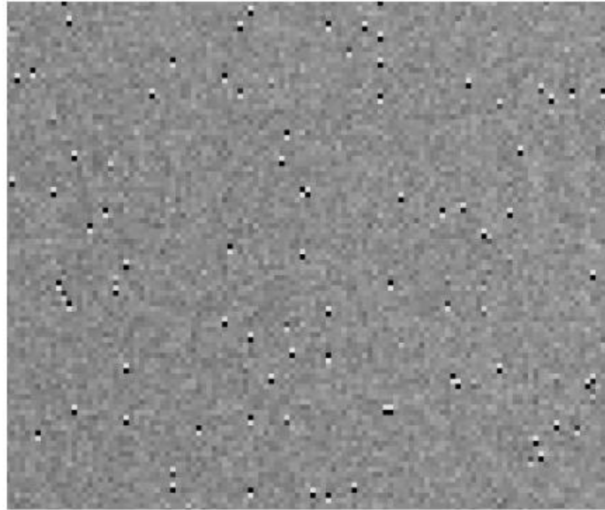

Figure 4.2: An example of a pocket pumping frame showing the characteristic "dipole" signal spike for individual pixel locations.

Expanding on the work of Mostek, Murray (4) uses pocket pumping (now called "trap pumping" to be more in line with the techniques primary objectives) to assist the Euclid VIS instrument to study traps to find any possible CTE improvements and any additional science. The paper highlights how trap pumping can increase the sensitivity of a camera through optimising the clocking process for the majority of traps in both parallel and serial directions. The variation of the transfer speed was found to directly impact the number of observations of different trap species, with the total trap density fluctuating with line time as different trap species became dominant to the CTI effects. Murray found that by changing the parallel clocking timings (t_{oi}) from 1 µs to 1000 µs the CTE of an irradiated device improved by a factor ≈1.6 and a clear connection was established between the number of traps observed by trap pumping and the measured CTE. It is finally recommended for the Euclid VIS instrument that there are sufficient resources to provide trap pumping data each day for each of the thirty-six detectors. Trap pumping daily is predicted to be beneficial to the study in three ways:

1) Instrument gain calibration is possible by measuring the intrinsic trap properties of the pre-flight unirradiated device and comparing to real time data.
2) Post processing data to mitigate CTI effects by predicting/correcting the position of deferred signal in the transfer process.
3) Radiation damage monitoring would be possible to better understand and model the radiation environment at the L2 orbit.

The effect of sweeping through multiple clocking timings was studied further in Hall (5), applying and expanding the use of Shockley-Read-Hall (SRH) equations to create a novel analytical method to accurately measure the emission time constant of individual traps directly in the time domain without any requirement to fit the energy or cross-section. The measurements of the emission time constants are consistent between simulations and experimental trap pumping results to within ≈5%. The paper demonstrated that trap pumping individual traps can be analysed in either the temperature, time or signal domains which allows for a very accurate measurement of trap properties. In addition, the emission time constants calculated in Figure 4.3(a) show that across the four temperatures sampled for an unirradiated device a real spread is observed (even when factoring in the most extreme measurement error). The histogram in Figure 4.3 (b and c) clearly defines two peaks rather than a sharp delta function at the location of the Si-A center which indicated that individual traps need to be characterised rather than an averaged measurement of all the traps in the imaging region.

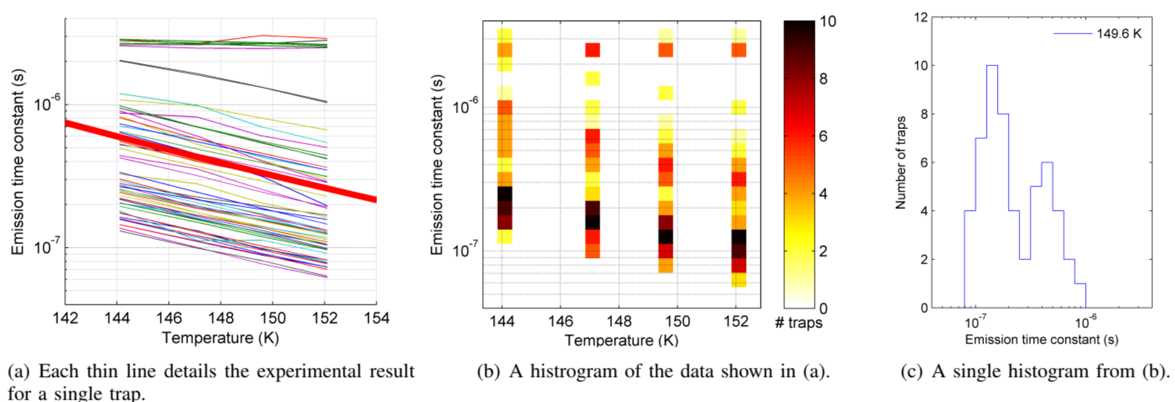

(a) Each thin line details the experimental result for a single trap.

(b) A histrogram of the data shown in (a).

(c) A single histogram from (b).

Figure 4.3: The emission time constants calculated from an unirradiated CCD273 in the serial register at four temperatures. (a) shows the emission time constant change with temperature for each individual trap and the red line shows the

theoretical time constant for the Si-A trap with an energy of 0.17 eV and a cross section of 10^{-14} cm^2. (b,c) Histogram of emission time constants with two clear peaks.

The thesis of Wood (6) applies the work done by Hall on additional irradiated devices with increased trap counts to provide a better statistical description of the trap landscapes. Irradiations were performed on p-channel devices at cryogenic temperatures and successfully measured and identified the emission time constants of the silicon divacancy and the carbon interstitial defect. Two p-channel CCDs were irradiated, one while cold and the other at room temperature. Comparing the emission time constant measurements between the two, the initial results of the cryogenic device indicate that when both devices were cooled to 153 K a factor ten reduction in the number of silicon divacancies was found over room temperature irradiations. When annealed at room temperature for approximately ten months the divacancy levels returned to a similar level found in the room temperature device. This implies that vacancies were frozen in and formed divacancies when warmed up. The conclusions demonstrate that previous studies on the trap landscapes at room temperature irradiations did not correlate directly to devices that are irradiated at cryogenic temperatures, directly affecting space-based detectors which generally suffer radiation damage at their operating temperature.

The thesis of Bush (7) expanded on the work under Hall, running a thorough investigation into the radiation damage, applying the trap pumping method to the EMCCD design proposed for the WFIRST mission. Trap pumping measurements were taken to find the initial annealing properties of the trap landscape following a proton irradiation at 165 K and found within the first 48 hours the number of observable traps and the dark signal decreased significantly indicating a rapid change of state for defects transitioning into their most energetically stable configuration or repair. In addition, detailed measurements of the most numerous trap species in a proton irradiated 2-phase EMCCD are summarised in Table 4.1. The study found a dramatic change in the divacancy and "unknown" emission time constants on the "trap diagram" (Figure 4.4) which is a useful tool for predicting the

emission time constant at different temperatures and choosing the appropriate readout speeds of a detector to reduce the impact of CTI. This most recent study by Bush (7) also found a peak for each trap with a large spread. However, all irradiations were conducted at ~6.5 MeV at the Synergy Health beamline at Harwell (UK). This spreading is not well understood. Several hypotheses have been put forwards which are further investigated in this study.

Table 4.1: Summary of the measurements on the energy level n-channel defects (below the conduction band), assumed cross sections and the temperature range necessary for the probing (7).

Trap species	Measured temperature range (K)	Energy level (eV)	Literature value cross section (cm^{-2})
Double acceptor silicon divacancy	158 to 183	0.226 ± 0.004	5 x 10^{-16}
"Unknown" trap	198 to 226	0.345 ± 0.003	5 x 10^{-16}
Phosphorus vacancy complex (Si-E)	238 to 248	0.45 ± 0.005	2 x 10^{-15}
Oxygen vacancy complex (Si-A)	152	0.16 ± 0.01	1 x 10^{-14}

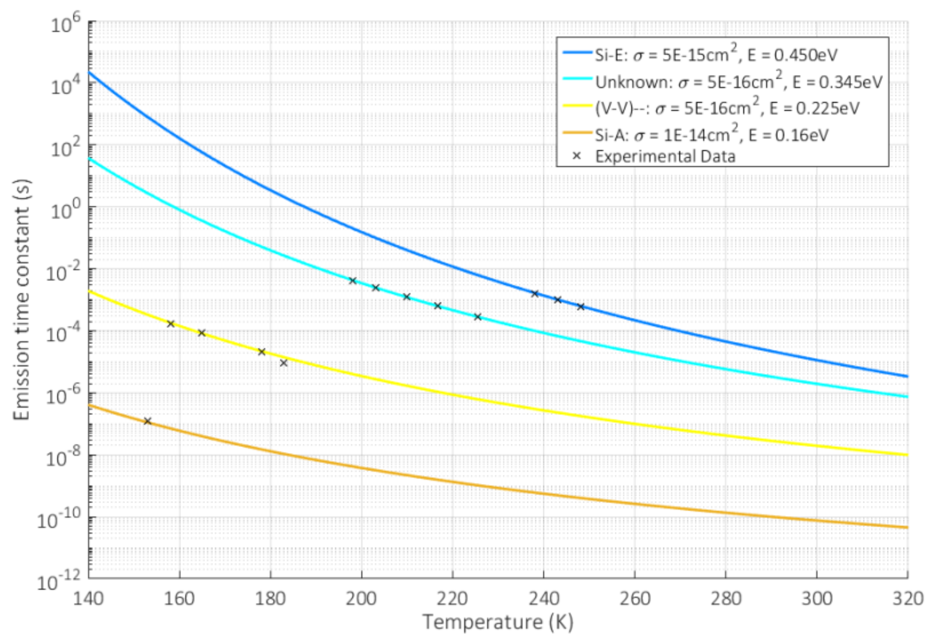

Figure 4.4: "Trap diagram" displaying the emission time constants of defects as a function of temperature based on the results of Bush (7). Image credit: (7).

4.1.2 The DLTS Technique

The analogous technique to trap pumping for semiconductors in more general terms is Deep Level Transient Spectroscopy (DLTS) technique, which allows for the measurement of activation energies and cross sections of deep level traps (8). Typical DLTS spectra are demonstrated in Figure 4.5 finding the trap resonances for five different stable defects, labelled E1 through to E5 and measured between 50 K and 250 K. The methodology is capable of finding the energy level of a trapping site; however, as the DLTS technique measures macroscopic trap properties, it fails to observe the distribution of all trap energy levels and cross sections. DLTS has a major deficiency, which is that its discrimination between defects with similar emission properties is such that the definitive identification of defects through their emission fingerprint is rarely possible. In addition, the linewidth of the DLTS peak hides the impact of the local environment on the defect such as strain effects or line defects. Trap pumping allows a similar measurement method to DLTS but applied to individual pixels which provides excellent statistics and sensitivity at observing single defects and their precise locations. The hypothesis that will be tested now is: how far do energy levels/cross sections extend beyond the primary peak location and are there any differences in the peaks due to particle type and energy of interactions?

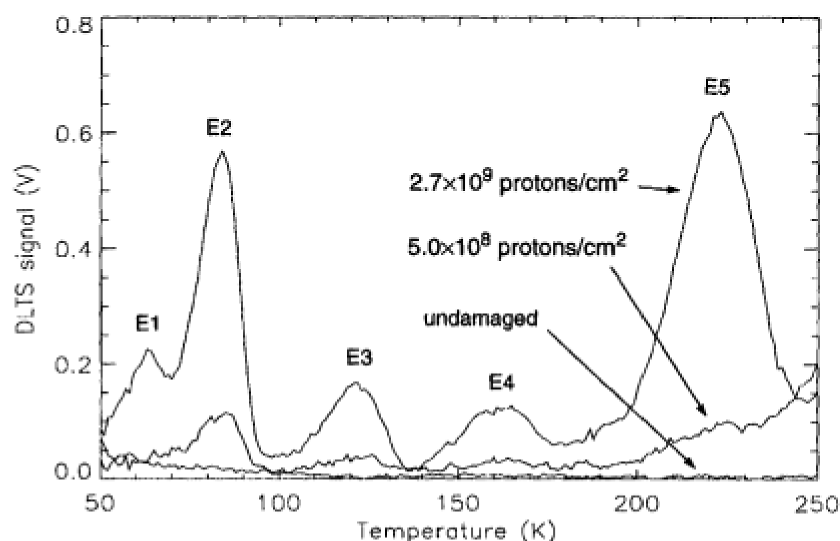

Figure 4.5: DLTS spectra at different proton doses at a fixed interval of 7.44 s (9).

4.1.3 Euclid VIS Instrument

Euclid's VIS instrument will be one of several upcoming missions such as SMILE and potentially Gaia (lab-based testing to back up in-orbit observations) to incorporate trap pumping following studies from the Open University, demonstrating the power of the technique for trap characterisation. The goal of trap pumping in flight will be to precisely characterise the trap landscape of the imaging regions and provide extra information to create the best possible CTI correction algorithms and adjust operating conditions if necessary.

In previous missions such as the Hubble Space Telescope (HST) it was found that CTI trails interfered with scientific observations and required specially designed software developed to correct CTI trailing damage up to 90% (10). Euclid will be using trap pumping on the VISible imager instrument (VIS) as part of the in-orbit calibration routines to mitigate radiation damage from the space environment by measuring the active trap landscape and identifying traps for each individual pixel. The ESA Euclid mission's VIS instrument aims to enable Weak Lensing measurements to determine the characteristics of dark energy and dark matter, which depend on accurate measurements of the shapes of distant galaxies. There is a strict CTI correction requirement, predicting a 99% correction on the CTI is necessary to successfully achieve the science goals (11,12).

It had previously been assumed that individual trap species have a fixed emission time constant when the temperature is fixed however measurements of energy levels and cross sections of trap species through techniques such as DLTS, EPR, Hall-effect measurements, photoconductivity, illumination-dependent IR absorption (to name a few) find a range of values rather than a definitive level, although it is not clear to what extent this spread is real or measurement induced. Furthermore, studies using trap pumping including (5-7) have found a distribution of emission time constants for all devices, irradiated at the Synergy Health Beamline at Harwell (UK) using the same beam energy. These studies, using the trap pumping technique show a distribution of time constants for each trap species, but more so clearly show this spread is *real* as the measurement accuracy is greatly increased. This

shows that studies of the trap properties of different trap species are necessary and leads to important questions such as if there is any impact of radiation damage properties such as fluence, energy levels and particle types on the trap landscape.

The trap pumping measurements taken so far have demonstrated that not only does the emission time constant of different trap species demonstrate a spread of emission time constants but a low level continuum of radiation induced traps are present throughout the trap landscape. The presence of these traps is significant as the correction method proposed for Euclid's VIS assumed a single species with no spread (13). It is worth noting the Euclid VIS CCD Working Group is currently aware of this trap spreading phenomena and have recently included the option of spread into their models based on the results of the aforementioned studies.

The experimental observations of the spreading of the emission time constants of different trap species has also brought to light that traps do not have delta function emission times and the spread is real and sizable to the point it extends through the entirety of the trap landscape, known as the "continuum of traps". The only studies on the trap pumping landscape using the trap pumping technique have irradiated at a single facility (Synergy Health, Harwell, UK) and with a proton energy of 6.5 MeV.

4.1.4 Understanding the Spread in Emission Time Constants

While field enhanced emission may be a likely candidate for the spreading of the emission time constants it has been hypothesised that local lattice strain may also play a crucial role in the spreading effect; it has previously been found in neutron irradiations to distort the energy level distribution and charge carrier capture behaviour of divacancy measurements as a result of the cluster of defects formed rather than point defects (14,15). As shown previously in Figure 3.11, the energy of the proton can determine what type of displacement damage effect can dominate the interactions and this is worthy of investigation with other damage types including solely point defect sources and clustering

radiation sources. As discussed in the introduction, this thesis therefore aims to answer several key questions on the spread on the emission time constants, including:

1) Does the particle type used to irradiate a device, and therefore the type of damage caused, influence the spread in parameters for a single trap species?
2) Is there any impact from irradiating particle energy on the trap landscapes produced?
3) Are the observed results facility dependant (i.e. is there an influence from secondaries that may be present from scatter in the beamline structure)?

4.2 Detailed Theory of Trap Pumping

The SRH model describes the generation and recombination of carriers and can be used to model the capture and emission of electrons/holes from electrically active defects in the CCD. The generation process describes a band change of an electron in either direction between the valance and conduction band through an intermediary jump, captured by a trap with an energy level held in the forbidden region of silicon. The recombination process describes an electron moving to a trap with an energy level in the forbidden region then returning to the original band (valance or conduction) shown in Figure 4.6.

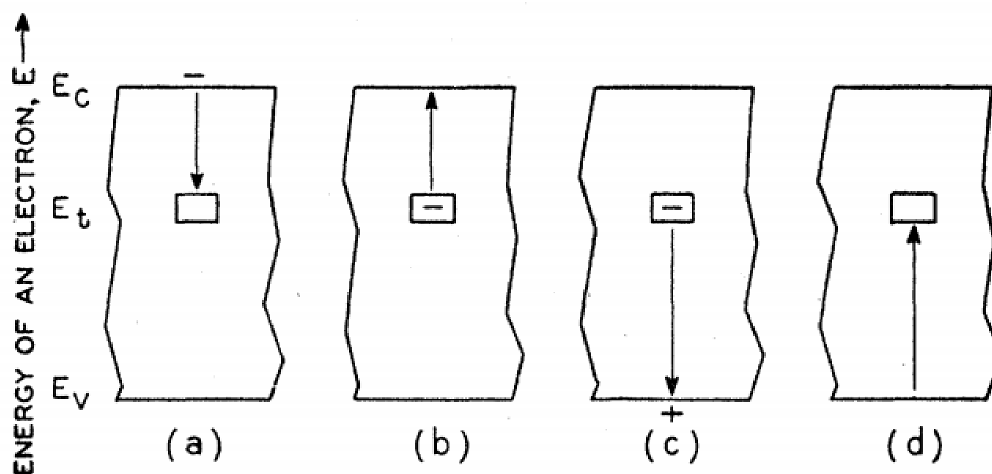

Figure 4.6: The basic processes involved in recombination by trapping: (a) electron capture, (b) electron emission, (c) hole capture, (d) hole emission (5).

The measuring of the capture and emission of electrons in CCDs is achieved through the manipulation of SRH Equations 4.1 to 4.4 while Equation 4.5 is a measure of the probability of either emission or capture (5,16,17).

$$\tau_c = \frac{1}{\sigma n v_{th}}$$ Equation 4.1

$$\tau_e = \frac{1}{X\chi\sigma N_c v_{th}} \exp\left(\frac{E}{kT}\right)$$ Equation 4.2

$$N_c = 2\left(\frac{2\pi m_{dos} kT}{h^2}\right)^{\frac{3}{2}}$$ Equation 4.3

$$v_{th} = \sqrt{\frac{3kT}{m_c}}$$ Equation 4.4

$$P_x = 1 - \exp\left(\frac{-\mathrm{t}}{\tau_x}\right)$$ Equation 4.5

The variable τ_c is the capture time constant and τ_e is the emission time constant of traps, σ is the capture cross-section, *X* is the entropy factor, χ is the field enhanced emission factor, m_{dos} and m_c are the density of states and conductivity effective masses of the electron respectively, n is the electron concentration and v_{th} is the thermal velocity. Adapting Equation 4.5 it is possible to add a term for the pumping probability (labelled P_p), Equation 4.6. Assuming a 100% probability of capture of the trap, the intensity of the dipole is given by $I = NP_p$, and as this is not consistent experimentally, Equation 4.7 determines the amplitude of the dipole *I*, *N* is the number of pumping cycles, P_c is the probability of pumping, $\tau_e$is the emission time constant of the trap dipole and t_{ph} is the time taken for a single pump in the pumping cycle, as demonstrated in Figure 4.7.

$$P_p = exp\left(\frac{-t_{ph}}{\tau_e}\right) - \exp\left(\frac{-2t_{ph}}{\tau_e}\right)$$ Equation 4.6

$$I = NP_c\left(exp\left(\frac{-t_{ph}}{\tau_e}\right) - \exp\left(\frac{-2t_{ph}}{\tau_e}\right)\right)$$ Equation 4.7

The measurement method for individual traps is detailed through Figure 4.7 with Figure 4.7(a) demonstrating the pumping signal intensity of the dipoles and how they are discernible from the

background noise. The Monte Carlo simulation of the derived SRH equation in Figure 4.7(b) shows the predicted intensity profile of a trap that pumps over a range of clocking phase times t_{ph} and produces something similar to a "resonance curve" for a trap with a peak amplitude of $\tau_e \ln 2$. This method makes it possible to scan the resonance of a trap in the time domain and measure the emission time constant of a trap. Figure 4.7(c) shows the change of the dipole intensity as t_{ph} increases. Figure 4.7(d) shows the significant variation in small temperature fluctuations and emphasises the temperature must be tightly controlled during trap pumping to extract accurate trap properties.

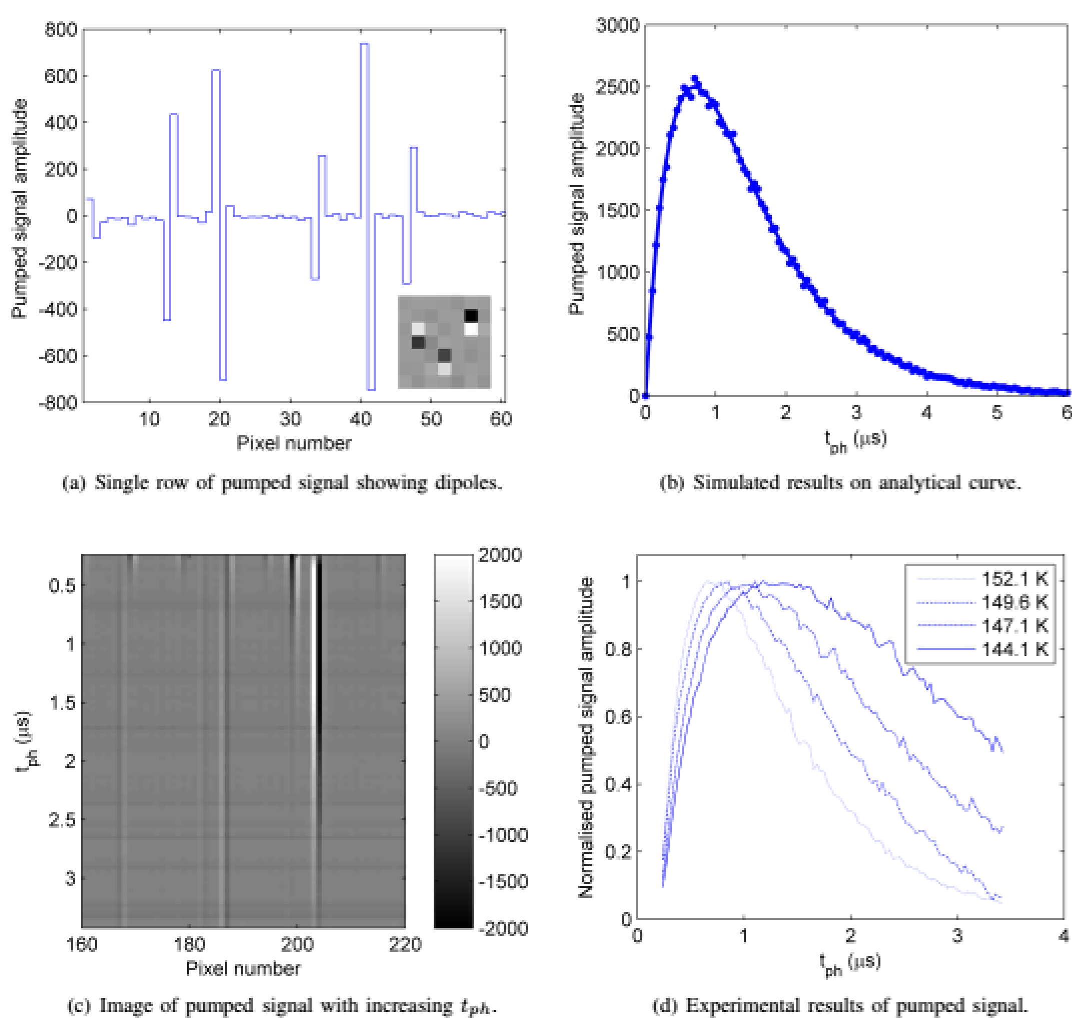

Figure 4.7: (a) is an example of a column from a mean-subtracted image where zero represents the average pixel value. The regions above and below the zero are dipole locations and having roughly equivalent equal and opposite amplitudes of neighbouring pixels suggests that a trap has captured signal from a pixel and reemitted into the neighbouring pixel. (b) shows the amplitude profile of a pixel containing a defect. Measuring the intensity readings of a dipole across a range of pumping times, we fit a curve to simulated data. (c) The pumping intensity of different pixels with emission time. (d) The measured curve with varying temperature. Image credit: (5).

The probability of capture for a trap in the central region of the charge cloud is modelled in Clarke (18) and at 10000 electrons (the charge cloud size used in this study). The reasonable assumption is made that the large signal density will result in near instantaneous charge capture. At small signals and at the outer edges of high-density charge clouds the probability of capture is significantly less.

To experimentally use trap pumping the charge packet is "shuffled" forwards and backwards over several electrodes, allowing signal charge to be captured by a trap and emitted into the neighbouring pixel. The repetition of this shuffling process increases the intensity difference between these neighbouring pixels and the mean and with a sufficient number of pumps (typically between 10^3-10^4) the intensity difference becomes large enough to distinguish the electrically active trap pixels from the flatfield background level. The resulting light-dark (or dark-light) pattern is known as a "dipole" and a row profile is shown in Figure 4.8 of the clear variation of the dipole intensity from the mean, showing dipoles at pixels 631-632 and 677-678, each showing the sub-pixel location of a single trap. The sub-pixel location of the trap can be deduced from the direction of the dipole (dark-light or light-dark) and clocking scheme used.

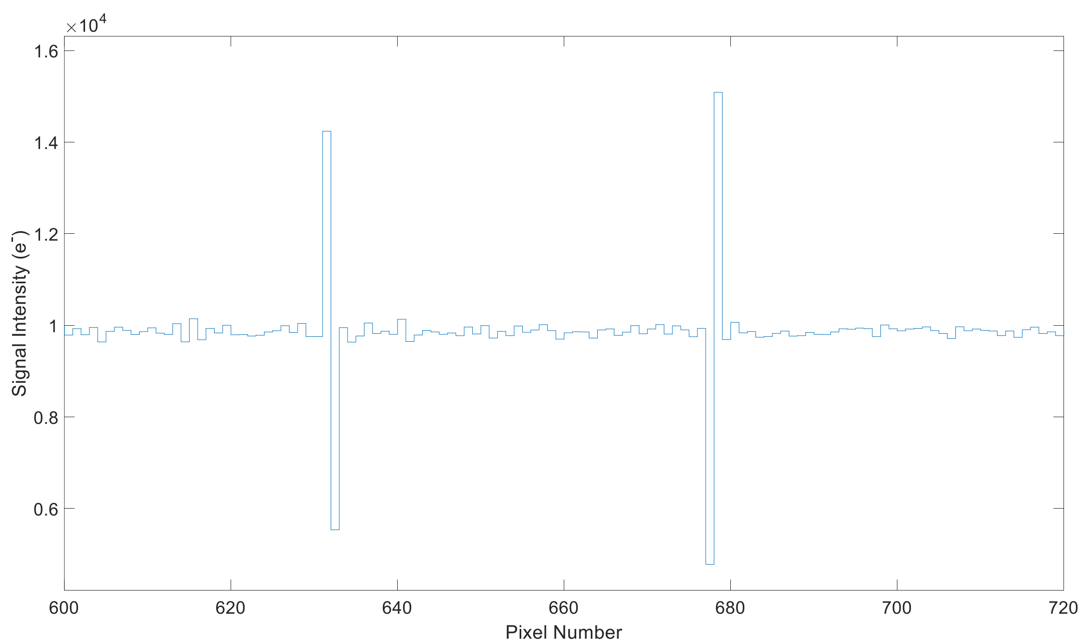

Figure 4.8: Intensity profile of a row of pixels for a trap pumped CCD347-20. A threshold of 3σ is chosen for dipole selection process and is dependent on neighbouring pixels both exceeding the threshold and opposite in sign when subtracting the mean value to zero the image.

Custom clocking schemes are designed to target the traps located under specific gates and multiple clocking schemes can be used to map all the electrically active traps across the entire pixel. In a three-phase device, each gate is labelled as ϕ1, ϕ2 and ϕ3 with the neighbouring pixels distinguished here by either ϕ1’ or ϕ1’’. Transferring the charge packets in the order ϕ1-ϕ2-ϕ3-ϕ2-ϕ1 (denoted henceforth as 12321) promotes emission of a captured trap to neighbouring pixels when the emission time constant is consistent with the window of emission as shown in Figure 4.9. If the emission time is too fast or slow the captured charge will return to the original pixels charge packet and not add to the dipole.

The pumping phase time t_{ph} defines the time the charge packet dwells under each phase of the detector. The dwell time must be sufficiently long to allow charge capture by the trap, while the pumping scheme must promote the transfer of charge into the neighbouring pixel and the charge packet must loop back to its original gate location multiple times to transfer a signal above the background level. To pump signal to the neighbouring pixel the pumping phase time would range between $t = t_{ph}$ and $2t_{ph}$ in example Figure 4.9. Custom sequencers can be writen to study traps under different electrodes so a trap under Φ2 is measurable with pumping scheme of 231’32. Four phase pumping is possible in schemes such as 1231’321 where the original charge packet moves into the neighbouring pixel and returns which probes different regions of the pixel. The typical range used for the pumping phase time ranges from 1 µs, the minimum dwell time achievable for efficient charge transfer, up to 10 ms, above which the technique hits very long emission times.

Sources of error in the technique include clock timings, inter phase emissions, electrode size non-uniformity, noise on the fit There is error on the dipole intensity due to traps at the edge of the charge packet not emitting/capturing as the probability of capture is low.

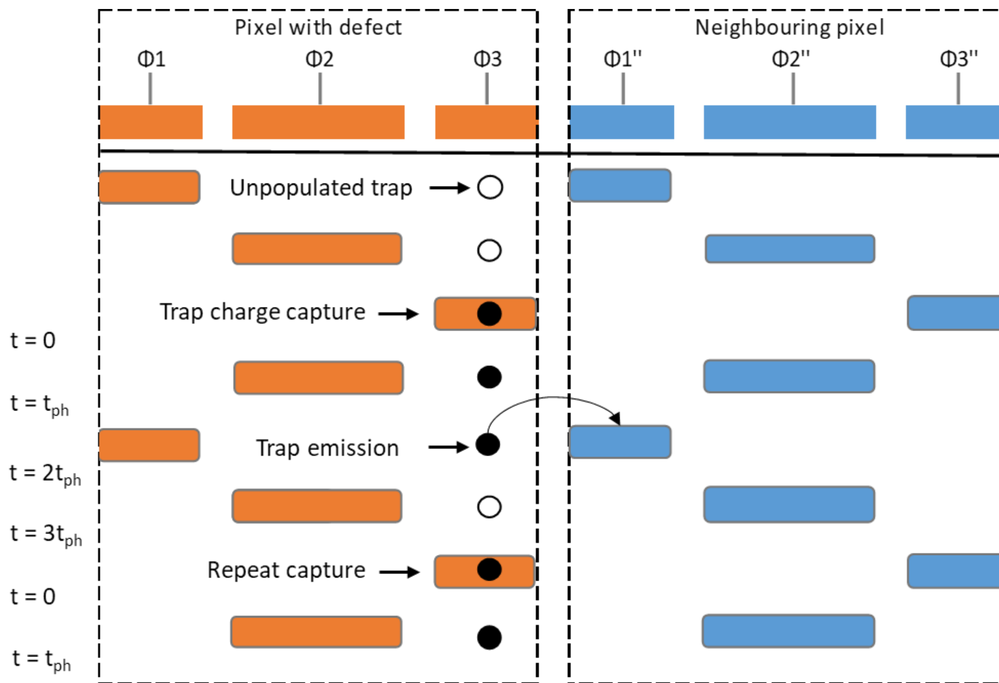

Figure 4.9: Clocking scheme for a three phase CCD with a trap located under Φ3. When the charge packet overlaps the location of the trap a signal charge is captured and if the emission time constant is within t_{ph} to $2t_{ph}$ the trap will emit the charge and the potential well will be strongest from Φ1'', taking charge from the original pixel and adding it to the neighbouring pixels charge packet.

To measure trap properties, we can then fit Equation 4.8 to the averaged dipole profile, Figure 4.10

$$I = NP_P = N(e^{-\tau_e t_1} - e^{-\tau_e t_2}) \qquad \text{Equation 4.8}$$

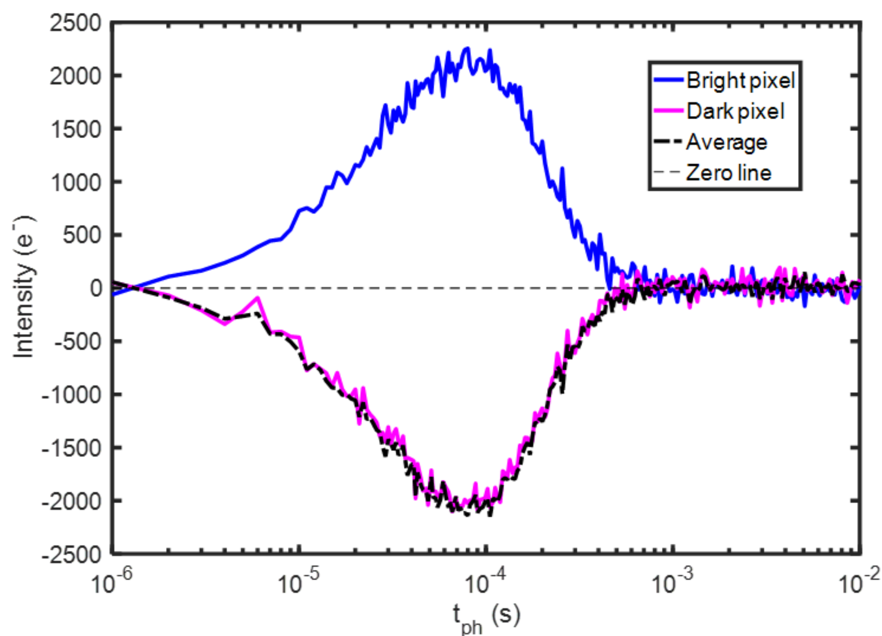

Figure 4.10: Dipole intensity of an electrically active trap. The bright and dark pixels intensities are shown and the average difference demonstrates the two pixels have pumped signal in equal and opposite quantity and sign, demonstrating successful trap pumping.

The experimental results (5-7) use devices that were all irradiated with protons at ≈6.5 MeV at the Synergy Health 5MV Tandem accelerator facility at Harwell (UK) and found unique distributions of emission time constants and energy levels which have yet to be fully explained. Discussion in upcoming results chapters aims to answer some of the unexplained questions including if there is any impact from proton beam energy, if consistency is found at different irradiation facilities (which may impact the production of secondaries within the beamline that may reach the detector) and if the distribution of emission time constants is unique to protons. Proton irradiated devices are to be compared with point defect forming damage sources (gamma irradiations) and clustering defect sources (neutron irradiations) to study the distribution of the energy levels.

The radiation damage effects are measured following irradiation campaigns on multiple CCDs of similar architectures irradiated using different particle types, energies, and doses and demonstrates variations in the trap landscapes and other properties of the devices.

4.3 References

1. Janesick J. Locating Electron Traps In A CCD [Internet]. Ntrs.nasa.gov. 1993 [cited 15 July 2020]. Available from: https://ntrs.nasa.gov/search.jsp?R=19930000546
2. Janesick J, Elliott T, Collins S, Blouke M, Freeman J. Scientific Charge-Coupled Devices. Optical Engineering. 1987;26(8).
3. Mostek NJ, Bebek CJ, Karcher A, Kolbe WF, Roe NA, Thacker J. Charge trap identification for proton-irradiated p+ channel CCDs. InHigh Energy, Optical, and Infrared Detectors for Astronomy IV 2010 Jul 16 (Vol. 7742, p. 774216). International Society for Optics and Photonics.
4. Murray NJ, Holland AD, Gow JP, Hall DJ, Tutt JH, Burt D, Endicott J. Mitigating radiation-induced charge transfer inefficiency in full-frame CCD applications by 'pumping' traps. InHigh

Energy, Optical, and Infrared Detectors for Astronomy V 2012 Sep 25 (Vol. 8453, p. 845317). International Society for Optics and Photonics.

5. Hall D, Murray N, Holland A, Gow J, Clarke A, Burt D. Determination of In Situ Trap Properties in CCDs Using a “Single-Trap Pumping” Technique. IEEE Transactions on Nuclear Science. 2014;61(4):1826-1833.
6. Wood D. Radiation-induced Deep-level Defects in CCD Imaging and Spectroscopy Sensors. Open University (United Kingdom); 2018.
7. Bush N. The impact of radiation damage on electron multiplying CCD technology for the WFIRST coronagraph. Open University (United Kingdom); 2018.
8. Lang D. Deep-level transient spectroscopy: A new method to characterize traps in semiconductors. Journal of Applied Physics. 1974;45(7):3023-3032.
9. Hardy TD, Deen MJ, Murowinski R. Effects of radiation damage on scientific charge coupled devices. InAdvances in imaging and electron physics 1999 Jan 1 (Vol. 106, pp. 1-96). Elsevier.
10. Massey R, Stoughton C, Leauthaud A, Rhodes J, Koekemoer A, Ellis R et al. Pixel-based correction for Charge Transfer Inefficiency in theHubble Space TelescopeAdvanced Camera for Surveys. Monthly Notices of the Royal Astronomical Society. 2010;401(1):371-384.
11. Massey R, Hoekstra H, Kitching T, Rhodes J, Cropper M, Amiaux J et al. Origins of weak lensing systematics, and requirements on future instrumentation (or knowledge of instrumentation). Monthly Notices of the Royal Astronomical Society. 2012;429(1):661-678.
12. Cropper M, Hoekstra H, Kitching T, Massey R, Amiaux J, Miller L et al. Defining a weak lensing experiment in space. Monthly Notices of the Royal Astronomical Society. 2013;431(4):3103-3126.
13. Paykari P, Kitching T, Hoekstra H, Azzollini R, Cardone VF, Cropper M, Duncan CA, Kannawadi A, Miller L, Aussel H, Conti IF. Euclid preparation-VI. Verifying the performance of cosmic shear experiments. Astronomy & Astrophysics. 2020 Mar 1;635:A139.

14. Svensson B, Mohadjeri B, Hallén A, Svensson J, Corbett J. Divacancy acceptor levels in ion-irradiated silicon. Physical Review B. 1991;43(3):2292-2298.
15. Kuhnke M. Microscopic investigations on various silicon materials irradiated with different particles with the DLTS method. Deutsches Elektronen-Synchrotron (DESY); 2001.
16. Shockley W, Read W. Statistics of the Recombinations of Holes and Electrons. Physical Review. 1952;87(5):835-842.
17. Shockley W, Read W. Statistics of the Recombinations of Holes and Electrons. Physical Review. 1952;87(5):835-842.
18. Clarke A, Hall D, Holland A, Burt D. Modelling charge storage in Euclid CCD structures. Journal of Instrumentation. 2012;7(01):C01058-C01058.

Chapter 5: Proton Radiation Damage

5.1 Introduction

The previous chapter highlights the history of the trap pumping technique and its practical applications. The following chapters demonstrate the experimental work completed for this thesis by applying the trap pumping technique to several devices irradiated with different radiation types (protons, high energy photons and neutrons) and at different energies, which are summarised in Table 5.1 for ease of reference. Additional features including the device type, the dosage, biasing conditions, and the shorthand names each device are found in this table. This chapter summarises the experimental trap pumping results of two Teledyne-e2v CCD47-20s, which were irradiated with protons at 6.5 MeV and 72.8 MeV to find variations in the trap properties of the double-acceptor silicon divacancy.

Irradiations carried out in the CEI for Euclid VIS instrument several years ago showed through the trap pumping technique that there was a distribution of properties across what was believed to be the same trap species. This distribution of emission time constant required a rethink of how CTI effects would be corrected, particularly regarding the "continuum" outside of the key trap species. However, these results were only obtained at one energy (≈6.5 MeV) and at one facility which may impact how "clean" the beam of protons is in terms of energy range and if any secondaries are produced. To provide confidence in both the "spread" of the key trap distributions and the continuum, the measurements are repeated at 6.5 MeV at the same facility used previously before carrying out a new test at 72.8 MeV, still using protons, at a different facility. Table 5.1 summarises all the irradiations taken during this study, highlights which devices are being discussed in the upcoming chapter and includes the irradiation conditions. Multiple trap pumping runs were completed for irradiated devices over the space of several months to years.

Table 5.1: Summary of the irradiation conditions of devices in this study. Devices discussed in the chapter are highlighted. All irradiations were performed at room temperature and all devices were stored at room temperature. All proton irradiated devices and the electron irradiated device E1 were irradiated under vacuum.

Device type	Interacting particle type	Energy	Facility	Dose	Biasing during irradiation	Shorthand name	Irradiation under vacuum	Irradiation date
CCD47-20	Proton	6.5 MeV	STERIS	3.37×10^9 protons/cm^2	Unbiased	P6.5 #1 & #3	Yes	09/09/2017
		6.5 MeV		6.74×10^9 protons/cm^2		P6.5 #2		09/09/2017
		72.8 MeV	Paul Scherrer Institut (PSI)	2.53×10^{10} protons/cm^2		P72.8		14/05/2016
		200 MeV		5.16×10^{10} protons/cm^2		P200		14/05/2016
	Electron	1 MeV	ONERA GEODUR	10 krad		E1		21/07/2016
CCD347-20	Unirradiated	-		-	-	C0	-	
	Photon	Cobalt-60 source	ESTEC - ESA	50 krad	Clocked	G50	No	21/06/2017
				100 krad	Clocked	G100C		
				100 krad	Clocked & long int	G100CI		
				200 krad	Clocked	G200C		
				200 krad	Clocked & long int	G200CI		
	Neutron	Californium source 2.15 MeV	ISIS	5.00×10^9 neutrons/cm^2	Unbiased	N2.15		07/04/2018

5.1.1 CCD47-20 Devices

The CCD47-20 is a popular imaging sensor from Teledyne-e2v with a rich flight history, being successfully used by multiple space agencies in over 40 high profile space missions including Sapphire, CHEOPS and Cassini-Huygens (1). The most common applications of the device include spectroscopy, scientific imaging, star tracking and medical imaging.

The proton irradiation comparison study presented here compares multiple Teledyne-e2v CCD47-20 with the schematic shown in Figure 5.1. The CCD47-20s used are back-illuminated, with a pixel size of 13 µm x 13 µm and a pixel resolution of 1024 x 1024 pixels. The maximum readout frequency is 5 MHz, and the unirradiated readout noise is approximately 2.0 e^- RMS. The design allows for high QE measurements of ultraviolet (193-400 nm), visible (400-700 nm) and near-infrared (700-1000 nm) wavelengths. Both devices used here are grade 5, meaning they are fully functional CCDs but they have an image quality worse than the desired specification for sale to external customers. These devices suffer from a number of pixels containing blemishes which can include excess traps, black spots with a signal level of less than 80% of the local mean, and white spots (similar to hot pixels) with a dark signal 25 times the specified maximum dark signal generation rate. Initial operating voltages were chosen based on recommended settings from the Teledyne-e2v datasheet.

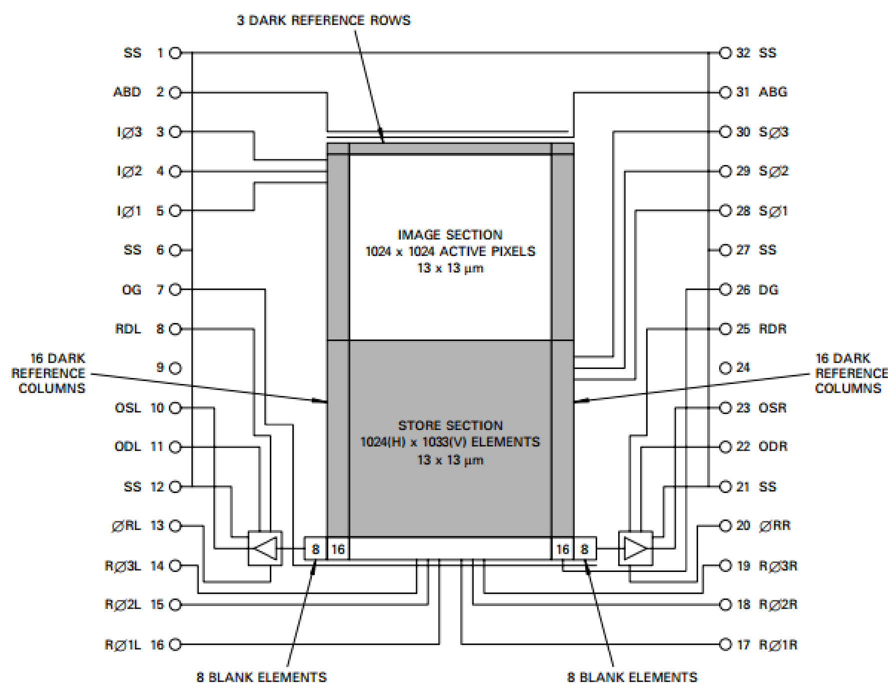

Figure 5.1: Schematic of CCD47-20, showing the photosensitive image region and store region with 2 mm aluminium shield and pin outputs.

5.1.2 Irradiation Facility

Two facilities were used for the proton irradiations, the STERIS Synergy Health ion beam site (Harwell, UK) and the Paul Scherrer Institute (PSI, Switzerland). Both beam lines were chosen according to the beam size, flux and quoted uniformity. The STERIS ion beam facility at the Harwell research complex in Didcot, UK is equipped with a 5 MV Tandem accelerator capable of accelerating protons and other light ions up to 10 MeV and was the facility used for the aforementioned Euclid VIS studies.

The P6.5 irradiations were part of the P-channel irradiation campaign which provided the most detailed investigation to date into the trap landscape of defects that form and stabilise while cold. Three n-channel CCD47-20 devices, P6.5 #1, #2 and #3 were irradiated as part of the aforementioned P-channel study for both dosimetry calculations and for trap pumping research of energetic proton interactions. As the study is looking at the effects of displacement damage, the fluence was chosen to scale to the industry standard 10 MeV equivalent proton dose. The devices were irradiated at room temperature, under vacuum and unbiased as shown in Figure 5.2 with glass taken off.

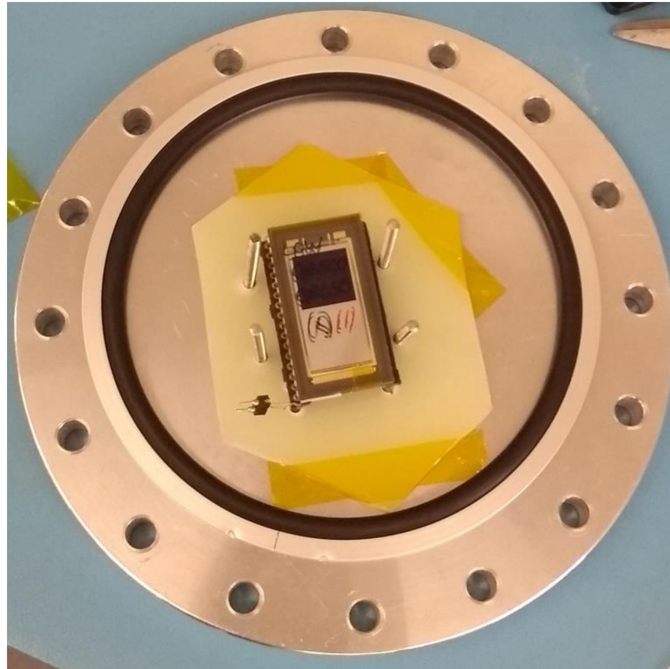

Figure 5.2: CCD47-20 mounted onto beamline flange prior to irradiation.

The ONERA-CEI study was originally conducted by Phillipa Smith under which two CCD47-20s were irradiated at PSI with proton energies of 72.8 MeV and 200 MeV. The 200 MeV device was too heavily damaged from the high energy, high fluence proton irradiation to successfully complete trap pumping. The fluence was chosen such that the total ionising doses across all devices were equivalent. These devices were irradiated unbiased, in air and with the pins shorted.

5.2 Trap Pumping Experimental Setup

Trap pumping requires a stable temperature to study the trap properties of CCDs accurately. A thermoelectric cooler (TEC) setup was used for characterisation tests and trap pumping the "Unknown" defect (section 0) but the setup was found to be limited to an unstable minimum temperature of 248 K. The temperature limit meant the dark signal generation rate was significant and for the longer pumping phase times greatly shifted the flat field intensity and temperature instability results in uncorrectable data. A new chamber was built in this study to incorporate a Stirling cooler as the primary cooling source which is capable of a stable base temperature of ≈145 K with a

biased CCD tuneable within the temperature range necessary to probe the double acceptor silicon divacancy (145 K to 175 K) which is the dominant trap species causing degradation in parallel CTE under standard operating conditions for space applications. The complete experimental setup is shown in Figure 5.3 with additional internal illustrations of the internal setup of the CCD housing chamber in Figure 5.4. The temperature was monitored and controlled using a Lakeshore Cryotronics 325 temperature controller operated using custom MATLAB scripts developed for this testing.

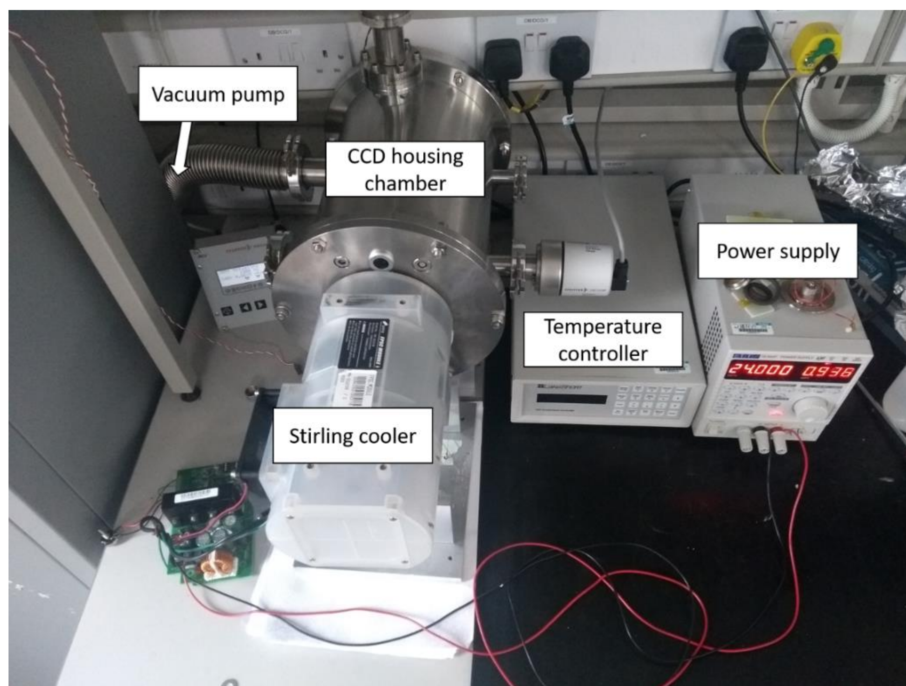

Figure 5.3: Experimental setup for trap pumping. The CCD is stored in the housing chamber which is brought to a pressure of 10^{-4} mbar necessary to prevent the formation of ice. The Stirling cooler reduces the temperature of the CCD to a stable base level. The temperature controller both monitors the CCD temperature from the PT-1000 and heats the cold finger by controlling the output of the 25 W heater. CCD drive electronics are located on the shelf above the chamber.

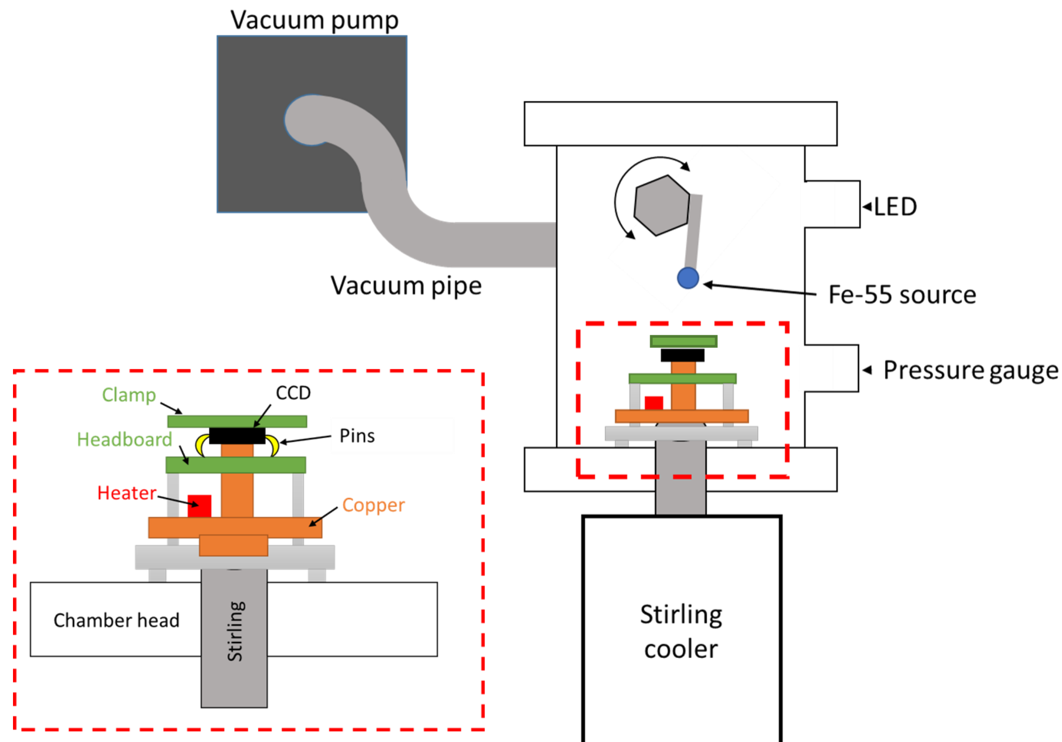

Figure 5.4: Stirling cooler experimental setup (not to scale). The clamp contains a square central cut-out for CCD illumination. The Fe-55 source is mounted on a rotating arm that is manually adjusted for X-ray calibration. The red dotted region is the detachable flange where the CCD is mounted to.

5.2.1 Experimental Method

Two proton irradiated devices were considered to compare the impact of proton energy on the trap landscapes whilst also confirming that any nuances in the distribution were not facility-specific. Using the experimental setup shown previously in Figure 5.4, the trap pumping process begins by clamping a single CCD onto the headboard and the whole flange is sealed on the end of the vacuum chamber. To confirm the device is correctly operating, a test image is taken where the voltages and clocking sequencers are individually designed for each CCD architecture. The voltages are chosen based on the specific CCD datasheets which recommend the operating conditions. For the clocking sequence test, a short integration is performed with a ^{55}Fe source and the image is read out, where the image, store and overscan regions are checked to confirm that the different areas of the detector are clearly defined. When the device has demonstrated full function the vacuum pump is started and observed until the pressure stabilises at 5 x 10^{-5} mbar. A low-pressure vacuum is necessary to stop condensation and ice accumulating on the detector when cooling. The Stirling cooler then applies a fixed cooling

load that can be set to slowly ramp the temperature down to a stable level to not exceed the cooling rate recommended by the device manufacturer. The Lakeshore temperature controller adjusts the power supplied to a 25 W heater mounted on the copper cold finger which is accurate to ± 0.1 K.

The gain is calculated using the ^{55}Fe source in the chamber. The X-ray source emits radiation at three energies with the most intense emission from the Mn-Kα line with known energy of 5.899 KeV which in silicon through the photoelectric effect measures approximately 1620 electrons per event. The mode of the secondary peak of an X-ray calibration frame is used to calibrate the voltage conversion from digital number (DN) to electrons. A flat field is produced by varying the LED flash time such that a mean of 10000 electrons is measured. If the device is heavily damaged through radiation damage effects and the flat field result is unreliable then a fixed LED pulse time is used, which is found by calibrating an unirradiated device with the same method.

The technique is not particularly effective for low illumination levels where the probability of capture is lessened. Trap pumping is typically measured at 4000-10000 e^- so the charge cloud electron density is large enough for defects to capture efficiently.

5.2.2 Clocking Sequence

The sequencer is responsible for integration, trap pumping the image area and then reading out the entire detector by raising and lowering the clock voltages at precise times. The XCAM electronics box controls the clock timings, which are checked every six months with an oscilloscope to confirm there are no discrepancies over time. For the three-phase CCD47-20 pixel design, each gate in the pixel of Figure 5.5 is labelled as ϕ1, ϕ2 and ϕ3 with the neighbouring pixels distinguished as either ϕ1' or ϕ1''. The trap pumping sequencer process used for both CCD47-20 devices is illustrated in Figure 5.5 where the black dots represent traps under the phases, and the vertical blue lines between ϕ1 and ϕ2 are the potential barriers from the AIMO implant that stop back-clocking between the two phases.

The specific clocking sequence used in trap pumping CCD47-20s is restricted because of the AIMO implants found in-between the first and second phase, prohibiting back clocking. To successfully trap

pump a device in AIMO configuration only one pumping scheme is theoretically possible for a three-phase device and this is demonstrated to work in the upcoming trap pumping results. The trap pumping loop transfers the charge packet from under ϕ2 to ϕ3 and from ϕ3 to ϕ1 in the neighbouring pixel (denoted as ϕ1'). The sequence is then run in reverse returning the charge packet to its original phase under ϕ2. This sequence more easily described by the shorthand (231'32) which is the ordering of the phases that are turned on to complete one pump. Though not described in the pumping sequence, each transfer stage has an intermediary step to guarantee efficient transfer where for example moving from ϕ2 to ϕ3 both voltages are raised before ϕ2 is lowered and ϕ3 remains high. The inability to use other pumping schemes with the AIMO implant limits the physical area under the gates that other traps can be probed but the method still provides sufficient statistics for an effective comparison. The pumping sequence is repeated 10,000 times to distinguish a trap peak from the background noise.

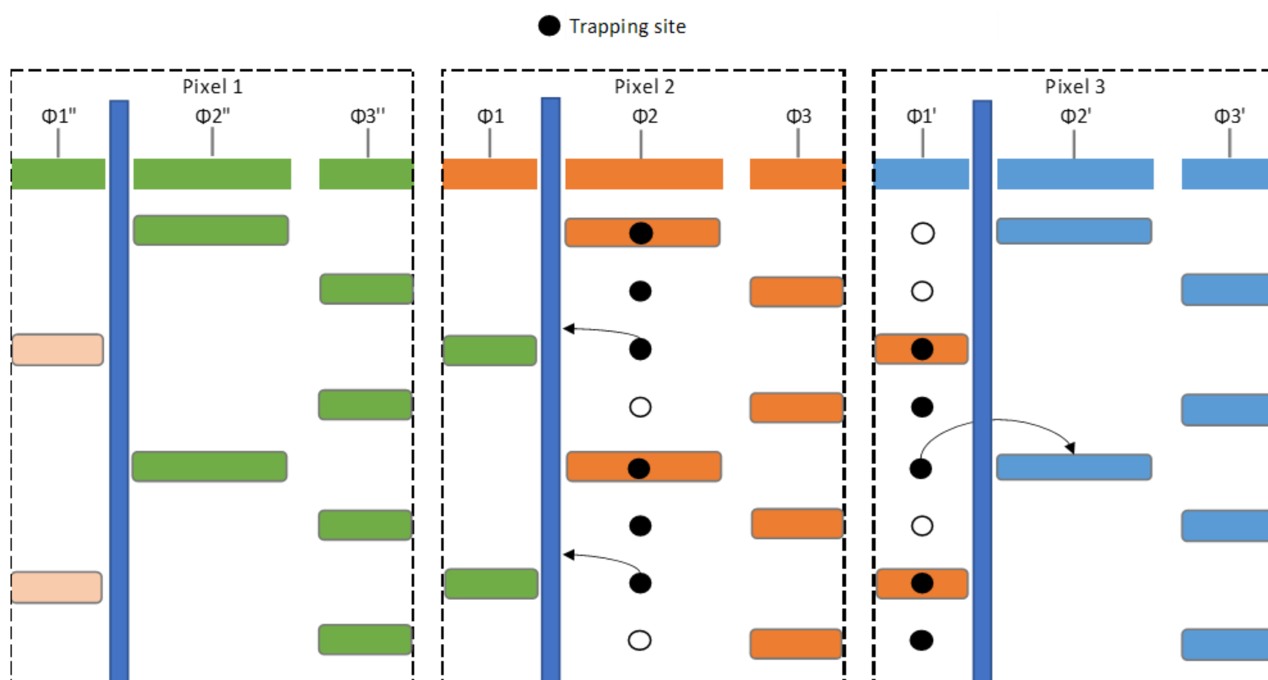

Figure 5.5: The trap pumping scheme (231'32) that cyclically shuffles the charge cloud for a CCD47-20. The AIMO implant shown as the vertical blue bar which stops backclocking. The black dots represent the traps that capture the signal from the charge cloud and the arrows show trap reemission is only possible in a single direction because of the implant.

5.2.3 Trap Measurements

To successfully measure trap properties, the trap pumping sequencer must be repeated several times while varying the time that a charge packet is held under an electrode before transfer (known as the "phase time"). For this study, 219 trap pumping frames are taken at each temperature where each frame has a different phase time, logarithmically spaced between 10^{-6} and 10^{-2} seconds. When the phase time approaches the emission time constant of a trap (which changes with temperature) the trap has a larger probability of reemission to the neighbouring pixel, which increases the signal difference between the two pixels. A search is made through the 219 frames for neighbouring pixels that both have an intensity exceeding 3σ above the background and are opposite in sign. An intensity profile is created for each pixel location across the phase times for the neighbouring pixel pairs, also known as a dipole. Figure 5.6 illustrates a dipole in a background subtracted frame with a single-phase time while Figure 5.7 shows the intensity plot of a single dipole across multiple phase times for both dipole pixels.

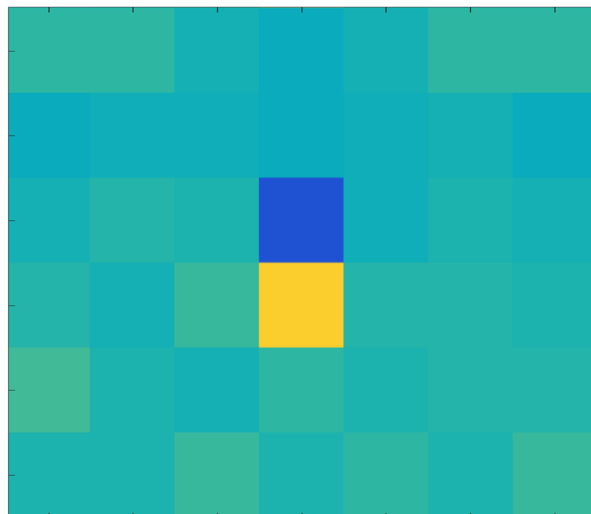

Figure 5.6: Visualised data of a dipole measured from a frame, identified by the low intensity pixel (blue) and high intensity pixel (yellow), taken at a phase time of 100 μs. This configuration is classed as "dark-light" and demonstrates signal has been captured by a trap in the dark pixel that has been reemitted to the bright pixel.

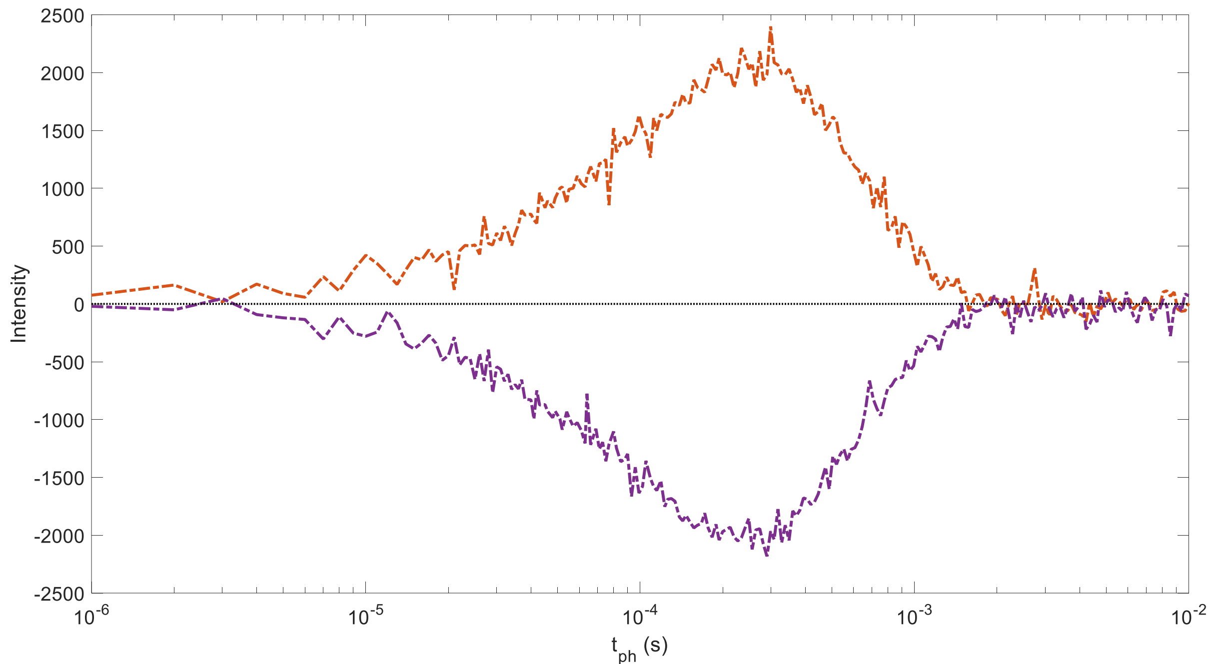

Figure 5.7: An example of a resonance curve for a trap found in the proton irradiated CCD47-20. Each data point represents the intensity of the top pixel (purple) and bottom pixel (orange) of a dipole at different phase times, ranging between 10^{-6} and 10^{-2} seconds.

A non-linear least square fit of the SRH equation 5.1 (discussed previously in section 4.2) is applied to the difference of the absolute values of the intensity plots for the top and bottom pixels to find the emission time constant of the trap. To confirm the emission time constant is accurate strict goodness of fit R-value is chosen at 0.995 to ensure only single traps within the pixel are probed. Further discussion on those profiles for which R<0.995 is found later in this thesis. Figure 5.8 shows a selection of trap resonance curves from trap pumping the CCD47-20 devices that successfully exceed the threshold.

$$I(t_{ph}) = NP_c\left(\exp\left(\frac{-t_{ph}}{\tau_e}\right) - \exp\left(\frac{-2t_{ph}}{\tau_e}\right)\right) \qquad \text{Equation 5.1}$$

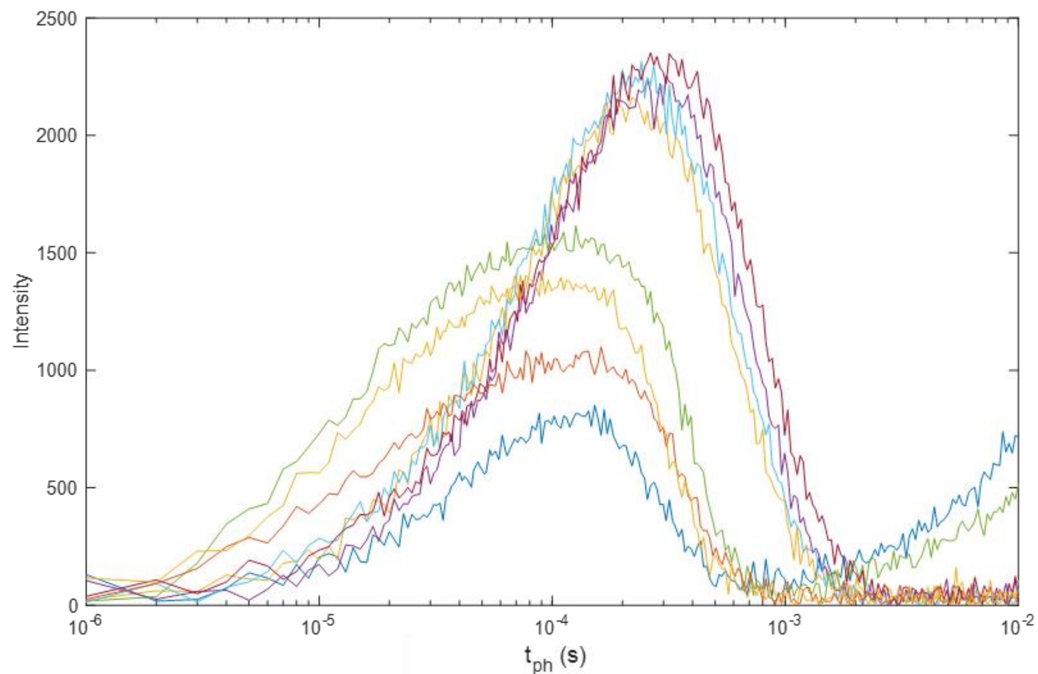

Figure 5.8: A selection of different dipoles resonance curves measured from the trap pumped P6.5 #2 at a 160.4 K.

5.2.4 Probing Region

In Figure 5.9 the theoretical emission time constants for the major known trap species are calculated using SRH theory equation 4.2 and the dashed box represents the phase times and temperature range achievable with the Stirling setup. The minimum temperature of the Stirling cooler at ≈145 K and temperature stability falls off beyond ≈170 K. A stable temperature is necessary for trap pumping to accurately extract the emission time constant of a dipole, with the Stirling/heater combo capable of ± 0.1 K. Work by Hall (2) demonstrates the significant shift to the resonance curve from small temperature variations in Figure 4.7 (d). The phase times and the temperature range chosen are ideal for study into the emission time constants of the double acceptor silicon divacancy, the most dominant trap species related to the degradation of parallel CTE.

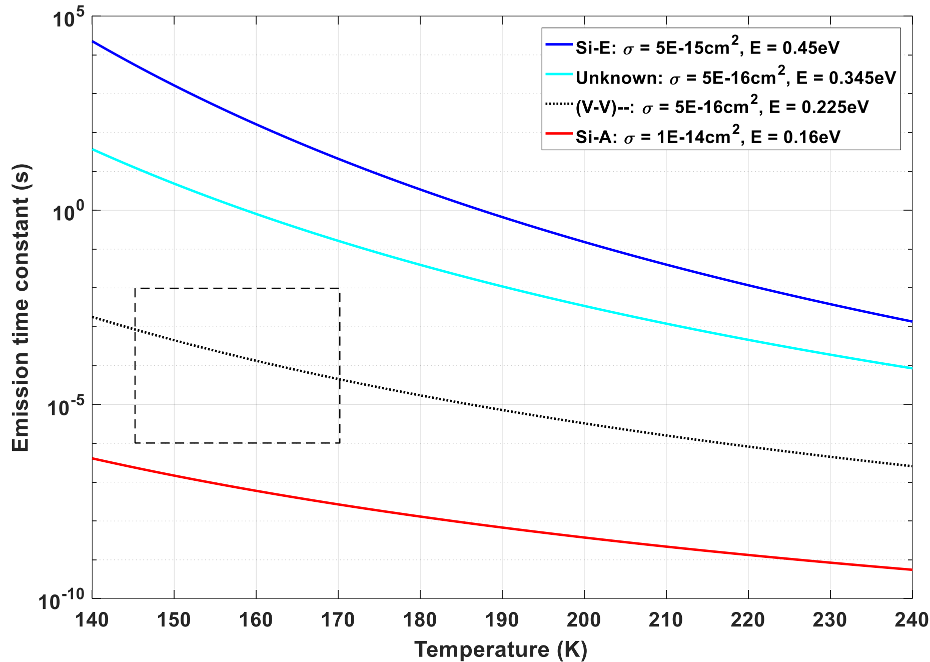

Figure 5.9: Emission time constant vs temperature, for the most prominent n-channel defects. The dashed box represents the phase times and temperature ranges that can be probed with the experimental setup. The stable temperature range for the setup is found to be between 150 K and 170 K and the phase time ranges between 10^{-6} to 10^{-2} seconds.

As the temperature increases, the resonance curve is shifted to the faster phase times as the traps gain more thermal energy, increasing the probability to reemit charge and shortening the emission time constant. The partial resonance curves entering from the rightmost edge of Figure 5.10 reveals a slower trap moving into the probing region as temperature increases, which is why these additional "peaks" appear to increase in intensity with temperature. The emerging traps have a larger energy (E_c-E_{trap}) than those in the main measurement region. The emission time constant of a trap is known to be directly affected by temperature variations while other types of dipoles such as potential pockets (section 6.3.2) and hot pixels will not show an equivalent change in resonance peak location. In the proton irradiated CCD, multiple traps are often found in the same pixel but the resonance curves are adequately separated to measure each emission time constant clearly for each trap. Those that are not readily separable are filtered out through the use of only those curved with an R>0.995. The separation of the trap resonant peaks is vital as overlapping curves can distort the emission time constants and skew statistics.

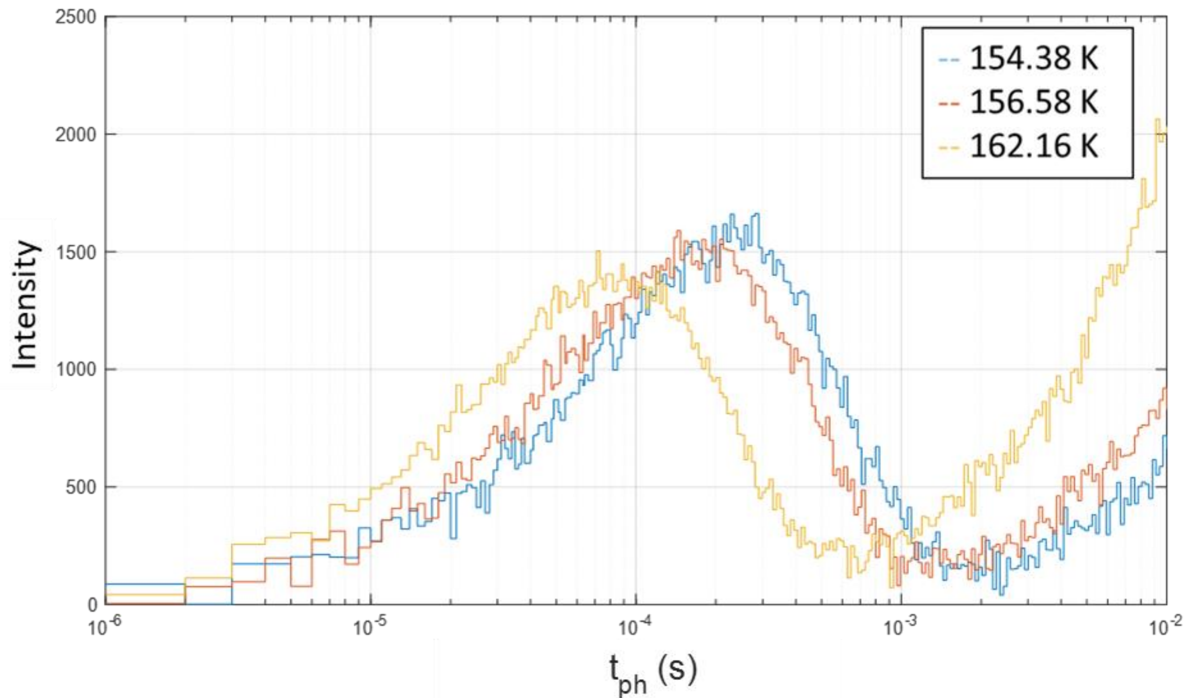

Figure 5.10: Resonance curve from P6.5#2 of an electrically active trap located in a single pixel, changing both intensity and emission time constant with temperature and introducing a new trap from the unprobed region of the trap landscape.

5.3 Proton Trap Pumping Results

The trap properties for two proton irradiated devices with energies of 6.5 MeV and 72.8 MeV are studied to find the impact of proton energy on the distribution of emission time constants and the inherent trap properties in detectors. Alongside its dominant impact on parallel CTE, the silicon divacancy is widely studied because of its presence in both n- and p-channel devices and the possibility for their formation is not heavily dependent on impurity concentration. The fitting statistics are summarised here to show the unsuccessful fits that are possible and variations between the two devices.

5.3.1 Trap Detection

As discussed in (3), 6.5 MeV proton interactions with silicon are dominated by point defects and single cascade effects. Higher energy proton and neutron interactions are predicted to be dominated by nuclear reactions, which manifest as clusters of defects. Shown in

Figure 5.11 are several dipole resonance curves where subplot (A) demonstrates a good fit and the remaining resonance curves fail to extract an emission time constant. The commonality between these failed fits is the amplitude exceeds the maximum pumping efficiency for a single trap which here would be 25% of the 10000 electron flat field signal. Observed in subplot (B) are two electrically active traps in the dipole that are pumping signal from the same charge packet which summates the resonance curves of two traps together. This is evident by the extension of the resonance curve, with a drop in intensity at $\approx 2 \times 10^{-4}$ seconds, showing two traps with different emission time constants were being pumped under the same pixel. The standard method used for mitigating the effects of trap damage (CTI) is to optimise the temperature or the readout speed, so that the traps emit significantly more quickly or more slowly relative to the clock timing/charge transfer timings. It is expected that the higher energy 72.8 MeV irradiation will produce more clusters because of the dominance of nuclear interactions in silicon at that energy, though this may be a representation of two normal traps that both appear in the buried channel and are electrically active. The ability to measure the emission time constant is limited here because the two traps obscure one another's resonance features.

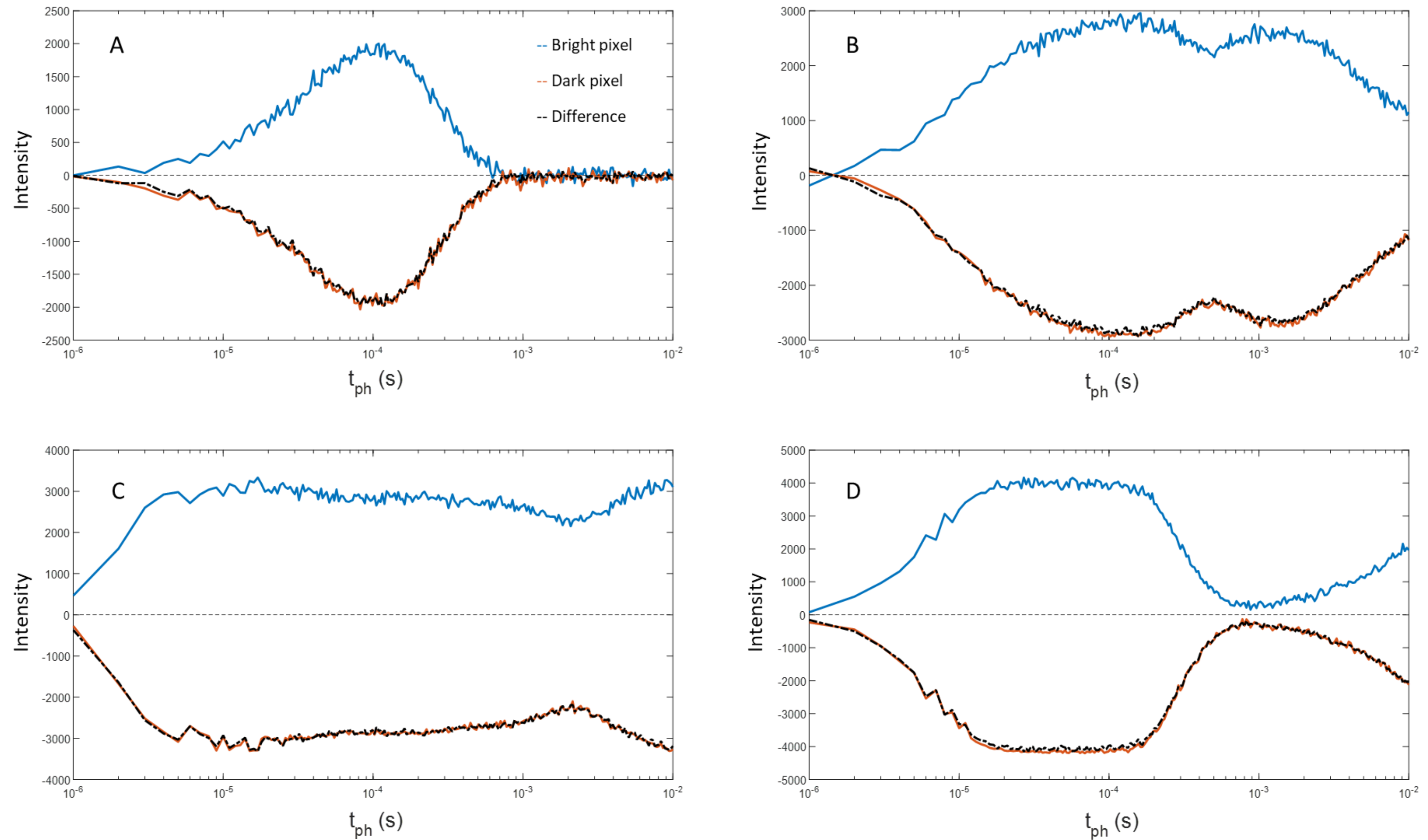

Figure 5.11: Different types of proton induced resonance curves. A) Single trap resonance curve with an amplitude the 25% maximum pumping efficiency. B) Multiple resonance curved of at least two neighbouring traps with similar emission time constants. C) Multiple overlapping traps with an additional trap emerging from the slower phase times. D) Standard single resonance with a larger that 25% efficiency indicating multiple traps with the same emission time constant. A dashed zero line is used to emphasise the mirroring of the resonance curves.

The percentage of dipoles for which a successfully fit can be attained and an emission time constant extracted is shown in Figure 5.12. The reduction in fitting efficiency with increasing temperature is due to the edges of resonance curves approaching the detection limits and new resonance curves entering the detection region that are incomplete such that the emission time constant cannot accurately be extracted. The inability to measure emission time constants for all dipoles demonstrates that when dipole counting an individual frame at a single-phase time, the number of traps in the image region can be overestimated. A sweep of different phase times is necessary to confirm if the trap is “real”, with its own resonance curve and phase time dependence, and if there are other traps with similar emission time constants that extend the resonance curve which distorts the emission time constant. When comparing the two devices a small increase of approximately 2.5% in the fitting rate is found for the 6.5 MeV proton device which is predicted to dominate the non-coulombic interactions with point defects/single cascades rather than from clustering with more disordered lattice sites for the 72.8 MeV protons.

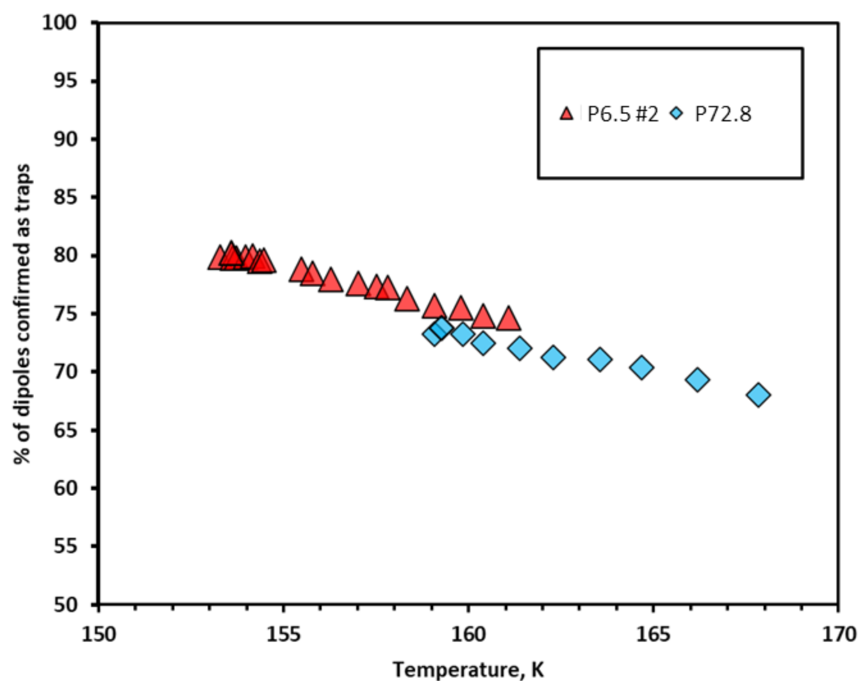

Figure 5.12: Percentage of dipoles found for a complete trap pumping run at multiple temperatures that accurately fit the SRH equation to measure the emission time constant.

5.3.2 Traps Present From Manufacturing

To understand the impact of radiation damage on the production of traps first the unirradiated devices need to be thoroughly characterised. The initial emission time constant distribution of the CCD47-20s and CCD347-20s are predicted to be similar, with both devices sharing many traits including crystal growth method, pixel size and count, gate widths and the depth of the back-thinned silicon at ≈14 µm. The trap properties are measured for an unirradiated CCD347-20 by trap pumping at 160.4 K. Figure 5.13 shows the emission time constants extrapolated from the resonance curves of all traps found in the image region. Here are three distinct peaks that can be attributed to the double-acceptor silicon divacancy (based on previous studies (4,5)) and two as of yet unidentified "inherent" defects. These peaks represent different trap species found across the imaging region that are not radiation-induced and even at low trap counts indicate a spread in the emission time constants rather than sharp peaks. This suggests that these are traps present from manufacturing (i.e. not through radiation damage) and still exhibits a distribution of emission time constants (and therefore individual energy levels and cross sections) rather than a single discrete value for each trap species. The intrinsic defects labelled X1 and X2 are tentatively identified as the B_iO_i and C_iP_s (III) defects at 0.25 eV and 0.23 eV respectively as they overlap with the emission time constant locations of the minor peaks and the formation is independent of vacancy production in the silicon.

The presence of a small number of traps in unirradiated silicon is expected, with imperfections introduced during the manufacturing process from impurities such as oxygen and carbon, additional vacancies from lattice misalignments or damage during the ion-implantation process which fail to be annealed out by heat treatments. The inherent defects appear to be linked to CCDs from the same wafer as they are found inconsistently between batches. The peak at the limit of the detection range is for dipoles with resonance curves that extend beyond the probing region and therefore the emission time constant cannot be accurately measured. Repeating the measurements at a higher temperature would shift the resonance curves of the slower emitting traps into the probing region and will be investigated in future work.

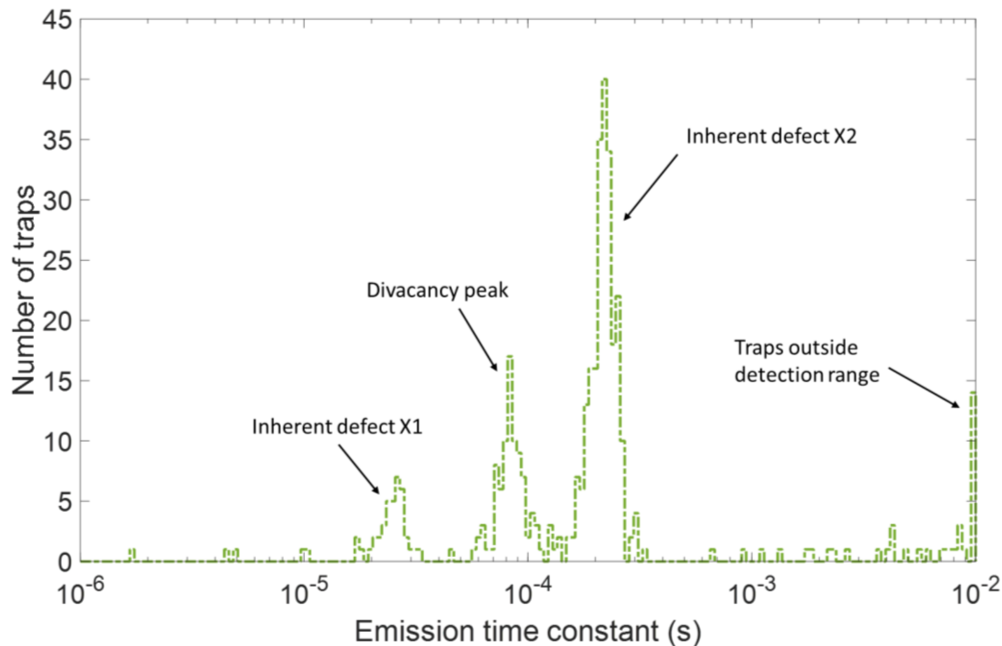

Figure 5.13: Unirradiated CCD347-20 emission time constant histogram for a dataset obtained at 158.30 K that shows the divacancy peak and the inherent defects found from the manufacturing process and unmeasurable neighbouring traps outside the detection range.

5.3.3 Traps Produced by Proton Irradiations

By irradiating to a typical five-year proton dose for a sensor in a satellite at L2 it is possible to emulate the space radiation environment and improve our understanding of the trap properties induced by proton radiation on CCDs. As before, each count on the histogram of Figure 5.14 represents the emission time constant of an individual trap, measured across a range of pumping times from 1 µs to 10,000 µs at a fixed temperature of 160.3 K that is accurate to ± 0.1 K. Comparing the proton irradiated trap landscape of Figure 5.14 to the unirradiated CCD347-20 trap landscape a significant increase in the peak intensity is observed following irradiation for both tested proton energies as more traps are produced in the buried channel. The key features of the histogram are the major peak, the ‘fast tail’ feature, the peaks at the extremes of the pumping times. A significant tail feature is observed out of the major peak towards the faster emission speeds for both energy levels of proton irradiations and is observed when the peaks are normalised in Figure 5.15. While the ‘fast tail’ feature could be attributed to a skewed distribution, each point is individually measured and the resonance curves are consistent following repeat measurements such that the ‘fast tail’ is considered to be a real feature

and either reveals a spreading of the energy levels of the divacancy or an additional broadly spaced trap as repeat measurements in Figure 5.16 find near-identical emission time constant trap properties.

For correction measurements of CTI, the energy level and cross sections of identified traps had until recently been expected to be of fixed values for the double-acceptor silicon divacancy (at least for the purposes of CTI correction). The histograms presented here show that instead of a single sharp peak, a broad distribution of emission time constants is found where either the energy level or effective cross sections are inconsistent. The distortions in the widths of the peak may come from a multitude of factors including the Poole-Frenkel effect which lowers the trap barrier when a trap is in a high electric field or lattice strain bending of the energy levels suggested in (6,7).

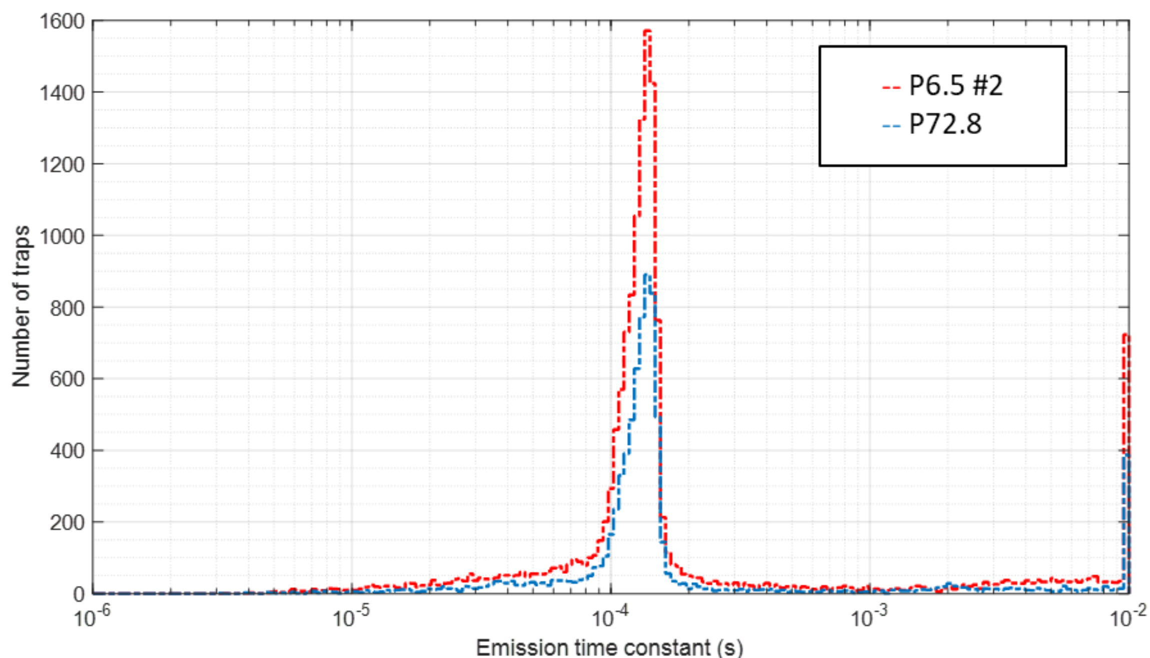

Figure 5.14: Trap landscape comparison for P6.5 #2 and P72.8 at 160.38 K.

A near-identical distribution of the emission time constants is found in Figure 5.15 between the 6.5 MeV and 72.8 MeV proton energies when rescaling (min-max normalisation). This clearly demonstrates the damage distribution is consistent for both devices which presents some very interesting discussion. Firstly, the difference between proton energies will signify the nuclear interaction mechanisms for 72.8 MeV protons dominated by multiple subcascades and the 6.5 MeV

protons dominated by single cascades (3) still produce an identical damage distribution. It is a possible indication that coulombic displacement events dominate the traps generated in the buried channel. However, as stated in (7), displacement damage is mainly present in cluster regions where divacancies are favoured.

Secondly, the two different irradiation facilities provide almost identical distributions of the divacancies emission time constants which suggests that the energy range from 6.5 MeV to 72.8 MeV produce similar divacancy configurations. The work of (2,4,5) found variations in the emission time constant distributions when irradiating despite using the identical irradiation facility at the same proton beam line energy at 6.5 MeV which indicates at the time of irradiation that the trap landscapes should not be changing between irradiations and instead a quirk of the different trap pumping methods used. In (5) there is discussion on the “split peak” observation found in (4) being a possible fitting error that arises from the difficulty to distinguish between different resonance curves with specific pumping schemes.

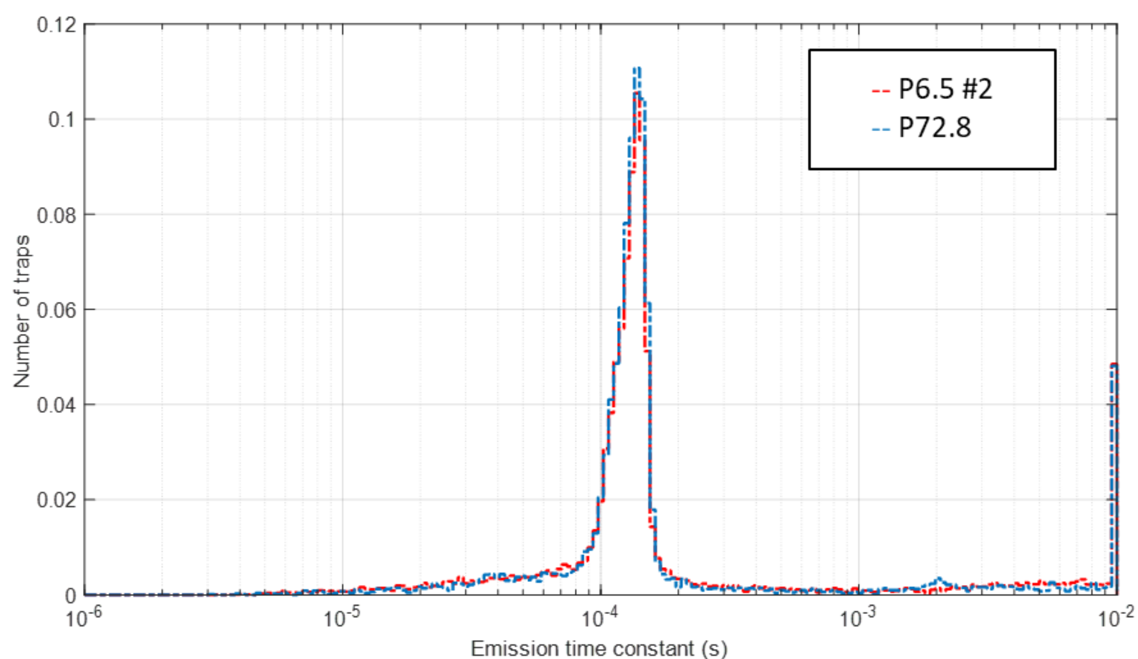

Figure 5.15: Normalised trap histogram for P6.5 #2 and P72.8 at 160.4 K.

To demonstrate the consistency of the trap pumping results, a repeat measurement is completed for P6.5 #2 trap pumping at 153.6 ± 0.1 K as shown in Figure 5.16. This shows the features of the histogram such as the 'fast tail' of the major peak are real and repeatable. The small number of inconsistencies can be attributed to traps found in the low-density regions at the edge of the charge cloud with a maximum amplitude comparable to the background signal or Random Pumping Signal (RPS) traps discussed further in Chapter 7.

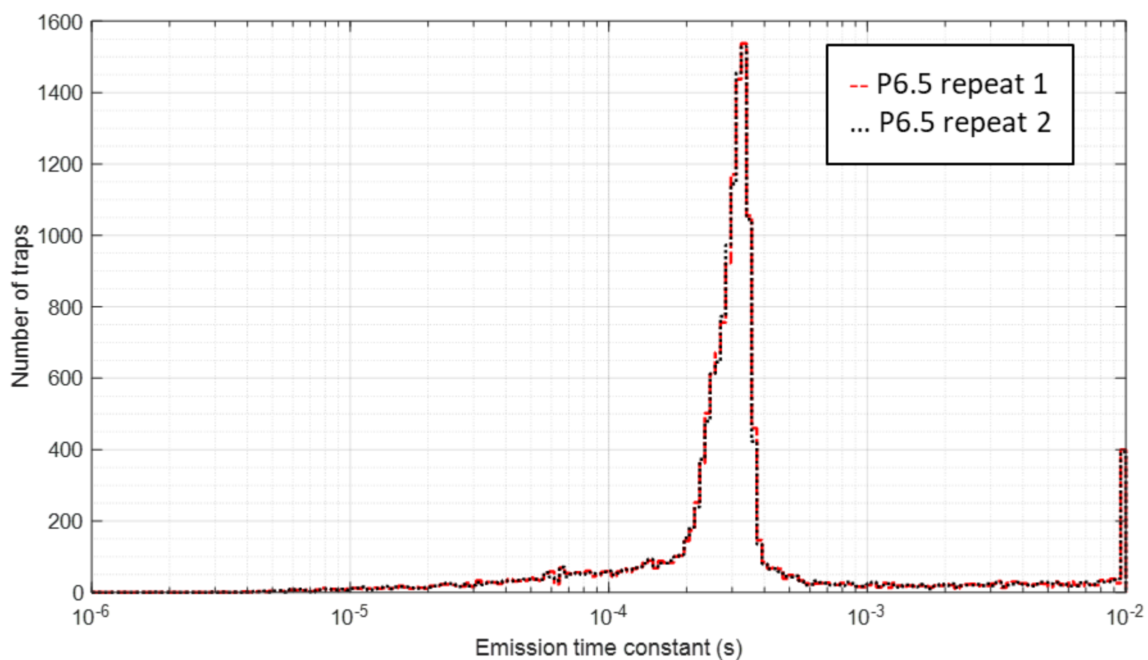

Figure 5.16: Repeat trap pumping measurements at 153.6 K demonstrating near-identical emission time constant repeatability.

5.3.4 Energy Level

The energy level of the double-acceptor silicon divacancy is contentious in the literature, with multiple measurement methods reaching various energy levels, typically found at either 0.21 eV or 0.23 eV. To calculate the energy level of the divacancy using the trap pumping two different approaches are taken. The first approach plots the mode value of the emission time constant histograms that are previously shown in Figure 5.16 at multiple temperatures. The mode value represents the most commonly occurring configuration of an electrically active silicon divacancy that successfully pumps signal.

The mode emission time constants at multiple temperatures are plotted for P6.5 #2 and P72.8 in Figure 5.17. The cross section, entropy factor and field enhanced emission are combined into a single term that we will refer to as the “effective cross section” as they cannot be separated by fitting. The energy level is calculated by solving the SRH equation 4.2 with the effective cross section fixed to the literature value of 5 x 10^{-16} cm^2 (2). The energy level of the double-acceptor silicon divacancy at E_C - 0.226 ± 0.003 eV is consistent with the measurements of (5) for CCD201s, also irradiated with protons at 6.5 MeV.

While this measurement is remarkably consistent for the two separate devices the spread of energy levels is not accounted for in this method. If a spread in energy levels is occurring through effects such as Pool-Frenkel barrier lowering, then the mode energy level will represent an average effect of a divacancy on a charge cloud found on a CCD.

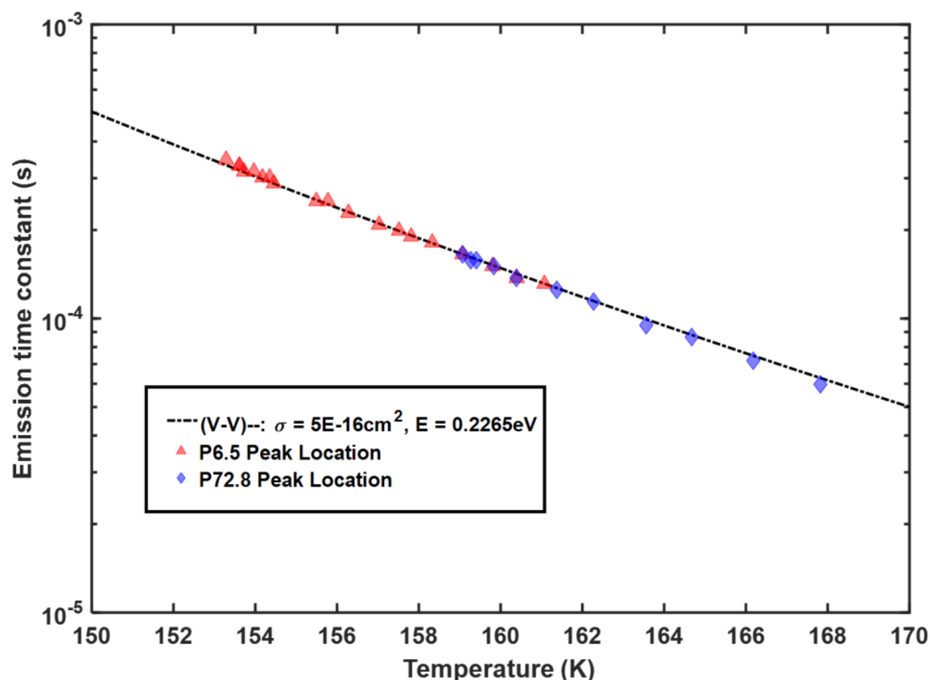

Figure 5.17: Emission time constant peak locations of the 6.5 MeV and 72.8 MeV proton irradiated devices across the parameter space. The cross section of 5 x 10^{-16} cm^{-2} found by (9) was used for the calculation. The full parameter space this is a part of is found in Figure 5.9.

The second energy level measurement method is necessary for understanding the variation of the individual traps rather than the mode the major divacancy peak for the emission time constant histograms. The change in emission time constant with temperature is tracked for every divacancy measured in the image regions of both devices and a non-linear least squares fit is used to find the energy levels in the identical method to the first method. The spread in the energies of the proton irradiated divacancies is shown in Figure 5.18 which appear consistent with (4,5) where a broad energy level peak is observed which indicates variations in the energy levels are consistent through multiple lattice strain may be the contributing factor to the trap landscape around the mode. The results suggest a real physical spread in the proton-induced divacancy energy levels. The mode energy level is measured at 0.226 ± 0.002 eV, again in strong agreement with literature values for the silicon divacancy. The 'fast tail' feature of the emission time constant histograms and spreading of the energy levels are found for the divacancy and additional tests on all measured traps confirm the feature is consistent across multiple temperatures. The normalised distribution of trap energy levels are consistent for 6.5 MeV and 72.8 MeV proton irradiated devices across all pixels, providing further evidence that the proton energy level creates traps that are functionally identical and that the spread of the traps effective energy level is real in CCDs.

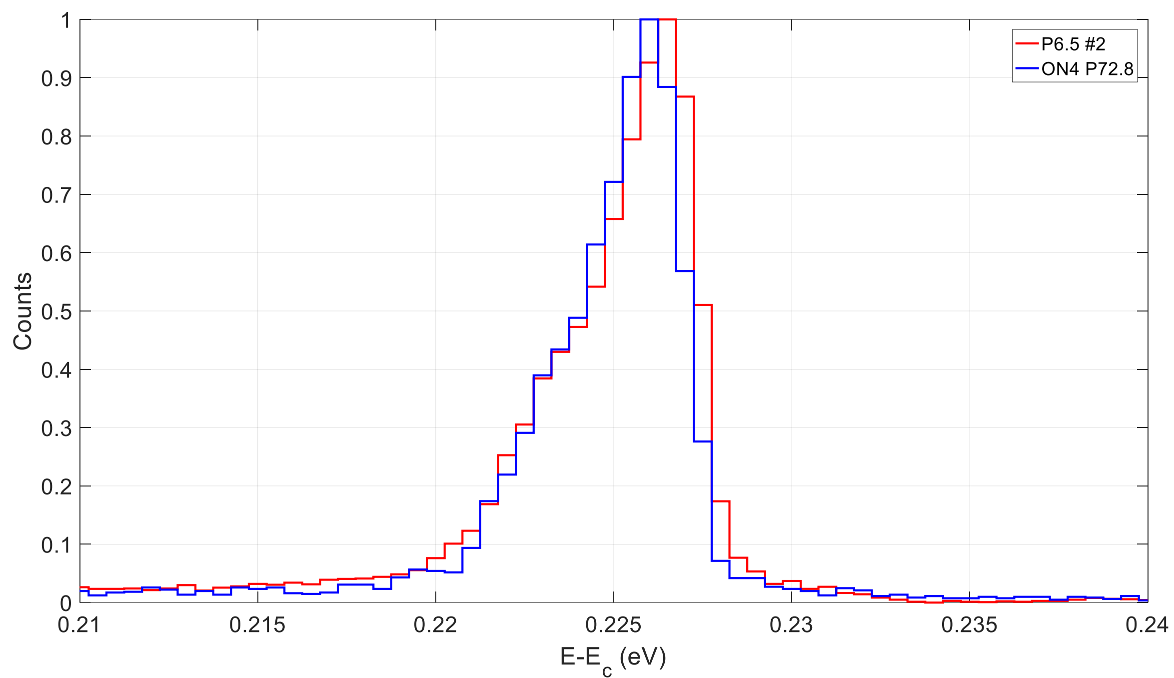

Figure 5.18: Energy levels using rescaling (min-max renormalisation) with a fixed cross section of 5 x 10^{-16} cm^2

5.4 Summary

A first of its kind trap pumping comparison study on the effect of different proton energy levels on the trap properties of CCDs has been conducted. Normalised trap properties are found for two CCD47-20s irradiated at two different facilities with different proton beamline energies of 6.5 MeV and 72.8 MeV, at two different fluences and find almost identical emission time constant histogram features and mode values for the emission time constant of the double acceptor silicon divacancy. As the emission time constant resonance curves are unique to each pixel and repeatable for multiple trap pumping runs it shows the distribution of the emission time constant is a spread of values rather than a delta function for the double-acceptor silicon divacancy. The energy level of the divacancy is found at 0.226 ± 0.003 eV in agreement with (5) and a real spread of the traps energy level is consistent between both devices. Both the emission time constants and the energy levels showing a distribution rather than a single delta function provides a strong argument that the correction method used for missions such as Hubble and Euclid's VIS instrument needs to consider a pixel by pixel analysis of individual traps to accurately correct the effects of radiation damage on the detector.

5.5 References

1. CCD47-20 [Internet]. Teledyneimaging.com. 2020 [cited 15 July 2020]. Available from: https://www.teledyneimaging.com/en/aerospace-and-defense/products/sensors-overview/ccd/ccd47-20
2. Hall D, Murray N, Holland A, Gow J, Clarke A, Burt D. Determination of In Situ Trap Properties in CCDs Using a "Single-Trap Pumping" Technique. IEEE Transactions on Nuclear Science. 2014;61(4):1826-1833.
3. Wood S, Doyle N, Spitznagel J, Choyke W, More R, McGruer J et al. Simulation of Radiation Damage in Solids. IEEE Transactions on Nuclear Science. 1981;28(6):4107-4112.
4. Wood D. Radiation-induced Deep-level Defects in CCD Imaging and Spectroscopy Sensors. Open University (United Kingdom); 2018.

5. Bush N. The impact of radiation damage on electron multiplying CCD technology for the WFIRST coronagraph. Open University (United Kingdom); 2018.

6. Svensson B, Mohadjeri B, Hallén A, Svensson J, Corbett J. Divacancy acceptor levels in ion-irradiated silicon. Physical Review B. 1991;43(3):2292-2298.

7. Kuhnke M. Microscopic investigations on various silicon materials irradiated with different particles with the DLTS method. Deutsches Elektronen-Synchrotron (DESY); 2001.

8. Kuhnke M, Fretwurst E, Lindstroem G. Defect generation in crystalline silicon irradiated with high energy particles. Nuclear Instruments and Methods in Physics Research Section B: Beam Interactions with Materials and Atoms. 2002;186(1-4):144-151.

9. Pichler P. Intrinsic point defects, impurities, and their diffusion in silicon. Springer Science & Business Media; 2012 Dec 6.

Chapter 6: Gamma Radiation Damage

6.1 Introduction

This chapter focuses on the impact of high energy *photons* on the trap landscape for CCDs using the trap pumping technique. Irradiation methods such as energetic proton and neutron bombardments are known to produce clusters of vacancies and the lattice strain associated with the increased damage to a localised region is believed to obfuscate the energy levels of the silicon divacancy (1). Studying the displacement damage effects of a cobalt-60 source (^{60}Co) is useful because the most energetic interactions only transfer enough energy to create *point* defects in the silicon lattice, reducing the strain on the surrounding lattice and allowing the study of the hypothesis that proton/neutron irradiation damages the lattice around the trap site, thus causing the spread in energy level seen in the proton Chapter 5. The highly ionising gamma radiation is found to have other adverse effects on the thin gate CCD which are measurable through the trap pumping technique.

The devices were initially irradiated as part of an ESA characterisation report, comparing performance changes of CCD and CMOS technologies following gamma irradiations. After the study was completed the devices were trap pumped to find the displacement damage effects of ^{60}Co gamma irradiations. The devices analysed in this chapter are highlighted in Table 6.1.

Table 6.1: Summary of the irradiation conditions of devices in this study. Devices discussed in the chapter are highlighted. All irradiations were performed at room temperature. All trap pumping tests were conducted through

Device type	Interacting particle type	Energy	Facility	Dose	Biasing during irradiation	Shorthand name	Irradiation under vacuum	Irradiation date
CCD47-20	Proton	6.5 MeV	STERIS	3.37×10^{9} protons/cm^{2}	Unbiased	P6.5 #1 & #3	Yes	09/09/2017
		6.5 MeV		6.74×10^{9} protons/cm^{2}		P6.5 #2		09/09/2017
		72.8 MeV	Paul Scherrer Institut (PSI)	2.53×10^{10} protons/cm^{2}		P72.8		14/05/2016
		200 MeV		5.16×10^{10} protons/cm^{2}		P200		14/05/2016
	Electron	1 MeV	ONERA GEODUR	10 krad		E1		21/07/2016
CCD347-20	Unirradiated	-		-	-	C0	-	
	Photon	Cobalt-60 source	ESTEC - ESA	50 krad	Clocked	G50	No	21/06/2017
				100 krad	Clocked	G100C		
				100 krad	Clocked & long int	G100CI		
				200 krad	Clocked	G200C		
				200 krad	Clocked & long int	G200CI		
	Neutron	Californium source 2.15 MeV	ISIS	5.00×10^{9} neutrons/cm^{2}	Unbiased	N2.15	No	07/04/2018

6.1.1 The CCD347-20

The devices used in this gamma irradiation study are Teledyne-e2v CCD347-20s which are based on the same architecture as the CCD47-20 but with a reduced gate oxide thickness. The devices have extremely low noise amplifiers making them ideal for scientific applications, an active imaging area consists of 1024 × 1024 pixels, with each pixel area measuring at 13 µm × 13 µm and an active silicon depth following back-thinning of approximately 14 µm. The schematic layout of the CCD347-20 is identical to the CCD47-20 and is shown in Figure 5.1 from the previous chapter.

The devices used in this study are considered thin gate with a dielectric thickness of 15/65 nm oxide/nitride (compared to the typical 80/80 nm or 40/40 nm thicknesses used in standard CCD47-20 designs). The devices are considered radiation-hard because of a thin gate dielectric which reduces the flat band voltage shift due to an applied Total Ionising Dose (TID) as the flat band voltage shift is roughly proportional to the square of the gate thickness (2). The CCD347-20s operate in Non-Inverted Mode Operation (NIMO) and relative to AIMO devices have several advantages such as lower DSNU and greater full-well capacity at the cost of a larger dark signal. These devices can be trap pumped in all schemes as they do not have an implant and therefore allow backclocking.

6.1.2 Irradiation Facility

In a related study, seven CCD347-20s were irradiated at the European Space Research and Technology Centre (ESA ESTEC) ^{60}Co facility in Noordwijk, Netherlands. The setup is demonstrated in Figure 6.1 and Figure 6.2where the devices are irradiated with no surrounding electronics and the output cable is passed through a shielding wall to an XCAM controller in the control room. The source had an activity of 71.19 TBq at time of irradiation (20th June 2017) and TID dosimetry measurements were made in water and converted to the equivalent silicon dose. The 100 krad dose was chosen based on the predicted end of life dose for JUICE.

The devices were biased during the room temperature irradiation while continuously clocking with two different integration times at a ratio of 1:7.6 (i.e. the integration time is 7.6 times larger) to find

the impact of holding particular electrodes high for different periods. The change in biasing schemes is predicted to have a small impact on the annealing behaviour for proton irradiated devices (3). The devices were characterised pre- and post-irradiation using a test camera at the Centre for Electronic Imaging (CEI) at the Open University.

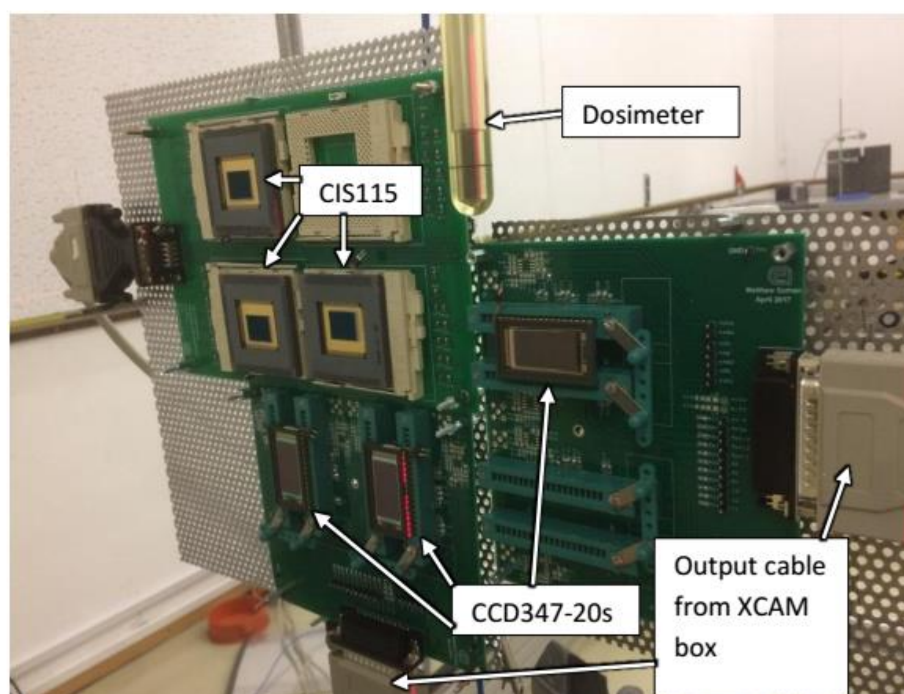

Figure 6.1: Experimental setup for cobalt-60 irradiation at ESTEC.

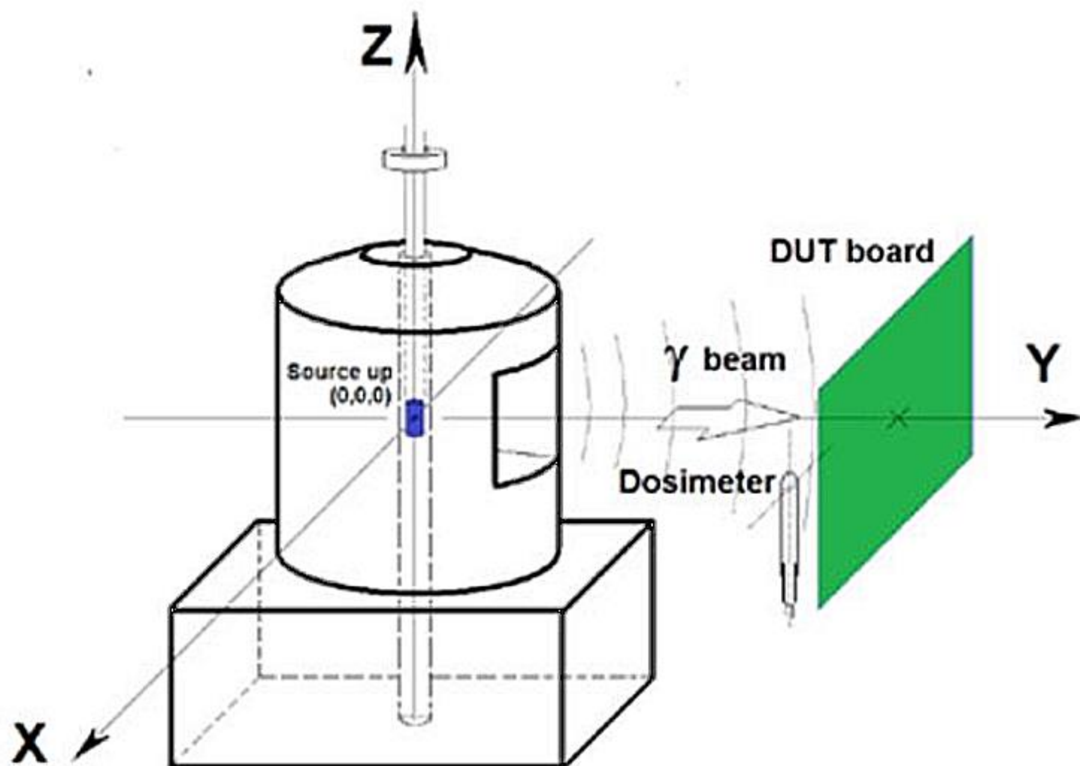

Figure 6.2: Cobalt 60 radiation source and Device Under Test (DUT) board positioning diagram.

6.2 Trap Pumping Measurements

The trap pumping setup was based on the experimental method detailed in section 5.2 for the proton irradiated CCD47-20s. Custom sequencers were built to run the NIMO devices while maintaining identical readout as the CCD47-20s. The temperature range possible for the setup was between 149 K and 168 K. Future tests aim to trap pump at warmer temperatures to measure different trap species.

The CCD47-20 AIMO devices previously studied are only capable of trap pumping using a single pumping scheme because the implant prevents backclocking. The CCD347-20s are NIMO devices which are built without the implant found in AIMO and as demonstrated in Figure 6.3 allows for probing of additional regions under the electrodes using the same (231’32) scheme. Here, a trapping site captures an electron from the charge cloud and reemits the charge towards the strongest potential (i.e. nearest active gate region). The physical location of the trap under the electrode can

determine if the charge is added to the original or neighbouring charge packet allowing for sub-pixel resolution in the locations of trapping sites.

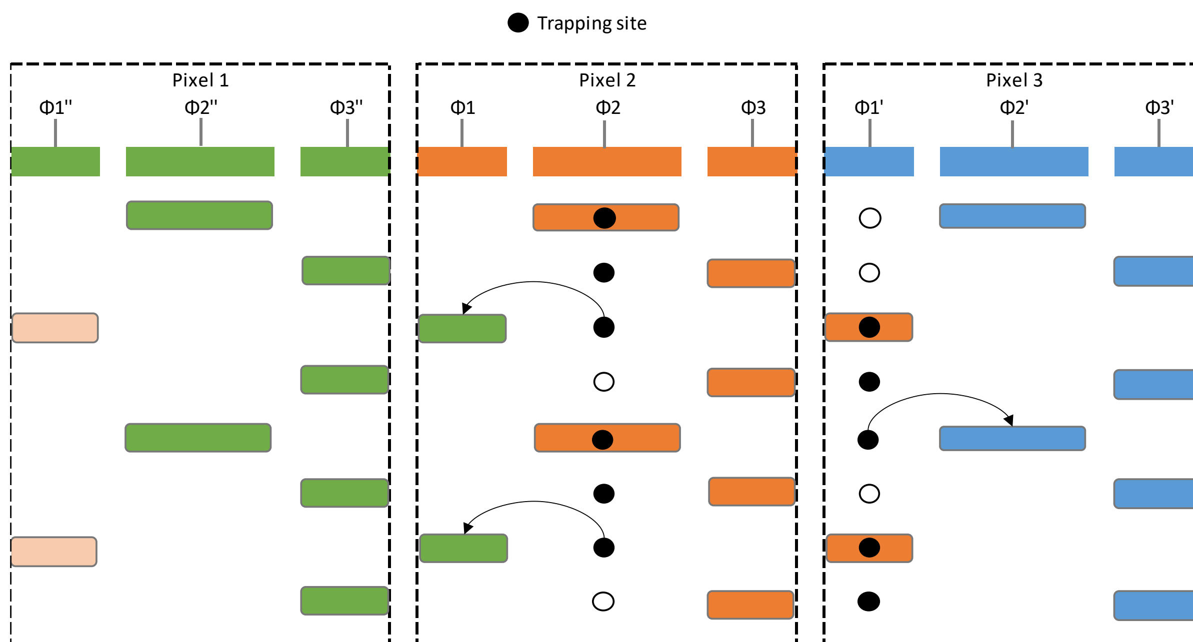

Figure 6.3: Trap pumping from phases (231'32) to cyclically shuffle the charge cloud and produce dipoles for a CCD347-20. The black dots represent the traps that capture the signal from the charge cloud and the arrows show trap reemission is possible in both directions.

A small windowed section of a raw trap pumped frame is shown in Figure 6.4, demonstrating the two different dipole configurations possible for NIMO devices that are otherwise in a single orientation in AIMO devices. The orientation of the dipole determines the sub-pixel trap locations which for the pumping scheme 231'32 (where 1' is the 1st electrode in the neighbouring pixel) are observed as either "dark-light" configuration for traps found under ϕ1 or "light-dark" for traps found under ϕ2 in trap pumping frames. The different intensities of dipoles observed are for traps at different stages of the resonance curve found either at the peak for high intensity or the earlier/later stages of the peak for lower intensities.

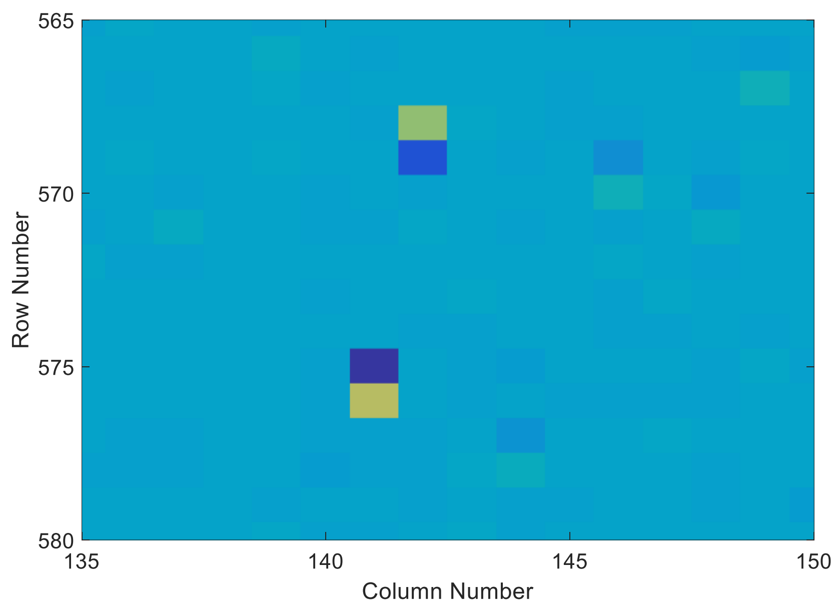

Figure 6.4: Dipoles found in a trap pumped frame for a CCD347-20 with two different orientations of dipoles (dark-light and light-dark).

6.3 Gamma Trap Pumping Results

Trap pumping gamma irradiated CCD347-20s are studied to find the impact of *point* defects on the trap landscape around the double-acceptor silicon divacancy and other potential traps within the measurement region. Gamma rays from ^{60}Co sources damage CCDs through both ionisation damage which accumulates charge in the CCDs gate insulator and displacement events which dominate damage effects observed in CCDs, particularly for the ultra-thin gate designs of the CCD347-20. The photopeaks of ^{60}Co are found at 1.17 MeV and 1.33 MeV where Compton scattering events dominate and produce Compton electrons through the elastic scattering of the gamma rays. The Compton scattered electrons with a maximum energy of approximately 1 MeV are unable to generate clusters, only point defects and the minimum strain to the lattice per displacement interaction.

6.3.1 Trap Detection

As in chapter 5, we can take the dipole measurements across multiple phase times to construct the resonance curves of different traps. An example of dipole measurements for the CCD347-20 is displayed in Figure 6.5, with each trap's resonances curve found for dipoles that successfully fit the fitting threshold. As previously, each point on a resonance curve is measured from the difference

between the absolute intensities of the light and dark pixels for a single trap pumping frame. These trap pumped resonance curves are entirely repeatable and again shift with temperature in agreement with SRH theory.

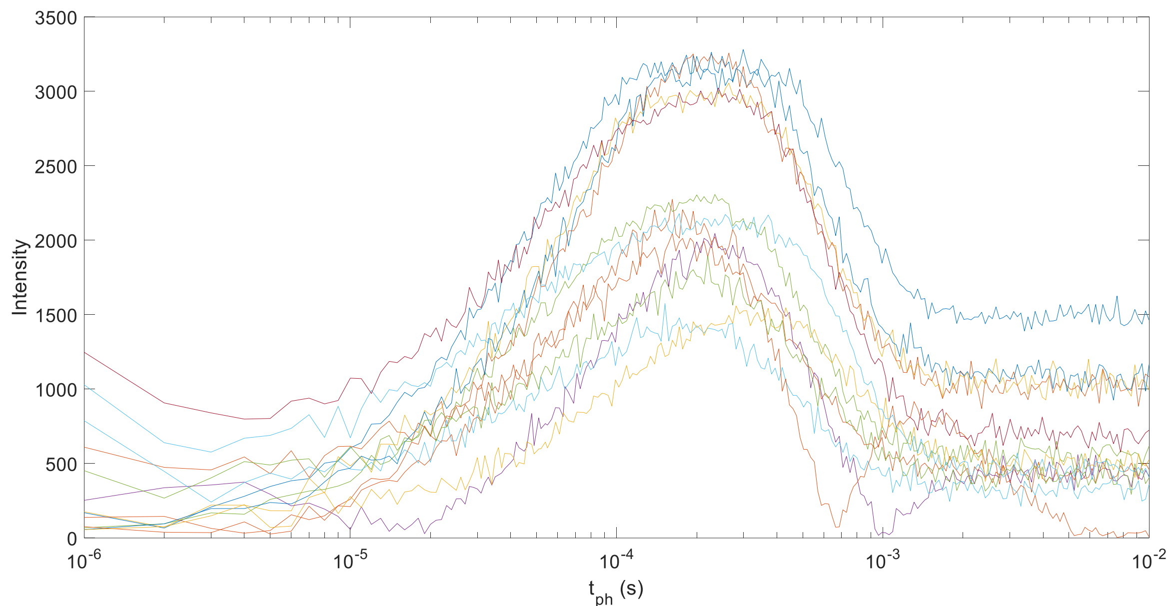

Figure 6.5: Example of multiple resonance curves found in the CCD347-20 G200CI device at 159.9 K, constructed from individual dipoles intensity profiles across multiple phase times (t_{ph}).

Fitting each measured dipole to equation 6.1 (repeated here for ease of reference) and setting an R > 0.995 threshold (set to ensure we are only looking at single traps and not clusters or other phenomena) it is possible to measure the emission time constants for each trap with complete resonance curve in the probing range.

$$I(t_{ph}) = NP_c\left(\exp\left(\frac{-t_{ph}}{\tau_e}\right) - \exp\left(\frac{-2t_{ph}}{\tau_e}\right)\right) \quad \text{Equation 6.1}$$

It is important to understand why dipoles fail to produce clear resonance curves because missions such as Euclid plan to use trap pumping sparingly in the Euclid VIS instrument to focus on observations so practically only a few t_{ph} frames can be taken in the allocated time slot rather than the extensive sweeps used in this study. Displayed in Figure 6.6 is the percentage of dipoles that exceed the threshold to successfully categorise a dipole as a trap which is found to be significantly lower ratio in

the gamma irradiated devices at colder temperatures in the probing range relative to the proton irradiated devices previously studied.

The impact of temperature change on the ratio of fitted traps is striking with a small decrease of ≈10% across the probing range for two proton irradiated devices and a ≈50% increase for gamma irradiated devices across the same temperature range. This phenomenon is discussed further in the next section.

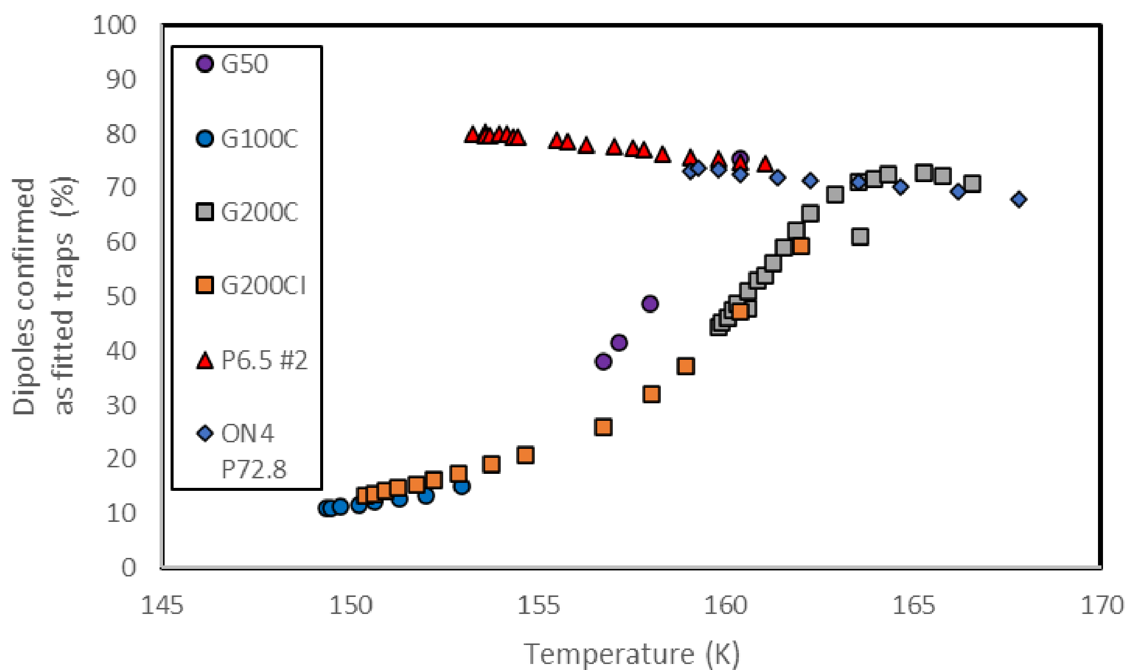

Figure 6.6: Percentage of dipoles confirmed as fitted traps to resonance curves for proton and gamma irradiated devices at multiple temperatures.

6.3.2 Potential Pockets

Through manual inspection of gamma irradiated device's resonance curves with the theoretical equation 6.1, the majority of failed dipole fits did not display the characteristic resonance peaks associated with the "standard trap" discussed in chapter 5. Figure 6.7 demonstrates this non-standard trap, which is found to have a fixed dipole intensity for both dipole pixels. The intensity profiles of the dipoles are mirrored across the dashed zero line indicating charge is being captured from a single pixel and reemitted into the neighbouring pixel, similar to regular traps but without a dependence on phase time. The observation is only observed in gamma irradiated devices because the flat band voltage shift

from the heavily ionising gamma irradiations forces the CCD to operate near the minimum clock voltage which causes effects such as potential pocket observations. The thin gate gamma irradiated CCD347-20s exhibit potential pocket effects whereas the proton irradiated CCD47-20 in chapter 5 fail to produce dipoles with similar features. The gamma irradiated devices were operated at an image clock voltage that was considered optimal during characterisation and while unirradiated, but the TID flat band voltage shift from a significant dose of ^{60}Co photons has caused a flat-band voltage shift.

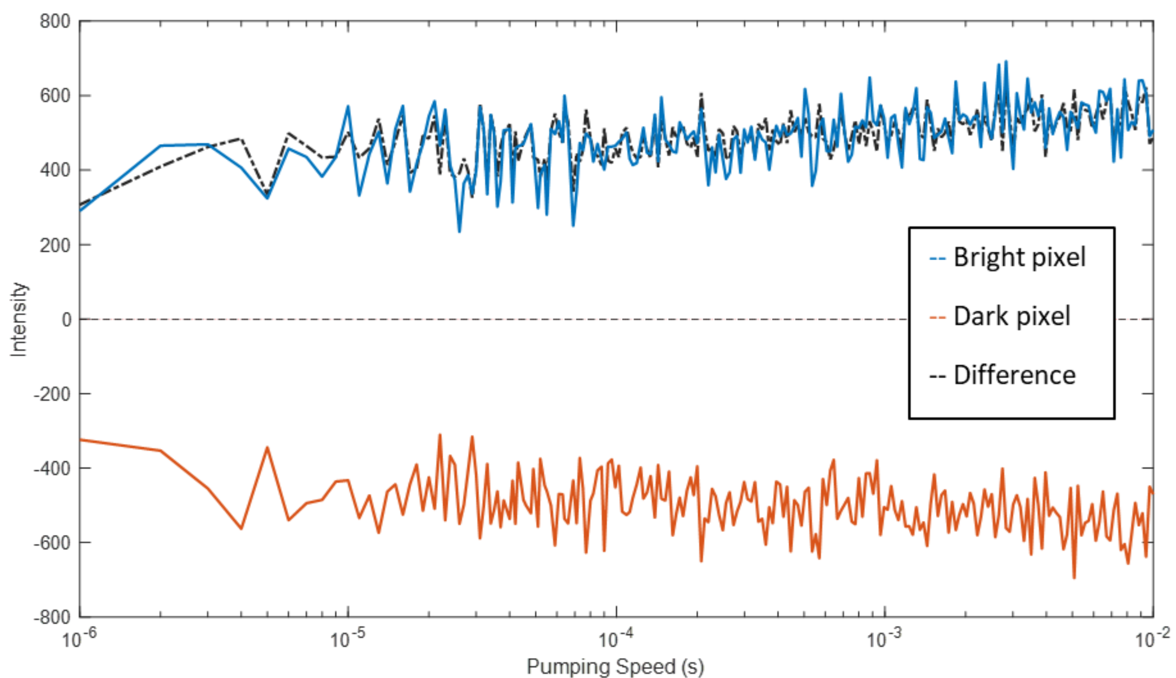

Figure 6.7: Intensity of a potential pocket from the top and bottom pixel of a dipole, pumping in equal and opposite intensities demonstrating charge is being captured directly from the neighbouring pixel.

Potential pockets appear to decrease with temperature as shown by Figure 6.8, dominating the dipole counts for devices G100C and G200C at the colder temperatures and reducing in count as the temperature exceeds 155 K. The reduction in dipole count is consistent across the three devices successfully trap pumped at the temperature range while the trap count increases as more traps enter the detection regions. The potential pockets are found to decrease in intensity with increasing temperature until the intensity is below the threshold necessary to extract a dipole from background noise, at which point the dipole count decreases by a factor ≈2. The apparent trap count is found to

increase with temperature as complete resonance curves enter the probing region as temperature is increased, which is necessary for a measurable emission time constant.

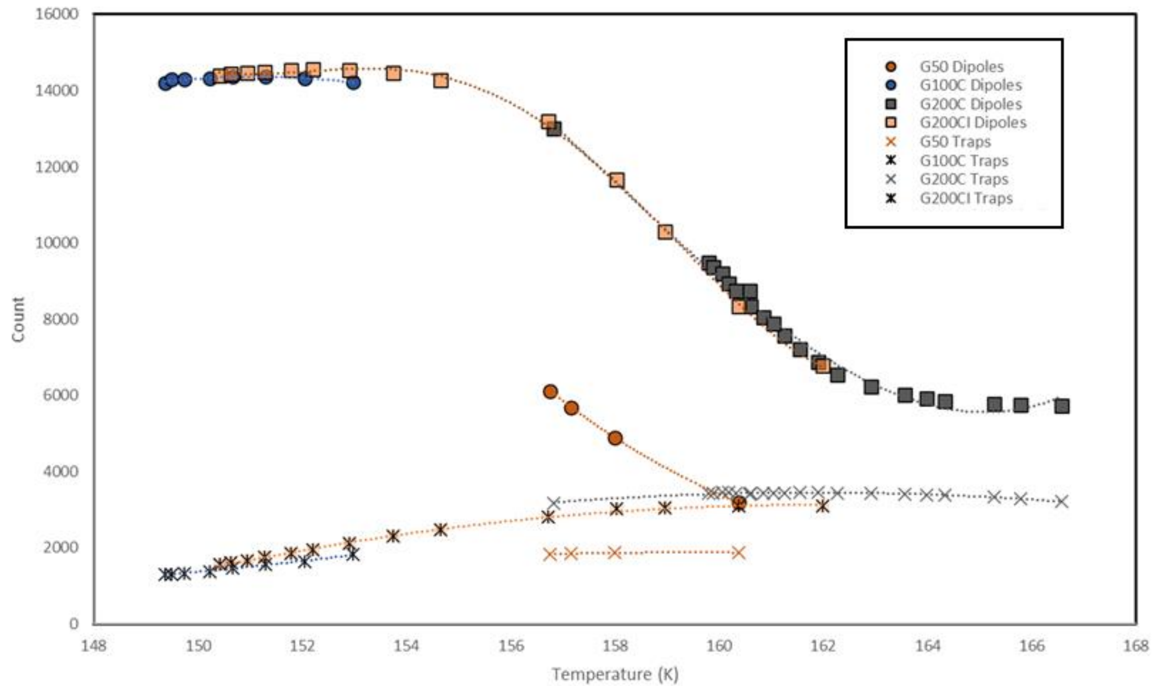

Figure 6.8: Change in the number of dipoles and the number of divacancies measured with increasing temperature. Both the number of dipoles measured and the divacancy count under the major peaks are presented here.

The temperature dependence implied previously in Figure 6.8 is demonstrated for an individual potential pocket in Figure 6.9. The constant pumping intensity that is characteristic to the potential pockets is found consistently for multiple trap pumping sweeps at different temperatures. Figure 6.9 clearly demonstrates the mean intensity of the potential pocket decreasing with increasing temperature until falling below the noise threshold.

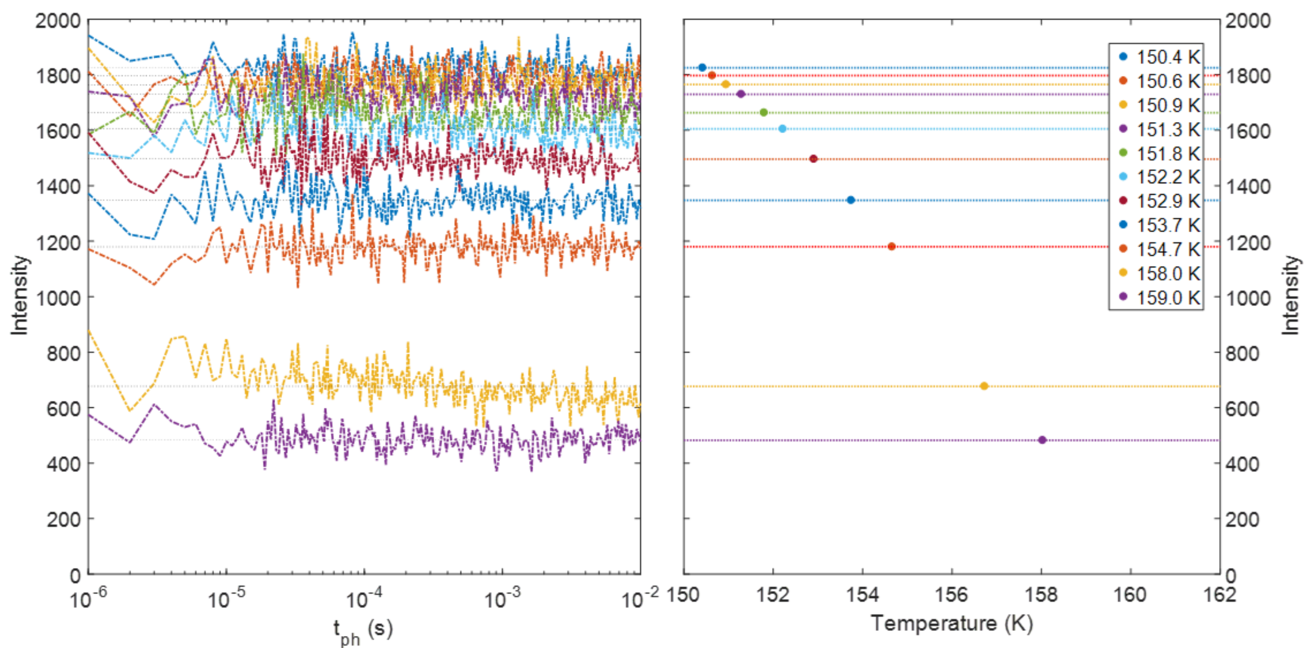

Figure 6.9: The potential pocket intensity profile for a single pixel tracked with temperature (left) and the mean intensity of the potential pocket found in G200CI between 150 K and 162 K (right).

Potential pockets are thoroughly studied in (4), predicting potential barriers to be present in the overlapping regions of gate electrodes at low gate voltages and even stating that "future generation devices with small dimensions and low clock voltages where the electron potential distortions of the silicon substrate in the interelectrode overlap region become significant". To test Taylor's theory, the voltage is increased in 0.5 volt steps to overcome the interelectrode potential barrier where we find the potential pockets disappear from the image regions, Figure 6.10. Here we find increasing the image clock voltage agrees with Taylor and Janesick as the dipole count and the potential pockets decrease in unison. The "fitted dipoles" represent successfully fitted traps with standard resonance curves and show an increase in count of ≈25% between 7.3 V and 11.8 V. This method of detection is useful for satellite missions as a simple onboard characterisation through trap pumping provides information on both the exact traps impacting CTI and improve CTI by increasing the clock voltages to

negate the effects of a flat-band voltage shift. This type of trap is identified as a potential pocket where the potential well shapes and/or depth is incorrect for charge transfer.

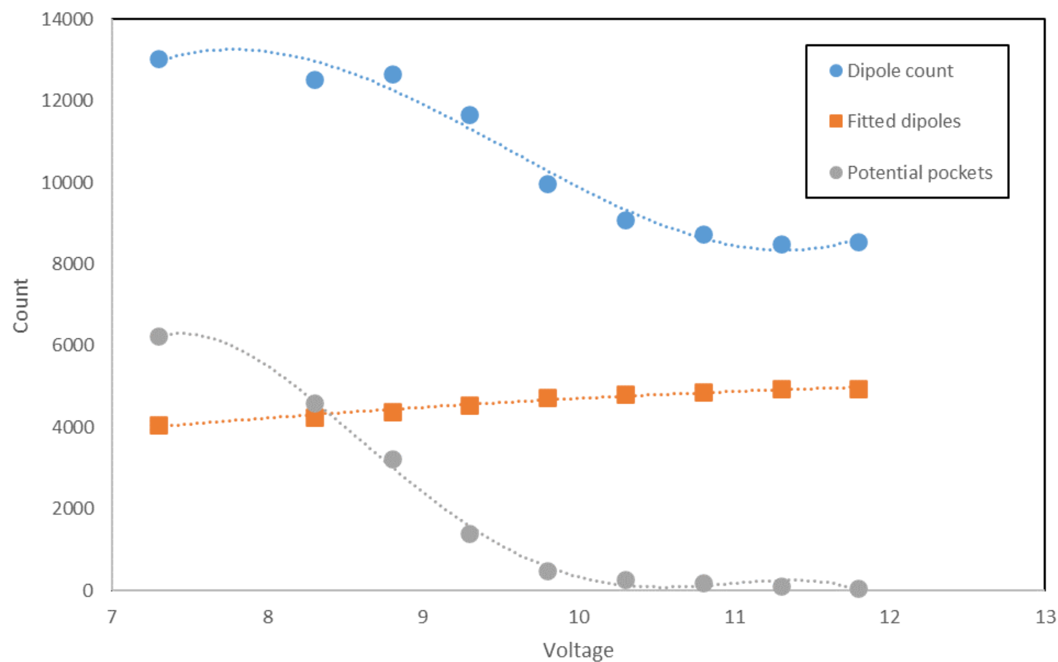

Figure 6.10: Dipole count and potential pocket relationship with fitted traps for device G200C at 156.0 K.

6.3.3 Irradiated Trap Landscape

The trap pumping technique is performed on unirradiated and gamma irradiated CCD347-20s using the 231’32 pumping scheme to find variations in the trap landscapes. The unirradiated CCD347-20 emission time histogram is shown in the previous chapters Figure 5.13 and finds a small number of pixels with the emission time constants of the silicon divacancy and two other manufacturing defects.

Comparing the emission time constant histograms of G50, G200C and G200CI at 160.35 ± 0.05 K in Figure 6.11, three distinct peaks are found representing the double acceptor silicon divacancy, the X2 peak and a new X3 peak. The mode of Figure 6.11 is identified as the peak of the double-acceptor silicon divacancy at 1.37×10^{-4} s which is in good agreement with the theoretical emission time constant at 1.28×10^{-4} s for the divacancy when calculated from the SRH Equation 4.2 using an effective cross section fixed at 5×10^{-16} cm^2 and the energy level at 0.225 eV from (5).

The divacancy count of each major peak at 160.4 K is shown in Table 6.2 and suggests that the introduction rate of divacancies is non-linear with dose, with G50 producing ≈2.1 times the number of identified divacancy pixels per krad compared to G200C and G200CI, which have similar introduction rates to each other. Similarities are found between the divacancy peaks of G200C and G200CI for integrated peak counts and peak widths confirming repeatability of the trap landscapes. The G50 device has fewer divacancy counts as expected when compared to the 200 krad devices and a narrower peak width. The variations in the peaks widths with fluence for *point defect* generating gamma radiation could prove an important distinction for future radiation damage correction algorithms like those described in (6) as the effective energy levels exist as a distribution rather than a single value which would be ascribed to a sharp single peak. It is believed the two intrinsic defects were present before irradiation and are tentatively identified in section 5.3.2 as the B_iO_i and C_iP_s (III) defects as their populations are independent of vacancy counts from displacement damage. Mode locations are consistent and will be compared further in chapter 7.

Table 6.2: Divacancy count from the major peaks of Figure 6.11 at 160.4 K.

Device	Number of identified VV^{--}	VV^{--} production per krad
G50	1876	37.52
G200C	3437	17.18
G200CI	3106	15.53

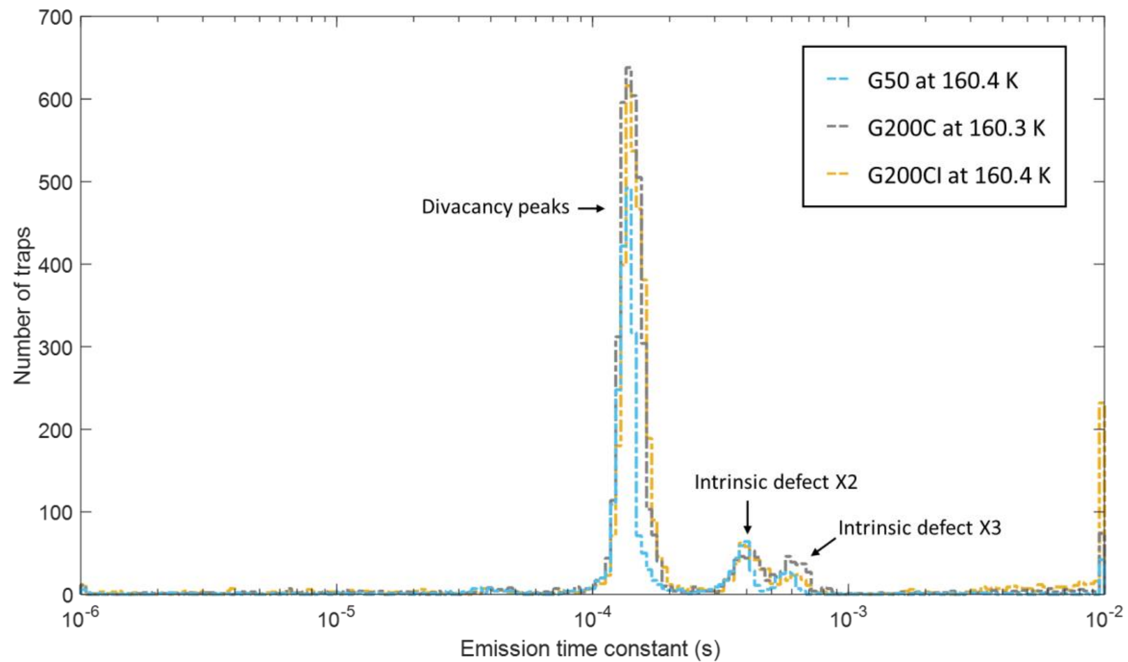

Figure 6.11: Trap pumping emission time constant histogram for multiple gamma irradiated CCD347-20s at ≈160.4 K.

6.3.4 Energy Levels

The divacancy energy level measurements of ^{60}Co irradiated devices is predicted to provide the sharpest peak for energy levels as the interacting photons are less damaging to the surrounding lattice structures than high energy protons or neutrons because of the larger momentum and ability to create *clusters* of defects. Calculations of the energy levels and cross sections are made through non-linear least squares fitting of the SRH equation 4.2 using the emission time constants for each measured trap across the measurable temperature range of the double acceptor silicon divacancy. To accurately measure the energy levels, many trap pumping sweeps are necessary at multiple temperatures while staying in the probing region of the chosen trap.

The energy level histogram is calculated based on the emission time constant data at different temperatures shown in Figure 6.12, where the mode is measured for the divacancy at 0.227 ± 0.03 eV for G100C, 0.225 ± 0.06 eV for G200C and 0.226 ± 0.03 eV for G200CI with an effective cross section fixed at 5 x 10^{-16} cm^2 and errors calculated from the residuals of the least-squares fitting method. The energy levels agree with the literature results of the previous trap pumping studies by (5) with protons.

The width of the histograms is the real spread of energies however the shift in the mean calculated trap energy distribution is likely caused by a systematic increase in fitting error due to a lower number/smaller range of temperatures measured and therefore it is not indicative of a real shift in trap energies. The X2 (and potentially X3) peaks are measured at an energy level of 0.24 ± 0.05 eV, believed to be the B_iO_i defect present in the unirradiated CCD347-20 and all other devices in the CCD347-20 batch. The general energy level features are compared in greater depth in chapter 7 between the proton, gamma and neutron irradiations.

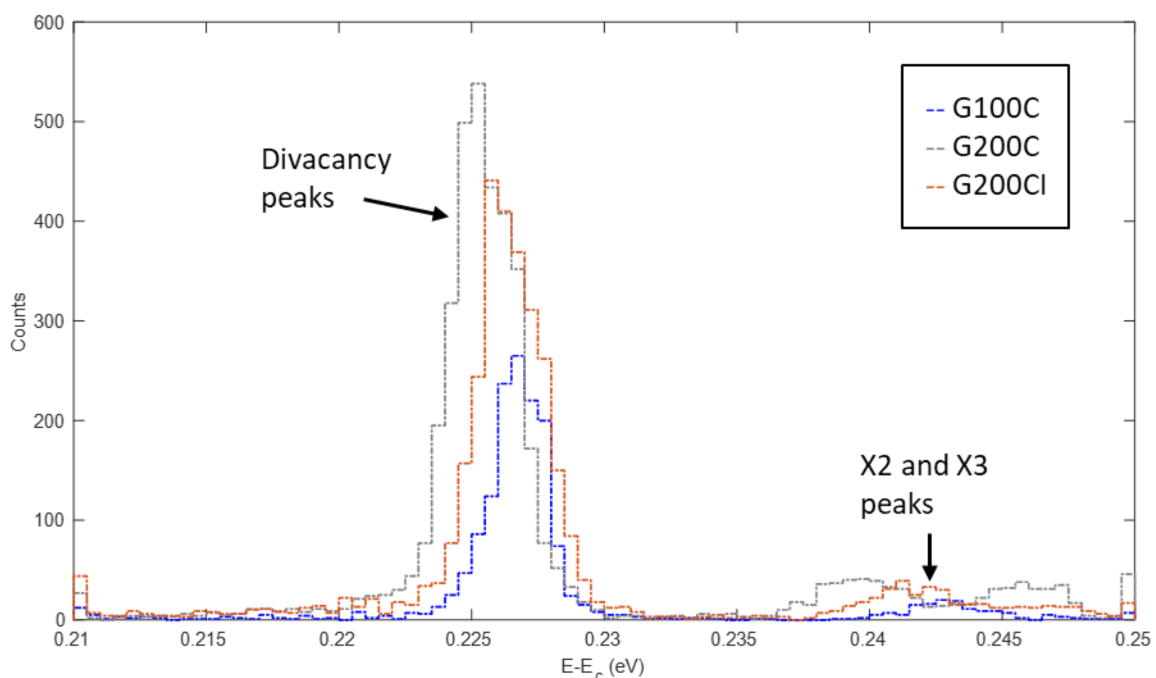

Figure 6.12: Energy levels below the conduction band for gamma irradiated CCDs at the fixed 5 x 10^{-16} cm^2 effective cross section. Mode values for the silicon double-acceptor divacancy are found at 0.227 eV for G100C, 0.225 eV for G200C and 0.226 eV for G200CI.

6.4 Summary

This chapter demonstrated trap pumped gamma irradiated CCD347-20s at multiple temperatures and found the modes of the emission time constant histograms and energy level measurements are consistent with the double acceptor silicon divacancy at 0.225 ± 0.001 eV with energy levels found in a normal distribution rather than a single sharp peak indicating additional effects such as lattice strain

is still present in *point* defects or another phenomenon is happening (such as field enhanced emission). A comparison to the proton irradiated devices will be explored in chapter 7.

Potential pockets are characterised in trap pumped frames and exhibit a fixed pumping intensity regardless of the chosen phase time. The potential pockets are unique to the thin gate CCD347-20s irradiated with a ^{60}Co source rather than the proton irradiated CCD47-20s. The high total ionising damage and the low image clock voltages are believed to cause these observations. Potential pockets can therefore be characterised in trap pumping frames during missions in-flight to find specific pixels where the CTE has degraded and if the clock voltages are high enough following ionising radiation damage. The observations of the potential pockets find:

1. The potential pockets are temperature dependent and are experimentally verified to reduce in pumping intensity as temperature increases from 154 K to 164 K.
2. The potential pockets are suppressed by raising the image clock voltage to mitigate the effects of flat band voltage shifts.
3. The suppression of the potential pocket through either temperature or image clock voltage improves the CTE.

6.5 References

1. Svensson B, Mohadjeri B, Hallén A, Svensson J, Corbett J. Divacancy acceptor levels in ion-irradiated silicon. Physical Review B. 1991;43(3):2292-2298.
2. Burt D, Endicott J, Jerram P, Pool P, Morris D, Hussain A, Ezra P. Improving radiation tolerance in e2v CCD sensors. InAstronomical and Space Optical Systems International Society for Optics and Photonics. 2009 Aug 26 (Vol. 7439, p. 743902).
3. Robbins MS, Rojas LG. An assessment of the bias dependence of displacement damage effects and annealing in silicon charge coupled devices. IEEE Transactions on Nuclear Science. 2013 Dec 2;60(6):4332-40.

4. Taylor G, Chatterjee P. An Evaluation of Submicrometer Potential Barriers Using Charge-Transfer Devices. IEEE Journal of Solid-State Circuits. 1980;15(4):644-650.
5. Bush N. The impact of radiation damage on electron multiplying CCD technology for the WFIRST coronagraph. Open University (United Kingdom); 2018.
6. Massey R, Schrabback T, Cordes O, Marggraf O, Israel H, Miller L et al. An improved model of charge transfer inefficiency and correction algorithm for the Hubble Space Telescope. Monthly Notices of the Royal Astronomical Society. 2014;439(1):887-907.

Chapter 7: Comparison of Multiple Damage Types

7.1 Introduction

The discussion of the proton and gamma irradiations in the previous two chapters have shown the effect of different particle types and energies on the trap landscape of the double-acceptor silicon divacancy and the surrounding defects. At this point many questions remain:

- Are there differences between the proton and gamma irradiations trap landscapes?
- Is the difference between the trap features energy or particle based or a mixture of the two?
- Is there a clear difference between clustering and point defect sources?
- Does the particle type result in different dipole fitting ratios?

This chapter compares the trap landscapes of the proton and gamma irradiations, introduces additional particle types with a 2.15 MeV neutron irradiated CCD347-20 and a 1 MeV electron CCD47-20, and finally compares the various emission time constant histograms for each particle type for a side by side analysis of the radiation damage effects.

Table 7.1: Summary of the irradiation conditions of devices in this study. Devices discussed in the chapter are highlighted. All irradiations were performed at room temperature.

Device type	Interacting particle type	Energy	Facility	Dose	Biasing during irradiation	Shorthand name	Irradiation under vacuum	Irradiation date
CCD47-20	Proton	6.5 MeV	STERIS	3.37 x 10^{9} protons/cm^{2}	Unbiased	P6.5 #1 & #3	Yes	09/09/2017
		6.5 MeV		6.74 x 10^{9} protons/cm^{2}		P6.5 #2		09/09/2017
		72.8 MeV	Paul Scherrer Institut (PSI)	2.53 x 10^{10} protons/cm^{2}		P72.8		14/05/2016
		200 MeV		5.16 × 10^{10} protons/cm^{2}		P200		14/05/2016
	Electron	1 MeV	ONERA GEODUR	10 krad		E1		21/07/2016
CCD347-20	Unirradiated	-		-	-	C0	-	
	Photon	Cobalt-60 source	ESTEC - ESA	50 krad	Clocked	G50	No	21/06/2017
				100 krad	Clocked	G100C		
				100 krad	Clocked & long int	G100CI		
				200 krad	Clocked	G200C		
				200 krad	Clocked & long int	G200CI		
	Neutron	Californium source 2.15 MeV	ISIS	5.00 x 10^{9} neutrons/cm^{2}	Unbiased	N2.15	No	07/04/2018

7.2 Proton and Gamma Irradiation Comparison

7.2.1 Emission Time Constants

The trap pumping results of Chapter 5 showed the effects of proton beam energy on the traps produced and Chapter 6 showed the effects of gamma irradiations at different fluences. The two different particle types are now compared to study any variations between the multiple cascade/clustering protons and the *point defect* producing gamma irradiations.

It was found previously that the two proton irradiations (despite the difference in energy levels) have a near-identical emission time constant distribution for the double-acceptor silicon divacancy measurement regions. The same was found for gamma irradiations, with three devices that successfully trap pumped at 160.4 K measuring identical mode values for the emission time constant of the divacancy. Figure 7.1 shows the raw trap pumping measurements of both proton and gamma irradiated devices as overlaid emission time constant histograms at 160.4 K, where the mode of the major divacancy peak is equivalent for all irradiated devices at (1.37 ± 0.03) x 10^{-4} s and the relative scale of the number of traps is greater for the proton irradiations.

When comparing the impact of the two types of irradiation on the trap landscapes produced, two major features are important to note. Firstly, Figure 7.2 shows the X2 and X3 defects discovered in the control and gamma irradiated devices are not present in the proton irradiated devices. As the unirradiated CCD347-20 demonstrated the presence of the X2 defect and with no observation in the CCD47-20 this is further evidence the traps are classified as manufacturing defects. These traps present pre-irradiation have sporadically been observed in other internal trap pumping studies and highlight that other trap species than the major trap species (A-center, VV^{--}, VV^{-}, “Unknown” and E-center) can be distributed throughout the trap landscape, degrading the CTE and distorting possible correction models that use a unique assumed single energy level rather than the observed spread of energy levels. It is therefore recommended to characterise the initial trap landscape at and near the proposed operating temperature of the detector to find specific pixels that could be negatively

affected from CTI and to better understand the charge transfer behaviour of the system. Secondly, the extended ‘fast tail’ feature found in both proton-irradiated CCD47-20s is absent in the gamma irradiated CCD347-20s, which is made clearer in the normalised emission time constant histogram Figure 7.2 where the gamma irradiated devices maintain a sharp peak whereas the protons have both a broader spread of the major peak and show the additional ‘fast tail’ feature. The additional ‘fast tail’ feature is unlikely to be related to Poole-Frenkel barrier lowering as the emission time constant histograms of the gamma irradiated devices tested at equivalent clock voltages (and therefore similar electric field strengths) to the proton irradiations do not show the ‘fast tail’ features. The possible source for the spreading of the emission time constants (and therefore energy levels/cross sections) could be a result of the stress on the local lattice site, Poole-Frenkel barrier lowering or another effect, as each emission time constant has been shown to be repeatable and unique to an individual pixel.

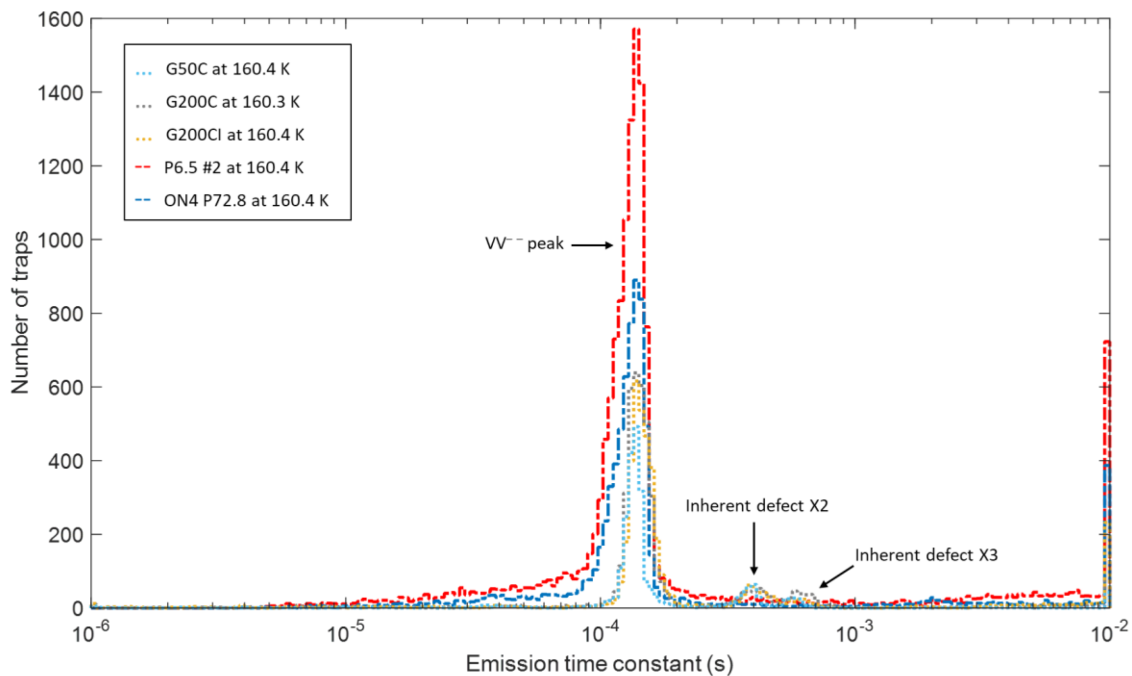

Figure 7.1: Emission time constant histograms for proton and gamma irradiations.

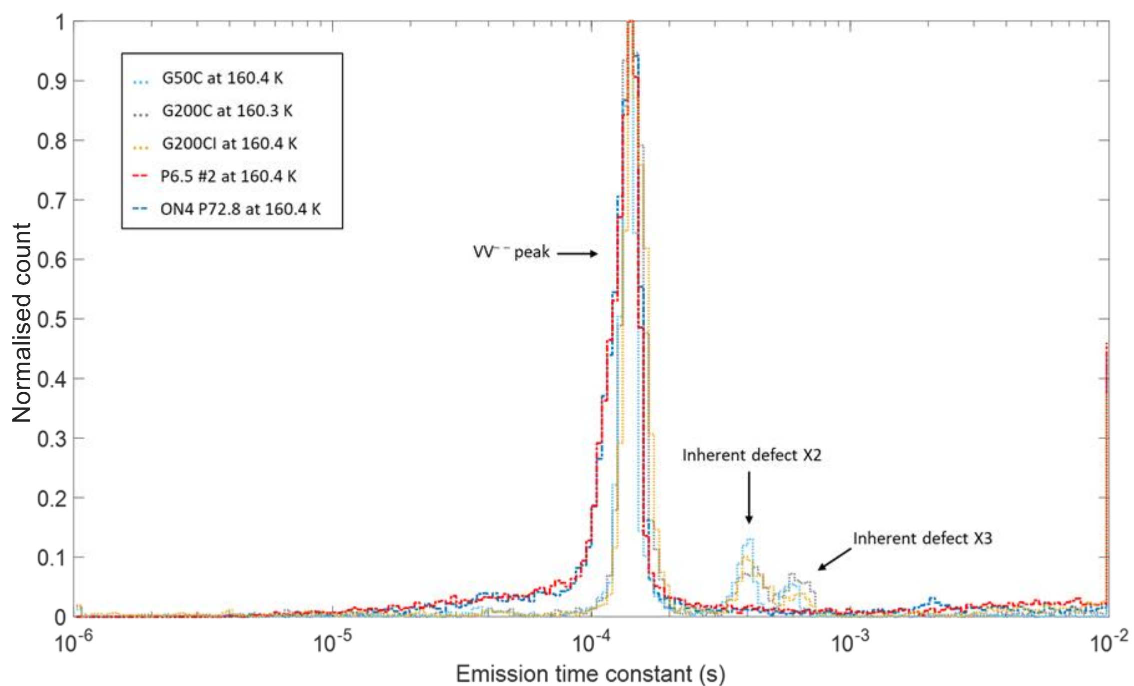

Figure 7.2: Normalised to emission time constant histogram for proton and gamma irradiations.

It is therefore shown here for the first time that the spread in the emission time constant and energy level is not only real but varies with particle type and therefore the specifics of the defect production mechanism. This provides crucial evidence that these effects must be included in all device trapping models, particularly the highly sensitive models used to correct radiation damage in images from space telescopes such as for the Euclid VIS instrument. Evidence is also provided that an element of the spreading, but not all, may be due to lattice structural damage.

However, to confirm that this is the case we can probe further through the use of neutron and electron irradiations. For a neutron irradiated device we would expect not only a significant increase in the production of clusters of traps, but also increased lattice structural damage around trapping sites. Therefore, through examining single traps within a neutron irradiated device, following the hypothesis that some element of the spreading is due to structural damage, one would expect that a neutron irradiated device would show a larger spread and a possible larger, more prominent 'fast tail' feature for the divacancy peak.

7.2.2 Energy Level and Cross Section Measurements First Method

The energy level and effective cross section measurements of defects in silicon-based detectors are essential to the understanding the individual defect types and attempt to correct the damage. The measurements are taken by finding the emission time constant extracted from each dipole (with a complete resonance curve), which is tracked with temperature change and fitted using the SRH Equation 4.2 with a least squares fitting method. A strict goodness of fit is necessary which is chosen at R-value threshold of 0.995 as small variations can greatly skew the measurements. The measurements of the energy level and cross sections are shown in Figure 7.3 for the proton and gamma irradiations. Regions with a high density of traps are highlighted and demonstrate the energy levels and cross sections associated with the mode locations of the previously shown emission time constant histograms. The large diagonal spread is a fitting error that is difficult to mitigate because of the degeneracy of the terms.

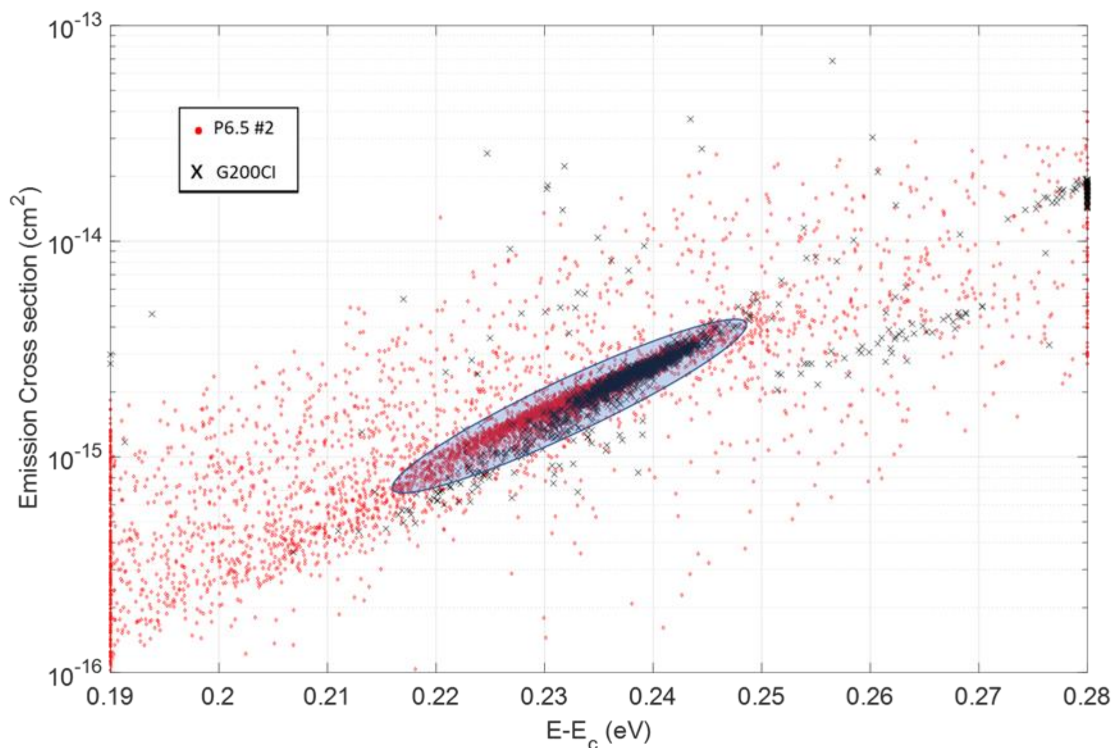

Figure 7.3: Fitted energy levels and cross sections for individual traps found in the proton irradiated P6.5 #2 (red dots) compared with the gamma irradiated G200CI. The highlighted region indicates the estimated location of the VV^- defect.

To better pinpoint the divacancy energy levels, the effective cross section is fixed to an assumed value of 5 x 10^{-16} cm^2 (1,2) which falls in the range of literature values found by (3,4) that have been measured using separate measurement techniques (results range from 10^{-16} to 10^{-15} cm^{-2}). The calculation of the energy level for the proton and gamma irradiations are overlaid in Figure 7.4 and normalised to demonstrate the change in shapes and spread of the major peaks with particle type and fluence. The threshold R-value is set to 0.995 to omit all poor fits that could distort the distribution.

The key difference between the two particle types include the broadness of peaks, where the proton irradiated devices (similar to the emission time constant measurements in section 7.2.1) demonstrate a 'fast tail' feature and shoulder peaks not seen in the gamma irradiations. A normal distribution is expected in the event of fitting noise however as shown in Table 7.2 there is a large negative skewness of each major divacancy peak which further indicates an effect such as Poole-Frenkel barrier lowering or lattice strain is reducing the energy level of many proton events, possibly from the sub-cascade/clustering component that is not found in gamma irradiated devices. The mode values are consistent between particle types showing the defect studied is consistent. The spreading of the energy levels is measured using the full width half maximum (FWHM) where it is found the 200 krad gamma irradiations are consistent with each other and ≈75% broader than the 50 krad device signalling the irradiating dose can contribute to the energy level spreading. The proton irradiations have broadest FWHM and a 'fast tail' feature that is not present in gamma irradiated devices. Normalising the energy levels and comparing the two particle types for each defect has resulted in the identification of the divacancy, the consistent observation of a negatively skewed distribution across all devices and finding the energy spreading effect is larger in proton irradiations and the gamma dose contributing to the energy level spread.

Table 7.2: Mode energy level, full width half maximum (FWHM) and skewness measurements for the VV^{--} peaks for proton and gamma irradiated devices.

Device	Mode energy level ± 0.0005 (eV)	FWHM (10^{-3} eV)	Skewness
G50	0.227	2.1	2.62
G200C	0.225	2.9	2.18
G200CI	0.226	2.8	2.23
P6.5 #2	0.226	3.3	1.82
P72.8	0.226	3.2	1.90

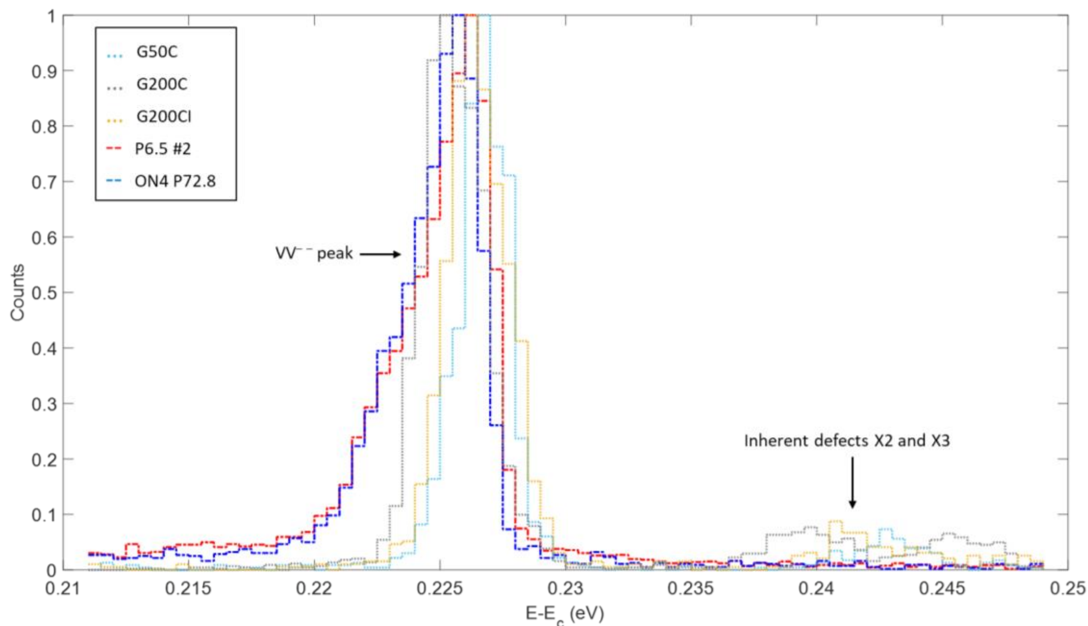

Figure 7.4: Normalised energy level comparison of the proton and gamma irradiated CCDs for the divacancy and the X2 and X3 defects at a fixed cross section of 5 x 10^{-16} cm^{-2}.

7.2.3 Energy Land Cross Section Measurements Second Method

The energy level measurement method used to this point have compared the emission time constants across multiple temperatures for each pixel at a fixed cross section in agreement with the literature values. The mode values of the emission time constant histograms for the divacancy peak represents the most probable emission time constant to be discovered in the detector. Regardless of if this is the true energy level of the divacancy or if it is a result of energy bending mechanisms, it is the energy level most likely to be found in the device during operation and should be characterised. Results in section 7.2.1 have shown the emission time constant mode value to be consistent at a fixed

temperature regardless of the fluence or the particle type and therefore every successfully trap pumped frame at each temperature can be used to measure the most probable divacancy energy level and cross section.

The mode peak locations of 73 different divacancy measurements for all combined proton and gamma irradiated histograms create a single dataset to calculate the energy level and cross section of the divacancy which is demonstrated in Figure 7.5 and fitted by using a non-linear least squares method with the SRH fitting equation 4.2. The energy level of the double acceptor silicon divacancy is calculated at 0.239 ± 0.0005 eV with a cross section of 1.29×10^{-15} cm^{-2} and the goodness of fit is 0.991, in excellent agreement with the experimental data. The new energy level of 0.24 eV for the divacancy has backing in the literature as while the majority of DLTS studies have measured the energy level of the double acceptor silicon divacancy at 0.23 eV, the Laplace DLTS method is known to have an order of magnitude increase in energy resolution (5) and finds divacancy energy level at 0.24 eV in both (6,7).

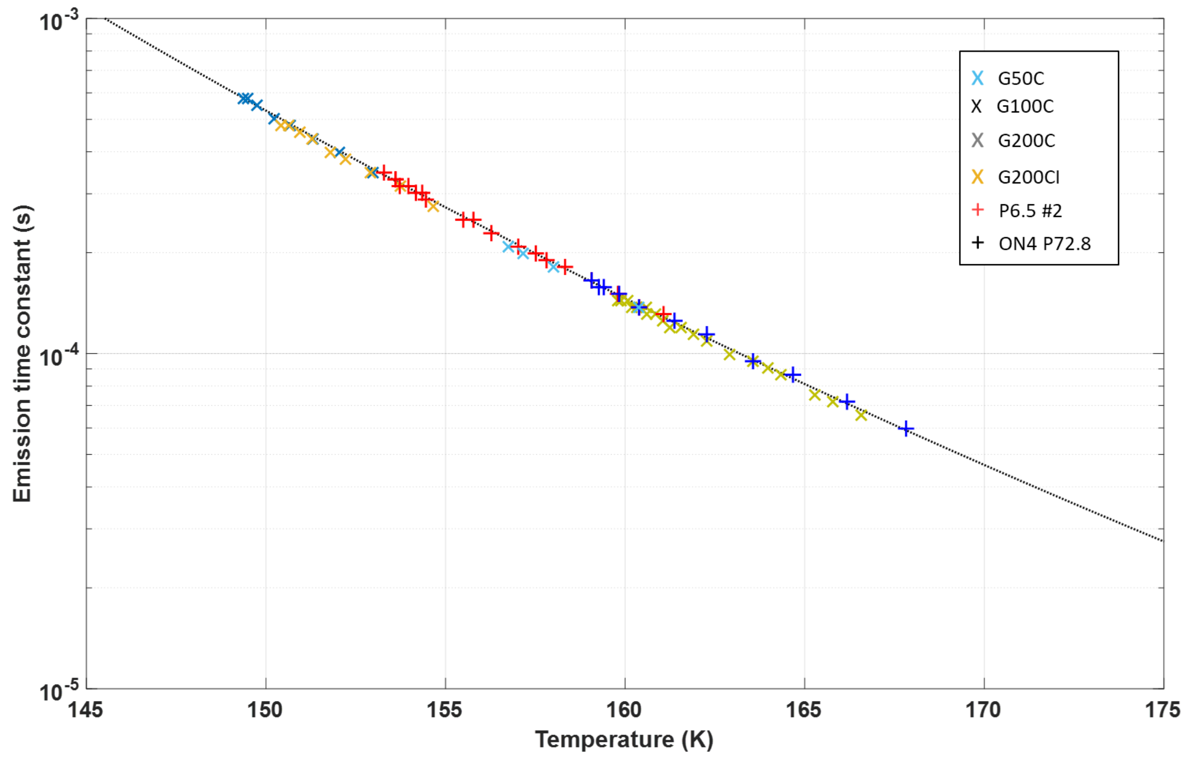

Figure 7.5: Emission time constant histogram mode location for the silicon divacancy peak for every trap pumped device at each temperature trap pumped.

7.3 Neutron irradiation comparison

To better understand the difference between *point* defects and *clustering* impact on the trap landscapes a CCD347-20 was irradiated with a californium-252 (Cf-252) neutron source which produces the most probable energy of 0.7 MeV and a mean energy of 2.15 MeV neutrons capable of producing *clusters* of defects in silicon and causing significant lattice structural damage. The device is part of the batch used for the gamma irradiations which should provide a good comparison on the extremes of each damage type and highlight any energy level spreading previously seen in the proton gamma comparisons. Additionally, a single CCD47-20 was irradiated with an electron beam at 1 MeV which is known to create *point* defects in silicon which is an ideal comparison particle type to higher energy protons and neutrons.

7.3.1 Traps produced by neutron irradiations

A single CCD347-20 device was irradiated at the National Physical Laboratory (NPL) in London, with a californium-252 neutron source producing an average neutron energy of 2.15 MeV. The device was irradiated to a 10 MeV equivalent proton fluence of 5 x 10^9 neutrons/cm^2. Trap pumping the neutron irradiated CCD347-20, the trap landscape shown in Figure 7.6 has similar trap statistics to the control device rather than the gamma and proton trap landscapes as a result of the fluence chosen being too low, though still advantageous for comparison to the control and electron irradiated devices, and the dipole fitting success from cluster defects. The key features of the emission time constant histogram include the divacancy mode count increasing by a factor of three relative to the control device while the divacancy peak is found to be relatively broad, extending from the divacancy mode to the X1 defect, the manufacturing defect X1 shows no sign of a trap count increase and the manufacturing defect X2 shows an increase relative to the control device, which has not been observed as drastically in any other device. Figure 7.7 shows the normalised comparison of the control device with the neutron irradiated device. A broadening of the divacancy peak is observed similar to the previous proton irradiations while neither the X1 or X2 defects show any indications of a broadening effect,

even with a substantial increase in counts for the X2 peak. This suggests the spreading feature observed in proton and neutron irradiations in unique to the divacancy however the small total trap counts in the neutron irradiated device warrant further investigations.

Table 7.3 shows the neutron X2 count is greater than any other CCD347-20 while the divacancy count is less than other devices which is the opposite to the ratios found for the other particle types where the divacancy dominates non-neutron irradiated trap landscapes.

Examples from neutron irradiated DLTS studies such as (8) finds the silicon divacancy is measured at 0.23 eV with a trap concentration of 0.54 ± 0.15 (10^{10} cm^{-3}) and a neighbouring defect is found with a measured energy level of 0.26 eV and a trap concentration of 2.20 ± 1.04 (10^{10} cm^{-3}) the neighbouring trap has a greater trap concentration even at greater fluence levels and a 5.3 MeV beamline energy. This would imply similarities between DLTS measurements and trap pumping results for the neutron irradiations, with both showing an increase in a defect found at 0.26 eV to 0.27 eV (which is calculated later in Figure 7.13) with a greater population than the divacancy. Defects such as the trivacancy and larger vacancy groupings have been considered however the energy levels do not agree with the 0.26-0.27 eV energy level suspected to be the X2 defect. It is possible the B_iO_i defect previously identified as X2 is present in N2.15 but an additional defect is contributing to the increased X2 peak count as the neutron irradiation introduces a different trap species that is dependent on the vacancy productions.

Table 7.3: CCD347-20 divacancy, X2 and X3 trap count with dose and damage species at ≈160.4 K.

Device	Divacancy count	X2 Count	X3 Count
Control	69	223	-
G50	1872	279	119
G200C	3410	313	291
G200CI	3130	350	125
N2.15	429	552	-
E1 (CCD47-20)	700	60	-

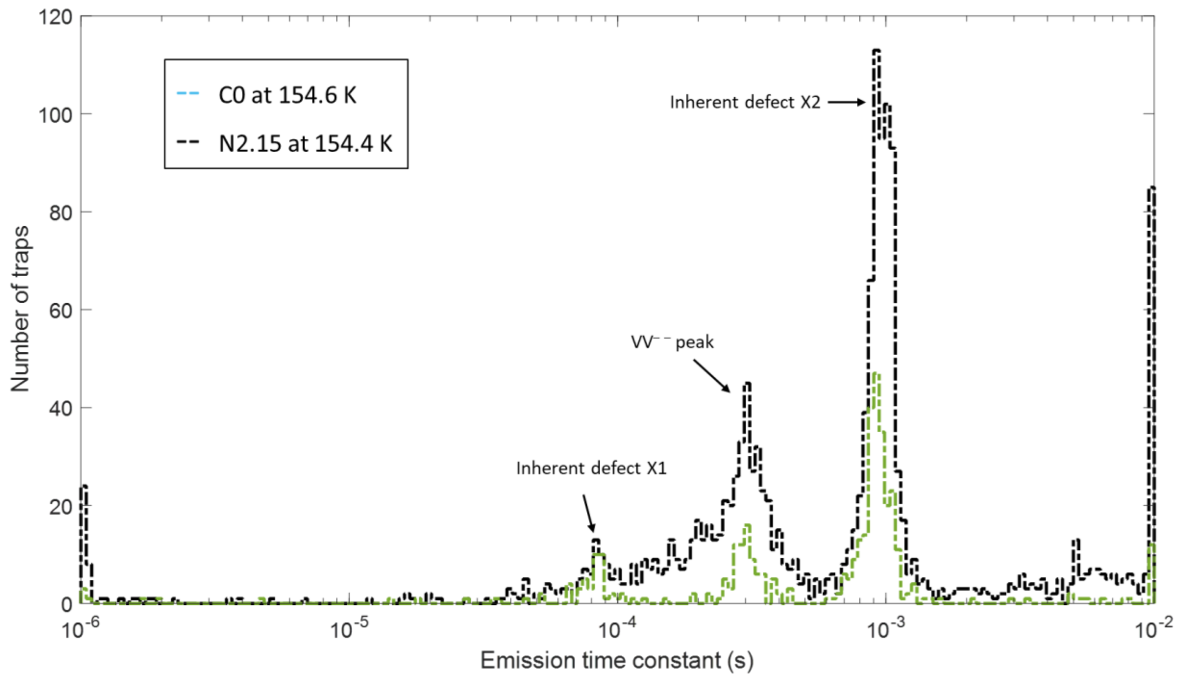

Figure 7.6: Emission time constant histogram of the control and neutron irradiated CCD347-20s at ≈154 K. X1 and X2 are the temporary names for the inherent defects that are currently undefined.

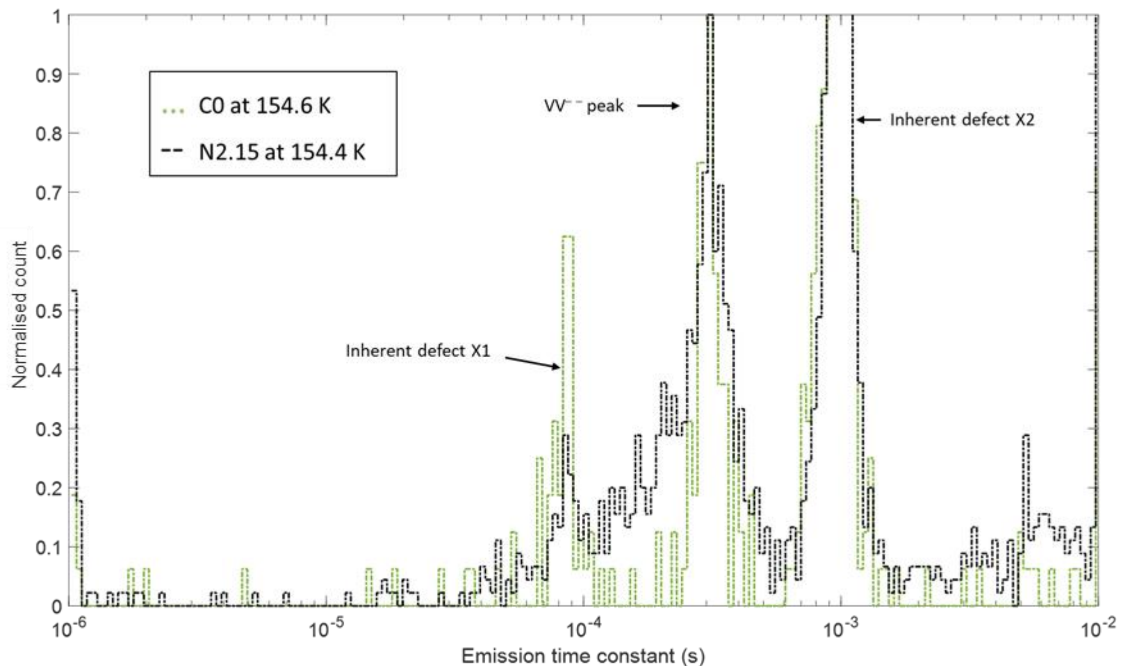

Figure 7.7: Normalised emission time constant histogram comparing neutron irradiated N2.15 device to the control device C0. Min-max normalisation is scaled to the divacancy mode value.

The neutron irradiated device is compared with the gamma irradiated G200C in Figure 7.8 and shows an increase in the manufacturing defect X2 is found while there is no presence of the X3 defect. It

further highlights the X3 defect is independent of the X2 defect demonstrating the manufacturing defects are made of at least two different defect species. The divacancy peak is broad for the count and if normalised would greatly exceed the peak width of the G200C peak however as the trap statistics are low it is suggested that this should be explored again in the future at a higher fluence to confirm if the increase in the X2 peak continues and if the broadness of the divacancy peak scales to the same distribution. When normalised to the divacancy peak as shown in Figure 7.9, the divacancy peak again broadens significantly. The increase in defects in the faster emission time constant range indicates an additional defect is formed in neutron irradiations that is otherwise absent from gamma irradiations. Future trap pumping studies will attempt to measure and identify these emerging traps.

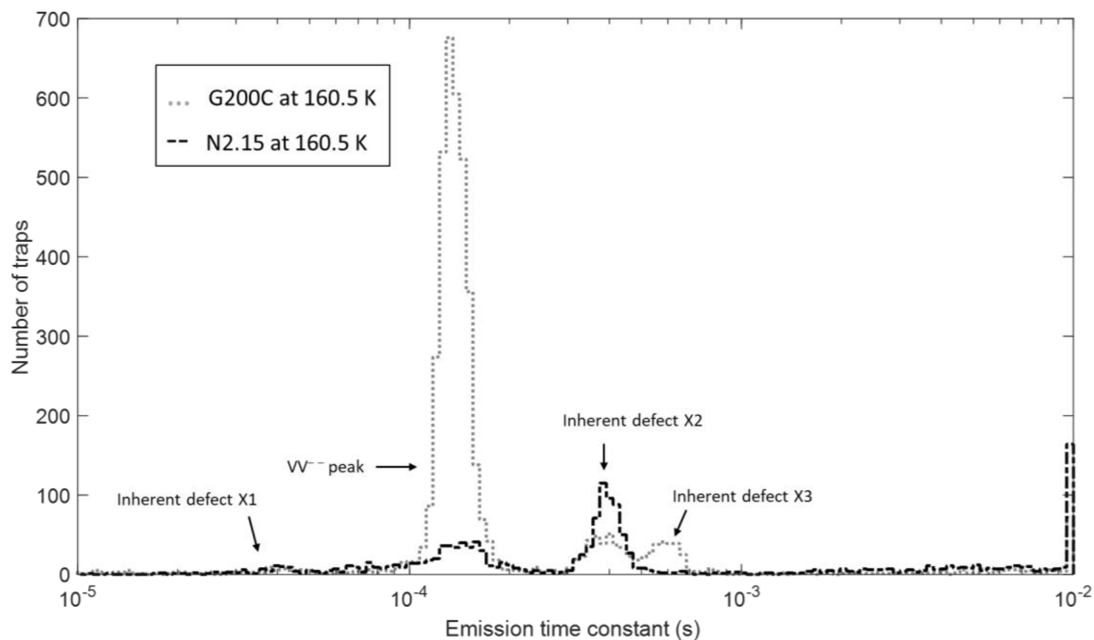

Figure 7.8: Comparison of the trap landscapes for the N2.15 neutron irradiated device and the gamma irradiated G200C. Both devices are CCD347-20s and both X2 and X3 peaks are present.

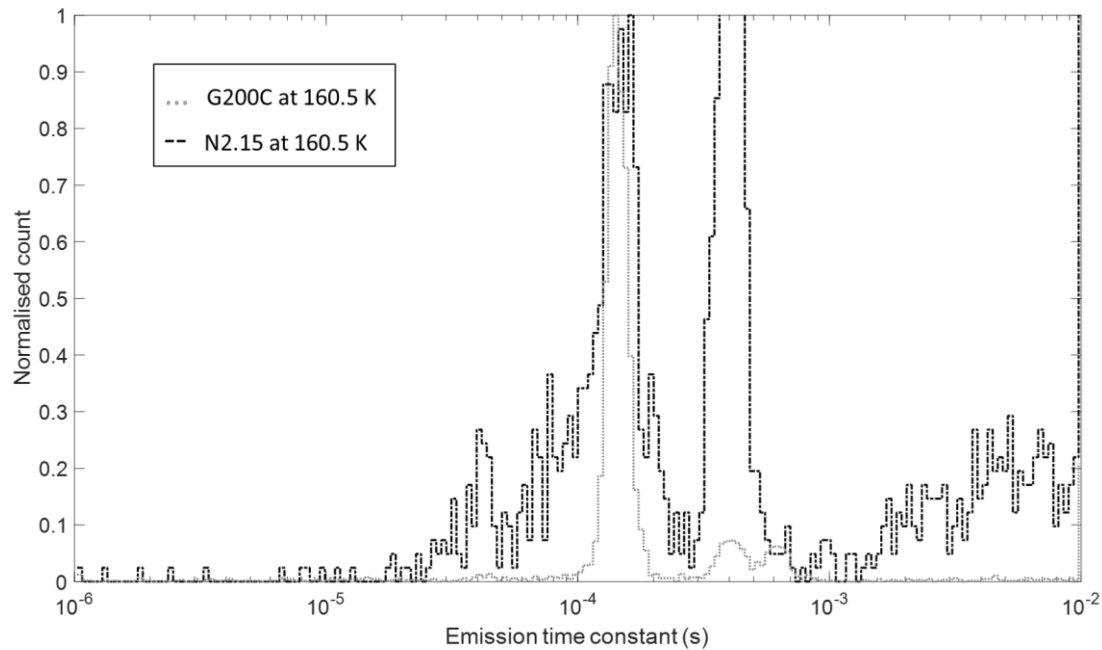

Figure 7.9: Normalised trap landscape to the divacancy peak for comparison of N2.15 to G200C. Min-max normalisation is scaled to the divacancy mode value.

7.3.2 Electron irradiation experimental setup

To confirm the observed feature differences between the neutron clustering source and *point defect* sources, a low fluence 1 MeV electron irradiated device is trap pumped. A single CCD47-20 was irradiated with a 1 MeV electron beam to a dose of 10 krad at the ONERA electron Van de Graaff accelerator in GEODUR facility (Toulouse, France) in April 2016 by Phillipa Smith as part of a joint CEI/ONERA study. The fluence is small relative to the lowest fluence gamma irradiated device (G50) at 10 Gy where the trap pumping results are compared to the neutron irradiated device in Figure 7.10 where both devices maintained a stable trap pumping temperature at 157.6 K.

7.3.3 Comparison of the neutron and electron trap landscapes

The trap pumping results of the electron irradiated device E1 shows the X1 peak fails to be measured on the on the CCD47-20 while the X2 peak is present on both the control and the neutron irradiated CCD347-20. This implies X2 is a manufacturing defect for both device batches while X1 is specific to the CCD347-20s manufacturing process or to the specific batch. The divacancy peak greatly exceeding

the X2 peak count agrees with all non-neutron irradiated devices, emphasising the clustering dominated neutron irradiations are unique to the trap landscape.

The edge of the divacancy count for E1 (at $\approx 10^{-4}$ s) drops off sharply, whereas in device N2.15 we find multiple traps in a region otherwise unoccupied in both the control device and E1, further demonstrating that traps in the neutron irradiated device experienced an energy level lowering. A continuum of traps is found between the X2 peak and the edge of the detection region for the neutron irradiated device with a significant count of neighbouring (slower emission time constant) defects relative to the point defect E1 device. For the trap pumping results for the proton irradiations previously shown in Figure 7.1 the peak count of the partial resonance curves at the edge of the probing region (10^{-2} s) was approximately half the maximum peak count whereas the neutron irradiations find the count comparable to the peak count of X2 which shows a different ratio of trap species is forming for proton and neutron irradiations.

When normalising to the divacancy mode location as shown in Figure 7.11, the X1 and X2 peaks are observed in the CCD47-20 device at a low count that is otherwise obscured by the ‘fast tail’ features of the proton irradiations. The main divacancy peak is similar but has a clearly defined cut off at 1.2×10^{-4} s for the 1 MeV electron irradiated device which is known to only produce point defects whereas the neutron irradiated device, even with a smaller total trap count clearly demonstrates the ‘fast tail’ feature is missing from the electron irradiation.

The spread in the peak is present for all irradiation types (proton, gamma, electron and neutron). The spread in the peak width for the divacancy emission time constant in the gamma irradiated devices is lowest, for which only *point* defects are expected, demonstrating that the mechanism is not simply the surrounding lattice damage. However, this surrounding lattice damage may be the broadening factor for the proton and neutron irradiations for which the spread increases. The neutron irradiation has the greatest spread and most prominent “tail” relative to the number of traps found, giving further

backing to this hypothesis, i.e. that some element of the spreading is caused by lattice structure damage near trap sites.

We are however limited in measurement for the neutron irradiations due to the predominance of clusters, such that many devices would be required to increase our statistics on singularly measurable defects. There are only a limited number of pixels in a device, and a large proportion of the defects created under neutron irradiation result in clusters, such that the number of single pixel defects that we can measure as separable from clusters is severely limited per device.

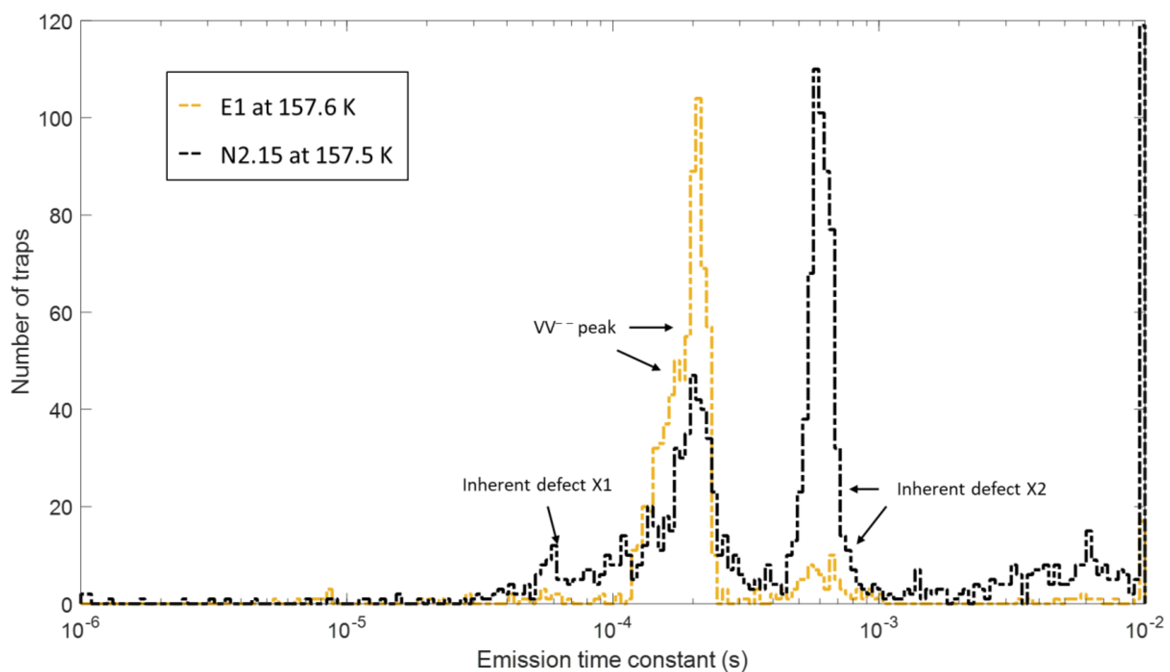

Figure 7.10: Emission time constant histogram of the electron and neutron irradiated CCD347-20s.

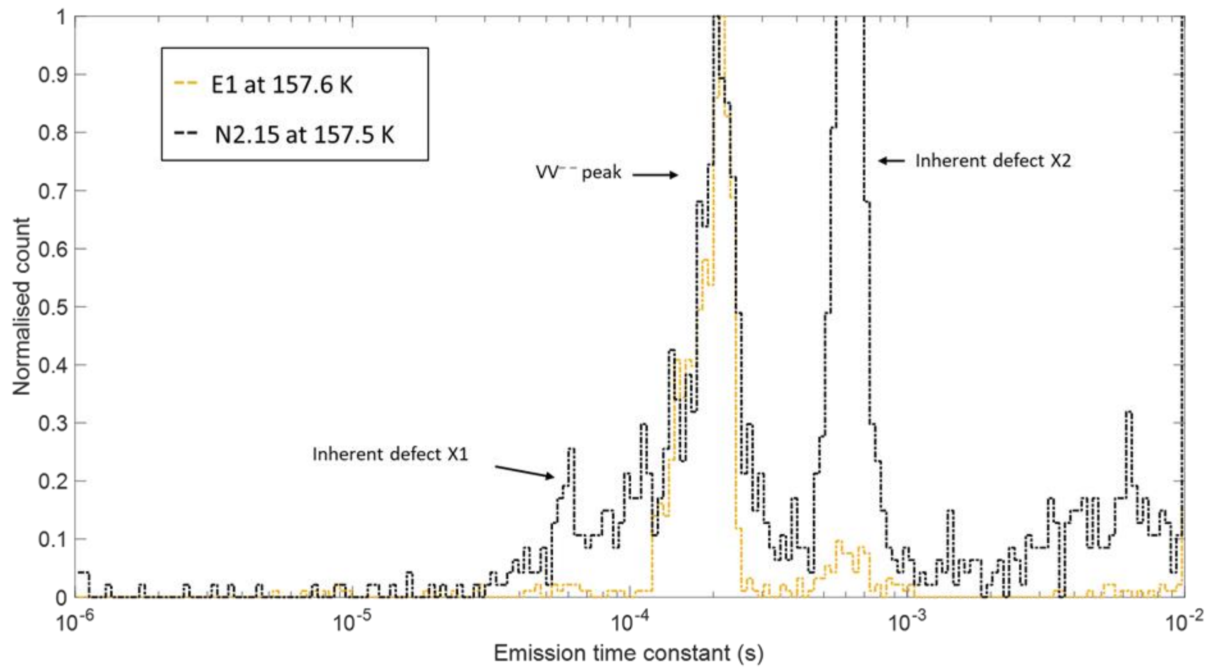

Figure 7.11: Normalised trap landscape to the divacancy peak for comparison of 1 MeV electron irradiated device E1 to neutron irradiated device N2.15.

7.3.4 Comparison of neutron and proton irradiations

The neutron irradiated device N2.15 is compared with the proton irradiated device P6.5 #2 in Figure 7.12 and shows an increase in the broadness of the normalised divacancy peak for the neutron irradiation. This spread is tentative as the number of defects present in the neutron irradiation is significantly lower than the proton irradiation which can be observed by the X1 peak that is identical to the pre-irradiation device. The defects forming in between the X1 peak and the divacancy peak is not observed in the gamma or electron irradiations, even with a larger number of pixels identifying traps. This heavily implies an underlying difference between protons (between 6.5 MeV and 72.8 MeV) and 2.15 MeV neutron irradiations with 1 MeV electron and ^{60}Co gamma irradiations, with the commonality being the displacement damage mechanisms either causing point defects or subcascades/clusters of defects from interactions with the silicon.

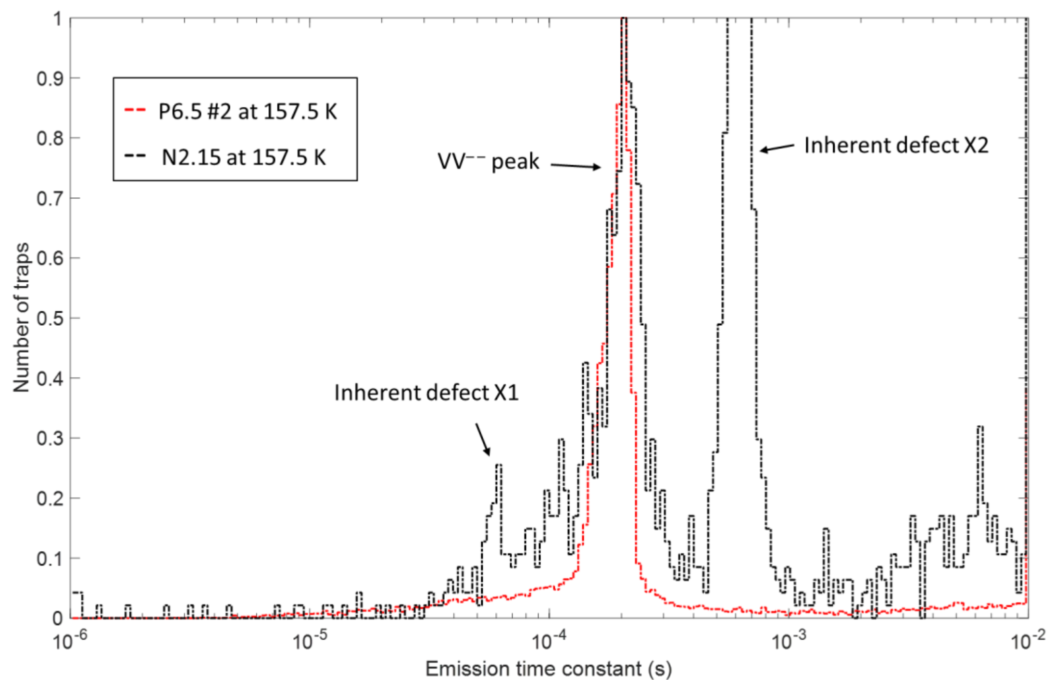

Figure 7.12: Normalised trap landscape to the divacancy peak for comparison of N2.15 to P6.5 #2 at 157.5 K. Min-max normalisation is scaled to the divacancy mode value.

7.3.5 Energy level of the X2 peak

The X2 peak has been observed to increase in count significantly for the neutron irradiated device relative to any other device tested. To try to measure the energy level specific to this unidentified defect the same method used in Figure 7.5 is applied here. Finding the mode location of the neutron irradiated device was found at the location of the X2 peak and as many trap pumping sweeps were taken for the neutron irradiated device the peak is studied using the same method. The energy level of the X2 peak is found at 0.269 eV and the cross section at 3.18 x 10^{-15} cm^{-2}, Figure 7.13. The X2 defect follows traditional trap dynamics, changing emission time constant with temperature but does not appear to be irradiation induced from any particle type. The energy level is tentatively attributed to the B_iO_i defect found by (9) which is also quoted at an energy level of E_c - 0.27 eV. The defect in Mooney was discovered following electron irradiation and correlated to the boron concentration, annealing out at 443 K which exceeds the maximum temperature a CCD is capable without sustaining damage. Repeat measurements pre- and post-irradiation would be the best solution to find if the X2 defect is a radiation induced defect from neutron irradiations. As the X2 defect is present in all

CCD347-20 devices and measurable in a single CCD47-20 so it is assumed to be a defect that is consistent to the manufacturing process and appears to fluctuate in count between wafers. The discovery of the X2 peak being consistent throughout the majority of irradiated devices, the occasional presence of the X3 defect and the spreading of the emission time constants for all detected traps definitively shows that as the scientific requirements of space missions become ever more demanding the characterisation of the defects must be performed in flight devices and while in-orbit to correct the damage.

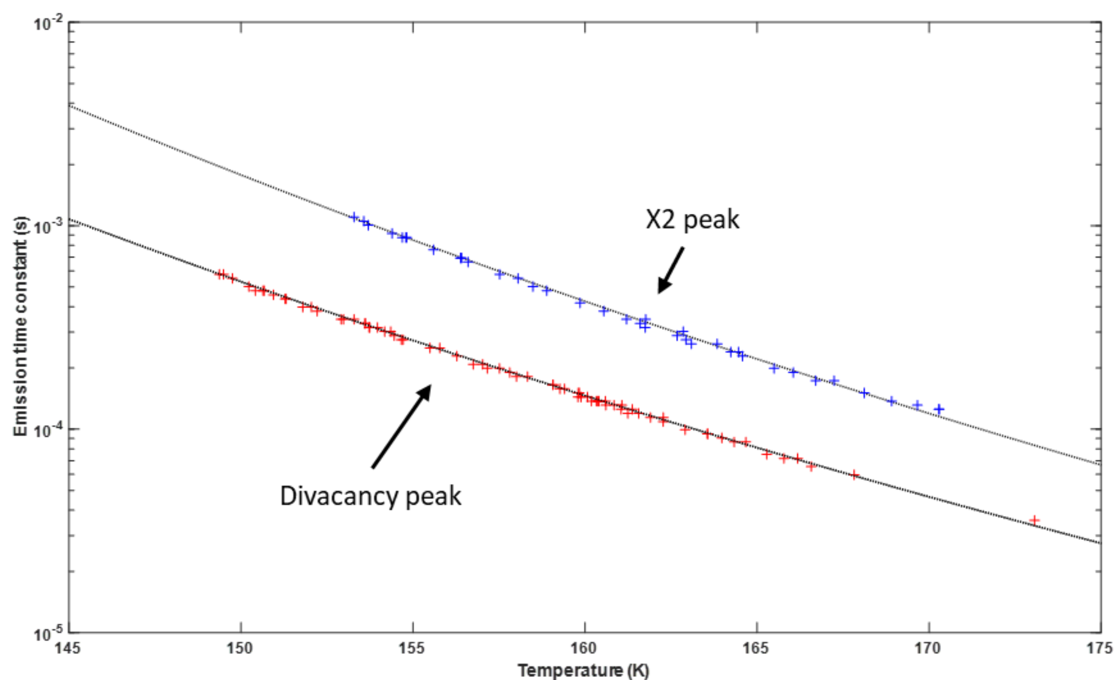

Figure 7.13: Peak locations from the emission time constant histograms of each device. The X2 defect peak is found in the neutron irradiated CCD347-20 and is compared to the divacancy peak from all irradiated devices, first shown in Figure 7.5.

7.4 NIEL Scaling Discussion

This study uses the Screened Relativistic (SR) Nuclear and Electronic Stopping Power Calculator for NIEL scaling. With this method, the 10 MeV equivalent dose is calculated for P6.5 #2 at 8.32 x 10^9 protons/cm^2 and P72.8 at 9.87 x 10^9 protons/cm^2. The damage ratio is a factor ≈1.2 larger for P72.8 however the number of divacancies is a factor ≈0.6 smaller for the divacancy peak count when both devices are trap pumped at 160.4K. The discrepancy is even more striking for gamma irradiated devices where, as shown previously in Figure 6.2, the G50 device has a lower dose by a factor of four

compared to G200 or G200CI and the number of traps is only halved. This is despite the fact that they were both irradiated simultaneously in identical conditions with a stable gamma source. In the last year of measurements there has been no appreciable changes in the divacancy peak counts or pixel locations that would indicate any signs of annealing effecting the defect landscape. If in any way the dose was compromised, the key results of this study remain accurate as the energy levels, peak locations and spreading of emission time constant peaks remained consistent for particle type and energy.

7.5 "RPS Defects"

While successful fitting to the resonance curves is essential to the understanding of defects and the methods to mitigate the damage, the dipoles that fail to fit to the resonance curves are of interest as charge continues to be captured and the behaviour of these traps is even less well understood. The initial study of the irradiated devices used a TEC cooler and was operated at 248 K which is capable of measuring the unknown defect which is estimated to be found at 0.30 eV to 0.34 eV but it is inconsistently observed in irradiated devices. While trap pumping at these warmer temperatures an observation was made that some resonance curves suddenly and substantially increased or decreased in intensity between two frames as shown in Figure 7.14. Here a dipole appears at one pumping phase time and then suddenly disappears while the neighbouring regular pixels and dipoles maintain the same orientation and intensity as the previous frame, even for a very small change in clocking timings between images. The phenomenon is similar to the multilevel Random Telegraph Signal (RTS) pixels that have previously been studied in the dark current profiles of CCDs and CMOS devices following displacement damage. These studies have shown metastable bulk generation centres with discrete switching amplitudes in dark current measurements. Through manual analysis of the resonance curves, a pattern emerged of certain traps exhibiting RTS-like intensity shifts through the probed regions for a selection of traps. The newly discovered traps are referred to hereon as "Random Pumping Signal" (RPS) traps and are found to flip between different pumping efficiencies, much like

the RTS pixels dark signal levels. These traps are found to directly interact with the charge packet and are present in the buried channel.

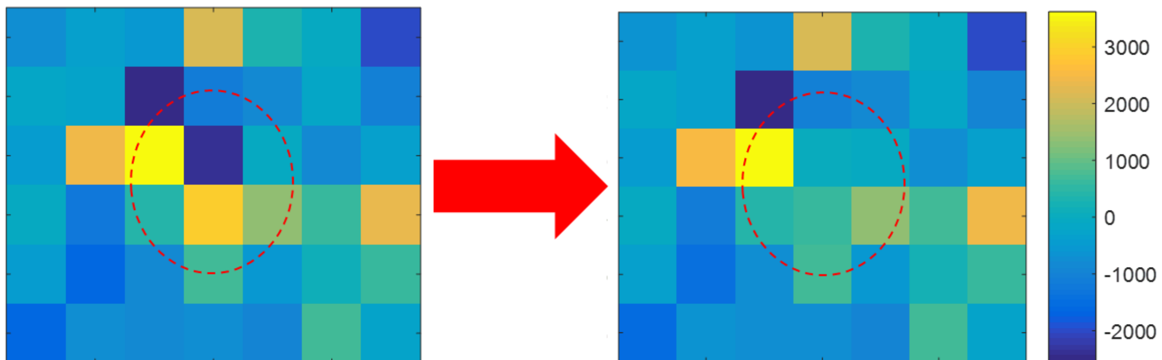

Figure 7.14: Dipole sudden intensity shift found in a background corrected frame where the neighbouring pixels remain at a consistent intensity and dipole orientation. The two frames have a 1 µs difference in pumping phase time.

Examples of the RPS effect on a trap's resonance curve are shown in Figure 7.15 and Figure 7.16 where the intensity, much like a dark signal RTS defect, appears to shift between two levels. On average the gamma irradiated devices showed 700 of ≈5000 traps (15%) exhibited RPS shifts whereas the neutron irradiated device showed only 44 of ≈6000 traps (0.7%) exhibited RPS shifts. As both gamma and neutron devices are CCD347-20s from the same batch the RPS phenomena is a radiation induced property. One should also note that each data point on the *x*-axis in Figure 7.15 and Figure 7.16 is a measurement from a new image, therefore the *x*-axis can be considered as a progression in time, with the sequencing taking successive images in order.

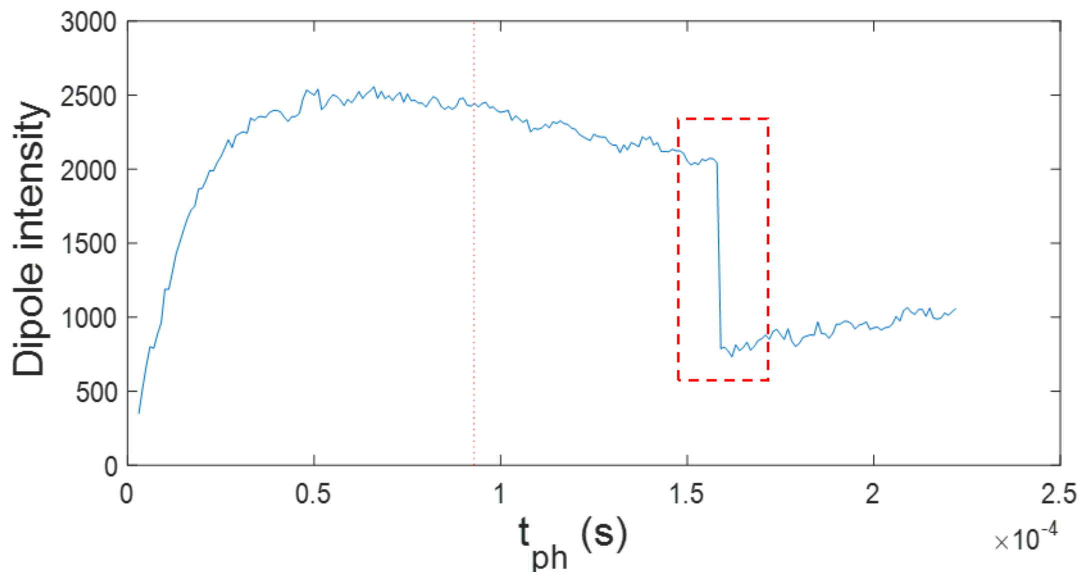

Figure 7.15: Resonance curve profile of a dipole with an RPS shift with a single sharp drop in intensity

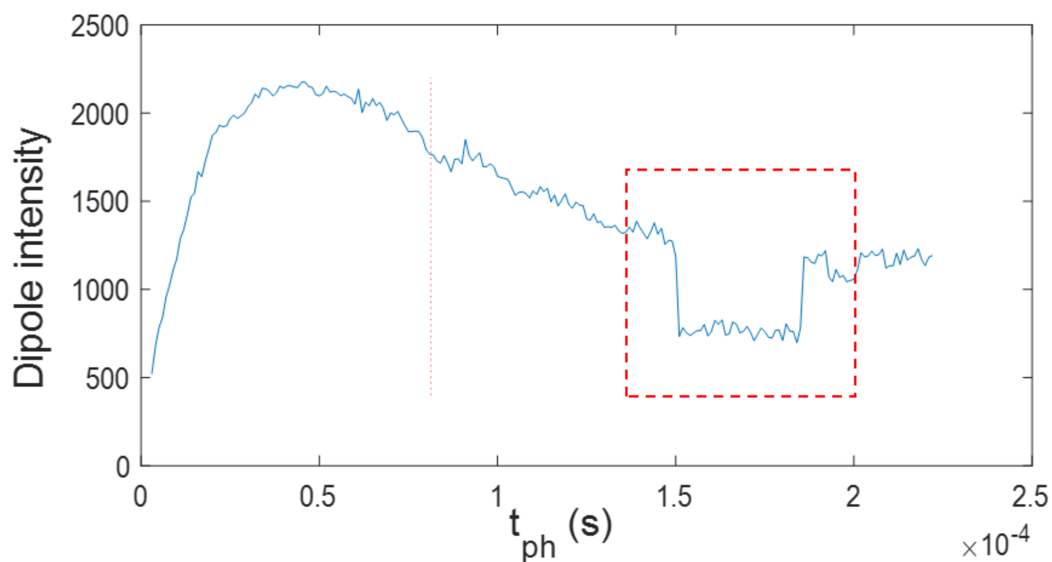

Figure 7.16: Resonance curve with a sudden intensity shift that sharply returns to the projected intensity level.

A comparison of the RPS defects between N2.15 and G200C are shown in Figure 7.17, where in the gamma irradiated device we find an evenly spread distribution of RPS shifts across the multiple pumping phase times are used. This shows the effect is most likely random (or dependent on a time constant) and independent of pumping phase time. The intensity shifts are roughly mirrored around zero for the intensity change which signifies both dipole pixels shift simultaneously, and they are pumping signal from one another as opposed to a false positive hot pixel neighbouring a cold pixel.

Finally, the trend indicates that two RPS shifts are the most common occurrence for the resonance curves of an RPS pixel similar to Figure 7.16.

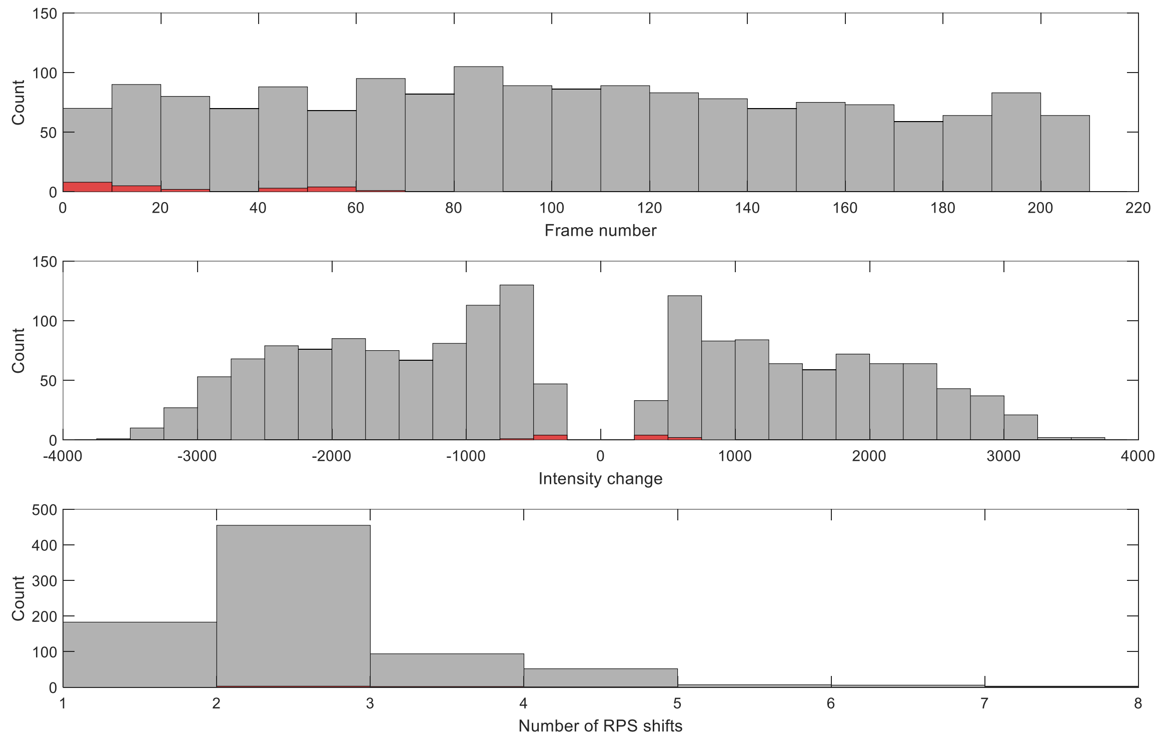

Figure 7.17: RPS statistics at 246K for N2.15 (red) and G200C (grey) showing the frame number (which are spaced logarithmically from 10^{-6} to 10^{-2}) with the occurrence of the RPS event (top), the number of traps and the intensity change of each jump (middle) and the number of RPS shifts found across all frames for each RPS trap (bottom).

The search is repeated at colder temperatures using the Stirling cooler at 160.4 K. The intensity profile of an cryogenic RPS dipole is shown in Figure 7.18. This data was taken from one thousand frames with uniformly spaced tphs to track the rate of significant RPS shifts. Each data point is representative of a single frame with identical operating conditions while only changing the pumping phase time and the surrounding pixels show no significant changes frame to frame. The possible resonance curve is illustrated on the figure, with a maximum pumping amplitude in-line with the maximum pumping probability of $P_C \approx 0.25$ expected for a single electron trap. The intensity periods where the trap flips from electrically active to inactive demonstrate the RTS-like nature of the trap and it does so at random periods (i.e. within the limited data available no time constant can be calculated).

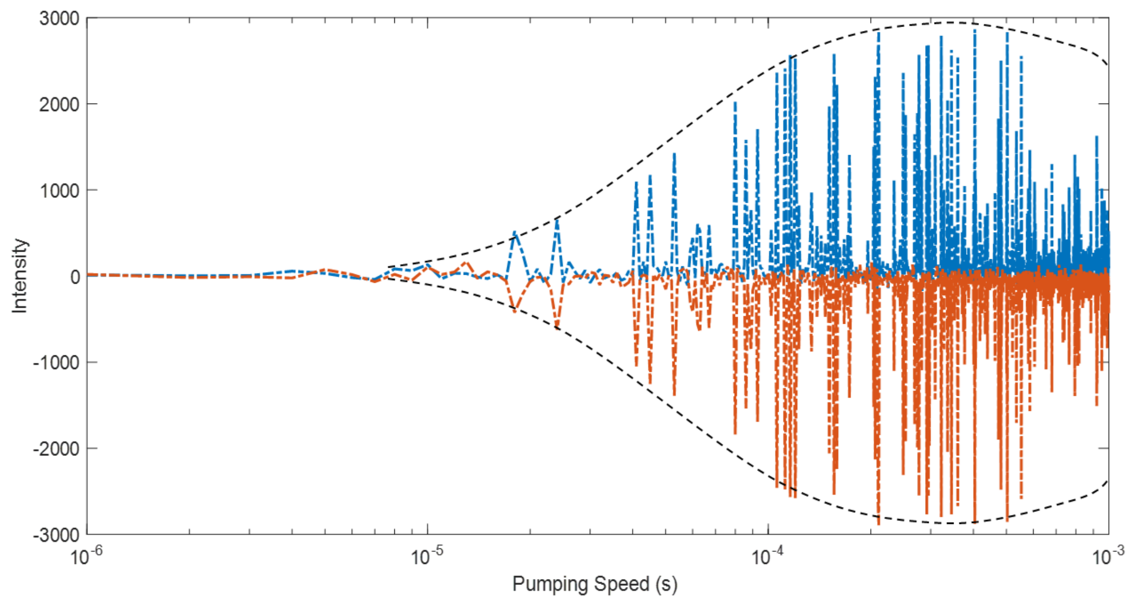

Figure 7.18: Example of an RPS trap from the G200C device at 165.0 K that is swapping randomly between background intensities and the resonance curve profile of a trap. The implied resonance curve is overlaid on the figure with the dotted line.

Table 7.4 shows the number of RPS defects that were found in the trap pumped devices at 160.4 K. The proportion is larger in the gamma irradiated devices relative to other particle types and the number of traps demonstrating RPS shifts in significantly less at 160.4 K compared to 246.0 K for all particle types indicating the RPS effect is dependent on thermal energy to swap states or is a property associated with the unknown defect. The proportion of RPS traps is again greater in the gamma irradiated devices relative to other particle types and the number of traps demonstrating RPS shifts in significantly reduced at 160.4 K compared to 246.0 K for all particle types. The RPS effect is shown to be dependent on thermal energy to swap states and it is possible that this is a property associated with the unknown defect. Work by (10) found Random *Telegraph* Signals defect fluctuations are observed at temperatures as low as 183 K while this study runs colder by ≈20 K and finds multilevel shifting still exists for individual traps in the detector and that these RTS defects scale well with displacement damage dose (DDD). The number of Random *Pumping* Signal defects does not find the same scaling relationship to DDD as RTS defects, with the type of radiation damage appearing to be a key factor as the proton irradiations have shown both a greater DDD and a greater number of traps yet a lower RPS trap count to the gamma irradiations.

Table 7.4: Number of dipoles found with RPS defect at 160.4 K.

Device	Dipole count	RPS defect count	RPS/dipole (%)
G50	3185	72	2.26
G200C	8737	168	1.92
G200CI	8338	185	2.22
N2.15	2839	2	0.07
P6.5 #2	18260	92	0.50
P72.8	10284	24	0.23

The same is true for dark current and RPS defects where in typical RTS studies a linear dependence is found between the dark current and RTS probability (11) as found in other areas of the study not detailed within this thesis. The multilevel RPS traps found in the gamma irradiated device appear to create a larger number of RPS defects than proton irradiations despite a reduced damage to the lattice, fewer vacancies produced on average and a lower dark signal. It appears that *point* defects from gamma irradiations introduce RPS traps at a higher rate than proton irradiations and neutron irradiations where the dark signals are both larger and clustering defects and subcascades are expected to dominate the interactions. Future attempts to probe the RPS defects will first characterise defect pre and post irradiation to find an accurate change which are merely assumed to be similar pre irradiation here.

7.6 Summary

The study of trap pumping similar devices with difference particle types has revealed a subtle but substantial difference in the measured emission time constants, energy levels and cross sections. The mode values of the divacancy are consistent between emission time constant histograms for each particle type while the distribution of the peak and the skew varies significantly. A "fast tail" feature in the emission time constant histogram is found for proton irradiations that is not replicated in any gamma irradiated device, showing that the emission time constants and energy levels are spread out

rather than found as a single delta function in all cases and this spread is found to increase with dose in the gamma irradiated devices despite only having enough energy to create *point* defects in the silicon. The gamma irradiated devices at all measured radiation doses have a small divacancy peak spread as predicted for "clean" *point* defects while the extended fast tail feature found for the divacancy in the proton irradiated emission time constant histograms is not found for any of the gamma irradiated devices making the feature unique to proton irradiations, and therefore likely linked to lattice structural damage. Further evidence of a difference between point defect sources and defect subcascade/clustering sources is found in the neutron irradiated device that even with a low defect trap count observes a clear broadening in the divacancy emission time constants relative to the unirradiated, 1 MeV electron and ^{60}Co gamma irradiated trap landscapes.

In summary:

1. When combining the mode emission time constants for each divacancy the energy level is found at 0.239 ± 0.0005 eV with a cross section of 1.29 x 10^{-15} cm^{-2} which is in agreement with Laplace DLTS measurements for the energy level, with the assumption the mode of the value is a reliable indicator of the divacancy that has not been distorted through effects such as lattice strain or barrier lowering. Regardless, if the mode value does represent a skewed energy level it is the most numerous across each device and would be a useful starting point for a single value correction model.
2. Overlapping of the resonance curves demonstrate the differences between point defects and clusters of defects where the neutron irradiated device has a large number of multiple defects with similar energy levels and therefore a smaller dipole trap fitting ratio.
3. RPS traps have been discovered that have a behaviour similar to that observed in RTS pixels however they are more prevalent in gamma irradiated devices rather than devices with a larger displacement damage dose such as the high energy protons.

Furthermore, we show here for the first time that the spread is not only real but is found even in *point* defect only irradiations (gamma). The spread increases for proton irradiated devices and again further still for neutron irradiated devices, across many different device batches, irradiations, and facilities, thus suggesting that the additional spread and 'fast tail' are related to the greater lattice structure damage. For applications in space telescopes such as the Euclid VIS instrument, these results demonstrate the great importance of the inclusion of the spread and 'fast tail' in modelling for radiation damage correction.

7.7 References

1. Hall D, Murray N, Holland A, Gow J, Clarke A, Burt D. Determination of In Situ Trap Properties in CCDs Using a "Single-Trap Pumping" Technique. IEEE Transactions on Nuclear Science. 2014;61(4):1826-1833.
2. Bush N. The impact of radiation damage on electron multiplying CCD technology for the WFIRST coronagraph. Open University (United Kingdom); 2018.
3. Kimerling LC. Defect states in electron-bombarded silicon: capacitance transient analyses. InRadiation effects in semiconductors, 1976. Invited and contributed papers from the international conference on radiation effects in semiconductors held in Dubrovnik, 6-9 September 1976 1976.
4. Evwaraye A, Sun E. Electron-irradiation-induced divacancy in lightly doped silicon. Journal of Applied Physics. 1976;47(9):3776-3780.
5. Peaker A, Markevich V, Hawkins I, Hamilton B, Bonde Nielsen K, Gościński K. Laplace deep level transient spectroscopy: Embodiment and evolution. Physica B: Condensed Matter. 2012;407(15):3026-3030.
6. Evans-Freeman J, Peaker A, Hawkins I, Kan P, Terry J, Rubaldo L et al. High-resolution DLTS studies of vacancy-related defects in irradiated and in ion-implanted n-type silicon. Materials Science in Semiconductor Processing. 2000;3(4):237-241.

7. Zangenberg N, Goubet J, Nylandsted Larsen A. On-line DLTS investigations of the mono- and di-vacancy in p-type silicon after low temperature electron irradiation. Nuclear Instruments and Methods in Physics Research Section B: Beam Interactions with Materials and Atoms. 2002;186(1-4):71-77.
8. Fretwurst E, Dehn C, Feick H, Heydarpoor P, Lindström G, Moll M et al. Neutron induced defects in silicon detectors characterized by DLTS and TSC methods. Nuclear Instruments and Methods in Physics Research Section A: Accelerators, Spectrometers, Detectors and Associated Equipment. 1996;377(2-3):258-264.
9. Mooney P, Cheng L, Süli M, Gerson J, Corbett J. Defect energy levels in boron-doped silicon irradiated with 1-MeV electrons. Physical Review B. 1977;15(8):3836-3843.
10. Hopkinson G, Goiffon V, Mohammadzadeh A. Random Telegraph Signals in Proton Irradiated CCDs and APS. IEEE Transactions on Nuclear Science. 2008;55(4):2197-2204.
11. Nuns T, Quadri G, David J, Gilard O, Boudou N. Measurements of Random Telegraph Signal in CCDs Irradiated With Protons and Neutrons. IEEE Transactions on Nuclear Science. 2006;53(4):1764-1771.
12. Evans-Freeman J, Peaker A, Hawkins I, Kan P, Terry J, Rubaldo L et al. High-resolution DLTS studies of vacancy-related defects in irradiated and in ion-implanted n-type silicon. Materials Science in Semiconductor Processing. 2000;3(4):237-241.

Chapter 8: Conclusions and future work

This thesis presents results from a number of CCDs irradiated with multiple particle types at different energies which are then compared using the trap pumping technique to probe individual traps that are known to degrade the performance of the detector. Studying the trap emission time constant histograms for proton, gamma, neutron and electron irradiated devices, features are observed which are unique to the particle type that has ramifications on the correction algorithms developed to mitigate CTI smearing. Both the emission time constant and the energy level measurements for different traps have shown a spread distribution for all particle types rather than a single delta function, providing a compelling argument that the CTI correction methods used for future space missions require a distribution of values for each trap species to accurately correct the data. The emission time constants of individual traps that negatively affect the detector can be measured in-flight by using the trap pumping technique which is proven to be highly accurate, repeatable and would allow for real time measurements of the ever evolving trap landscape for detectors in radiation environments.

Significant differences between incident particle are found in the “fast tail” feature present in the divacancy peak of the proton irradiated devices which are absent in all gamma irradiated devices (repeated for ease of reference in Figure 8.1). The spreading is more pronounced in particle types producing subcascades/clusters (proton and neutron irradiations) as opposed to the *point* defects from ^{60}Co gamma and 1 MeV electron irradiations demonstrating different particles at different energies cause distinct strain effects on the lattice at a high enough dose.

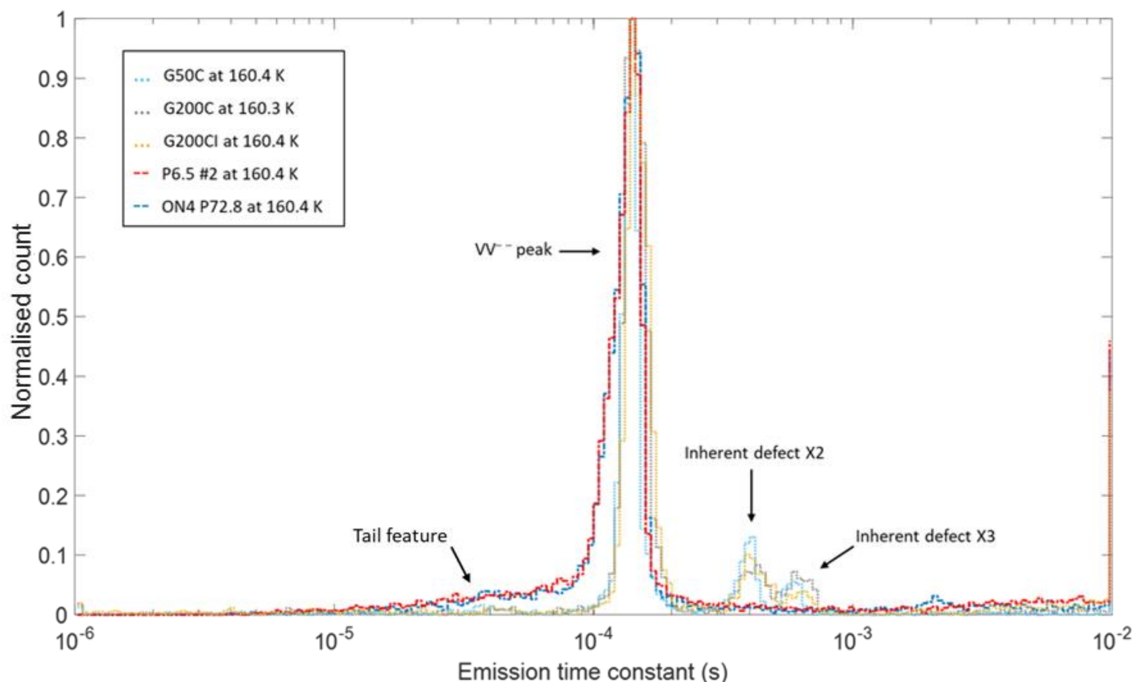

Figure 8.1: Normalised emission time constant histogram for proton and gamma irradiated CCDs at 160.4 K

Despite the significant difference in the trap count between 6.5 MeV and 72.8 MeV proton irradiations, when normalising using feature scaling the distributions of traps are remarkably similar. This reveals that despite irradiating at separate facilities with different irradiation energies and doses the spreading is manifests in proton irradiations independent of these differences, within the particle energy ranges studied.

For proton irradiations the spread is broad and the mechanism for causing displacement damage is understood to generate sub-cascades of vacancies for 6.5 MeV proton irradiations and clusters of vacancies for 72.8 MeV proton irradiations in addition to the Compton scattering events which introduce point defects. The neutron irradiated device, similarly, is predicted to have clustering events dominate the displacement damage interactions which strongly indicates the spreading feature is related to the generation of clusters in the proton devices, as the spreading is not observed in the ^{60}Co or 1 MeV electron beamline irradiated devices, which energetically are only capable of generating point defects.

While the spreading of the emission time constant histograms major peaks is broad, the measured modal location of the double acceptor silicon divacancy is consistent between all devices regardless of particle type, particle energy or dose. This highlights the consistency of the technique and with these measurements the energy level of the most probable divacancy configuration can be calculated (shown in Figure 8.2) at 0.239 ± 0.0005 eV with an effective cross section at 1.29 x 10^{-15} cm^{-2}. This measurement agrees with the Laplace-DLTS measurements for the macroscopic properties of the silicon divacancy found by both (7,12).

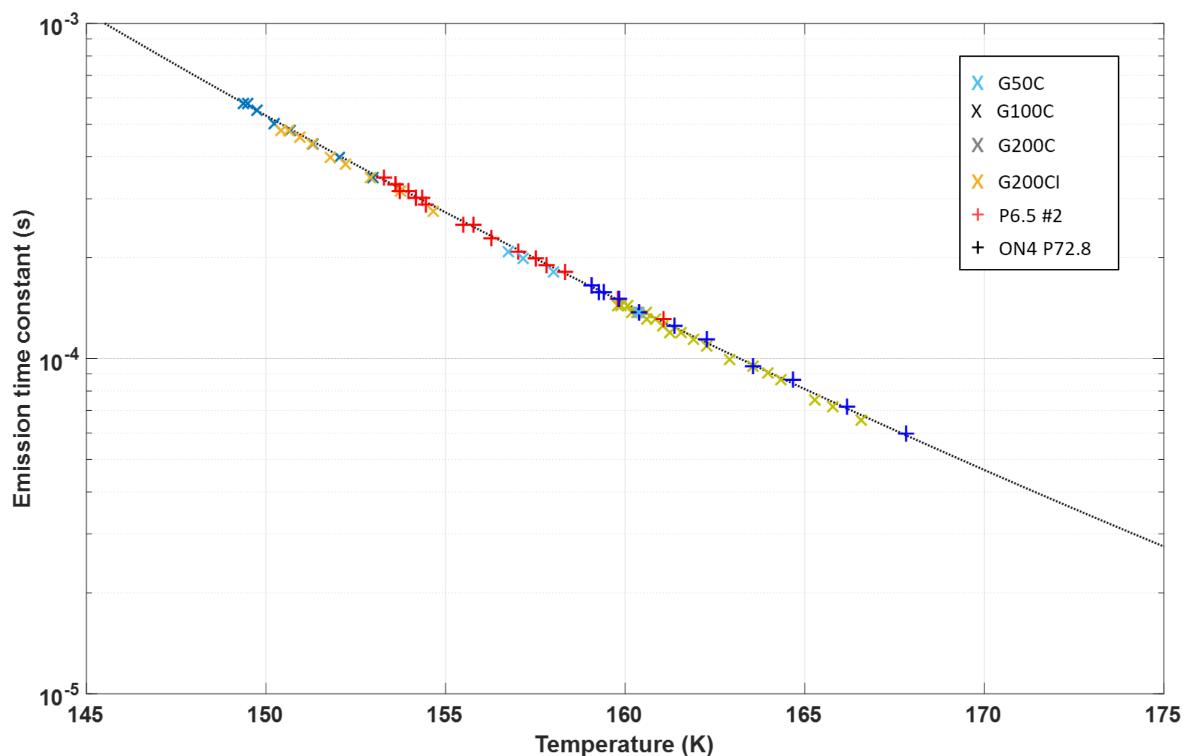

Figure 8.2: Emission time constant histogram mode location for the silicon divacancy peak for every trap pumped device at each temperature trap pumped.

The study has found two new phenomena using the single trap pumping studies. Firstly Random Pumping Signal (RPS) defects which are observed in as many as 15% of the detected traps found at 248 K but as the temperature decreases to 160 K are only measured in the range of a few percent of the total trap population. These traps are of interest because they resemble RTS pixels that display,

over time, step changes in the magnitude of dark current and may provide greater insight into multilevel defects worthy of additional study. Secondly, traps which behave as potential pockets are found following irradiation in gamma irradiated devices between approximately 148 K and 163 K. The ability to characterise these defects in-flight will allow flat band voltage shifts to be mitigated, improving CTI and uncovering any traps hidden by the potential pocket pumping signal. It is also found that these traps are stable over time (at least for the measured range) but are affected by changes in temperature, decreasing in pumping intensity as the temperature is increased.

These results show that the trap pumping technique is necessary to characterise traps found in individual pixels that directly correlate to CTI. Being able to measure the variation in the trap landscape emission time constants as the detector becomes increasingly damaged through the CCD's operational lifetime is therefore critical to the success of future state of the art space instruments which require higher accuracy and therefore better radiation damage mitigation than has been possible before.

Future work following this study will attempt to characterise additional trap species with the same device type, to be made possible at higher temperatures by a chamber redesign. The goal will be to compare the introduction rates of different trap species; there is the possibility of additional defect complexes in proton irradiations from substitutional hydrogen creating complexes. The observation of the potential pockets and their disappearance with increasing temperature warrants additional study; is it specific to the ≈150 K temperature range or do these traps reappear at other temperatures and are they found in the same pixels as previously observed?

The continuum of traps found by Bush (2) have been briefly discussed in this study and it would therefore be useful to find if the observation is consistent with spreading of other major peaks, similar to the proton irradiation "fast tail", or if the continuum is made of different isolated traps in low volume throughout the detector. Trap pumping measurements at higher temperatures would also allow for the study of the RPS defects from different trap species as they have been observed in both the double acceptor silicon divacancy and the "unknown" defect.

The trap pumping technique has proven to be a powerful tool for the characterisation of traps that directly affect the CCDs performance and has been used extensively in this thesis to find new and exciting physics. It is the hope of the author that the results in this thesis can be used in further research and development of CCDs and assist space-based telescopes in answering the pressing scientific questions of our time.

Appendix

A1: Additional Trends

While only a single pumping scheme is possible for the AIMO CCD47-20s, the NIMO CCD347-20s are capable of fully backclocking and multiple pumping schemes are available that allow for probing for traps at different regions under the electrodes. Multiple pumping schemes were tested to increase the trap statistics as different sub-pixel regions are probed and to confirm the findings of (Bush 2018) that the “split peak” phenomenon is a fitting error brought about from the difficulty to distinguish between multiple fitting curves. Using the pumping configuration (1231’321) shown in Figure A.1 additional regions are measurable.

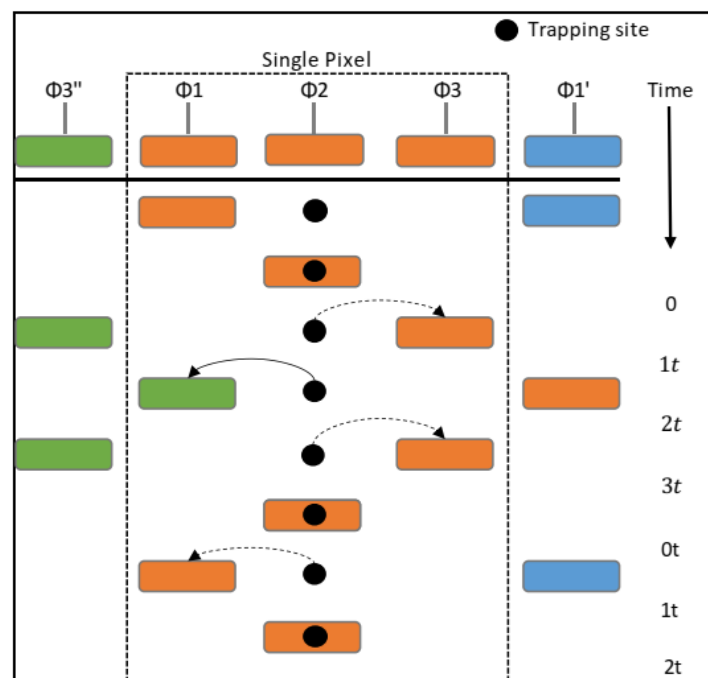

Figure A.1: The trap pumping scheme (1231’321) that cyclically shuffles the charge cloud for a CCD347-20. The black dots represent the traps that capture the signal from the charge cloud. The dotted arrows show the electron captured by a trap reemitting at the time necessary to return to the original charge packet. The solid arrow shows a successfully pump for traps located under ϕ2 to the charge cloud of the neighbouring pixel.

In Figure A.2 the G100 device is trap pumped using two different trap pumping schemes (at different temperatures to show a side by side comparison) where the (231’32) scheme shows a single major peak for the divacancy whereas the alternate scheme (1231’321) finds the same daughter peak and

shoulder peaks found in (Bush 2018 and Wood 2018). The second pumping scheme has more stages necessary to complete a single pump and therefore more phase time periods possible for reemission compared to a three stage pumping scheme. The difficulty of distinguishing between the characteristic resonance curves described by the different fitting equations 6.1 and 6.2 can result in these distortions of the emission time constants.

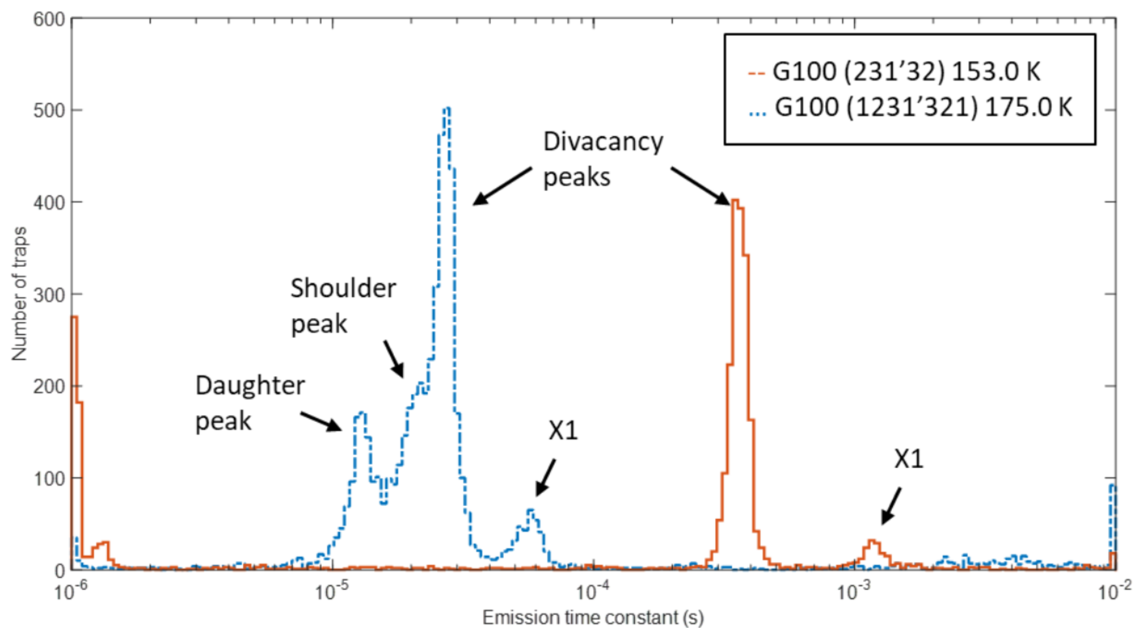

Figure A.2: Histogram of the emission time constants of two trap pumping schemes for the G100 device at 153.0 K and 175.0 K to demonstrate the different features.

As found in (Bush 2018) the difference in peak locations based off the possible distortions of the emission time constants is equal to ln(2)/ln(3/2) ≈ 1.7 which is the experimentally verified factor difference between the daughter peak and the divacancy peak for the (1231'321) scheme. The shoulder peak is not found in the (231'32) scheme indicating it is also a distortion of the fitting equations as the major peak is found to be symmetrical with an equal spreading of emission time constants towards the valance and conduction bands. These results give confidence that the additional 'fast tail' features found in the proton irradiated devices of the previous chapter are not distorted fitting features and a real distribution (e.g. from another trap species or lattice strain effects or field enhanced emission) as the gamma irradiated devices fail to measure the feature at across the multiple radiation doses studied.

Reprints and permissions forms

ELSEVIER LICENSE
TERMS AND CONDITIONS

Sep 24, 2020

This Agreement between Open university -- Anton Lindley-DeCaire ("You") and Elsevier ("Elsevier") consists of your license details and the terms and conditions provided by Elsevier and Copyright Clearance Center.

License Number	4915270827261
License date	Sep 24, 2020
Licensed Content Publisher	Elsevier
Licensed Content Publication	Planetary and Space Science
Licensed Content Title	Prediction of solar minimum and maximum epochs on the basis of spectral characteristics for the next millennium
Licensed Content Author	N.R. Rigozo,D.J.R. Nordemann,E. Echer,M.P.S. Echer,H.E. Silva
Licensed Content Date	Dec 1, 2010
Licensed Content Volume	58
Licensed Content Issue	14-15
Licensed Content Pages	6
Start Page	1971
End Page	1976
Type of Use	reuse in a thesis/dissertation
Portion	figures/tables/illustrations
Number of figures/tables/illustrations	1
Format	both print and electronic
Are you the author of this Elsevier article?	No
Will you be translating?	No
Title	The impact of irradiation particle type and energy on radiation-induced trap properties in CCDs
Institution name	The Open University
Expected presentation date	Nov 2020
Order reference number	None
Portions	Figure 1
Requestor Location	Open university Milton Keynes, Buckinghamshire MK7 6AA United Kingdom Attn: Open university
Publisher Tax ID	GB 494 6272 12

ELSEVIER LICENSE
TERMS AND CONDITIONS
Sep 24, 2020

This Agreement between Open university -- Anton Lindley-DeCaire ("You") and Elsevier ("Elsevier") consists of your license details and the terms and conditions provided by Elsevier and Copyright Clearance Center.

License Number	4915350909204
License date	Sep 24, 2020
Licensed Content Publisher	Elsevier
Licensed Content Publication	Elsevier Books
Licensed Content Title	Advances in Imaging and Electron Physics
Licensed Content Author	T.D. Hardy,M.J. Deen,R. Murowinski
Licensed Content Date	Jan 1, 1999
Licensed Content Pages	96
Start Page	1
End Page	96
Type of Use	reuse in a thesis/dissertation
Portion	figures/tables/illustrations
Number of figures/tables/illustrations	1
Format	both print and electronic
Are you the author of this Elsevier chapter?	No
Will you be translating?	No
Title	The impact of irradiation particle type and energy on radiation-induced trap properties in CCDs
Institution name	The Open University
Expected presentation date	Nov 2020
Order reference number	None
Portions	Figure 7
Requestor Location	Open university Milton Keynes, Buckinghamshire MK7 6AA United Kingdom Attn: Open university
Publisher Tax ID	GB 494 6272 12

ELSEVIER LICENSE
TERMS AND CONDITIONS
Sep 24, 2020

This Agreement between Open university -- Anton Lindley-DeCaire ("You") and Elsevier ("Elsevier") consists of your license details and the terms and conditions provided by Elsevier and Copyright Clearance Center.

License Number	4915391304797
License date	Sep 24, 2020
Licensed Content Publisher	Elsevier
Licensed Content Publication	Elsevier Books
Licensed Content Title	Handbook of Thin Film Deposition Processes and Techniques
Licensed Content Author	Martin L. Hammond
Licensed Content Date	Jan 1, 2001
Licensed Content Pages	66
Start Page	45
End Page	110
Type of Use	reuse in a thesis/dissertation
Portion	figures/tables/illustrations
Number of figures/tables/illustrations	1
Format	both print and electronic
Are you the author of this Elsevier chapter?	No
Will you be translating?	No
Title	The impact of irradiation particle type and energy on radiation-induced trap properties in CCDs
Institution name	The Open University
Expected presentation date	Nov 2020
Order reference number	None
Portions	Figure 1
Requestor Location	Open university Milton Keynes, Buckinghamshire MK7 6AA United Kingdom Attn: Open university
Publisher Tax ID	GB 494 6272 12

SPRINGER NATURE LICENSE
TERMS AND CONDITIONS
Sep 24, 2020

This Agreement between Open university -- Anton Lindley-DeCaire ("You") and Springer Nature ("Springer Nature") consists of your license details and the terms and conditions provided by Springer Nature and Copyright Clearance Center.

License Number	4915400701047
License date	Sep 24, 2020
Licensed Content Publisher	Springer Nature
Licensed Content Publication	Springer eBook
Licensed Content Title	Single-Crystal Silicon: Electrical and Optical Properties
Licensed Content Author	Mark Auslender, Shlomo Hava
Licensed Content Date	Jan 1, 2017
Type of Use	Thesis/Dissertation
Requestor type	academic/university or research institute
Format	print and electronic
Portion	figures/tables/illustrations
Number of figures/tables/illustrations	1
Will you be translating?	no
Circulation/distribution	1 - 29
Author of this Springer Nature content	no
Title	The impact of irradiation particle type and energy on radiation-induced trap properties in CCDs
Institution name	The Open University
Expected presentation date	Nov 2020
Order reference number	None
Portions	Figure 21.1
	Open university
Requestor Location	Milton Keynes, Buckinghamshire MK7 6AA United Kingdom Attn: Open university

SPRINGER NATURE LICENSE
TERMS AND CONDITIONS
Sep 24, 2020

This Agreement between Open university -- Anton Lindley-DeCaire ("You") and Springer Nature ("Springer Nature") consists of your license details and the terms and conditions provided by Springer Nature and Copyright Clearance Center.

License Number	4915400994857
License date	Sep 24, 2020
Licensed Content Publisher	Springer Nature
Licensed Content Publication	Earth, Planets and Space
Licensed Content Title	Complexities of gamma-ray line intensities from the lunar surface
Licensed Content Author	Naoyuki Yamashita et al
Licensed Content Date	Apr 9, 2008
Type of Use	Thesis/Dissertation
Requestor type	academic/university or research institute
Format	print and electronic
Portion	figures/tables/illustrations
Number of figures/tables/illustrations	1
Will you be translating?	no
Circulation/distribution	1 - 29
Author of this Springer Nature content	no
Title	The impact of irradiation particle type and energy on radiation-induced trap properties in CCDs
Institution name	The Open University
Expected presentation date	Nov 2020
Order reference number	None
Portions	Figure 1
Requestor Location	Open university Milton Keynes, Buckinghamshire MK7 6AA United Kingdom Attn: Open university